

REPORT DOCUMENTATION PAGE				Form Approved OMB NO. 0704-0188	
<p>The public reporting burden for this collection of information is estimated to average 1 hour per response, including the time for reviewing instructions, searching existing data sources, gathering and maintaining the data needed, and completing and reviewing the collection of information. Send comments regarding this burden estimate or any other aspect of this collection of information, including suggestions for reducing this burden, to Washington Headquarters Services, Directorate for Information Operations and Reports, 1215 Jefferson Davis Highway, Suite 1204, Arlington VA, 22202-4302. Respondents should be aware that notwithstanding any other provision of law, no person shall be subject to any penalty for failing to comply with a collection of information if it does not display a currently valid OMB control number.</p> <p>PLEASE DO NOT RETURN YOUR FORM TO THE ABOVE ADDRESS.</p>					
1. REPORT DATE (DD-MM-YYYY) 01-11-2012		2. REPORT TYPE Final Report		3. DATES COVERED (From - To) 15-Nov-2010 - 14-Aug-2012	
4. TITLE AND SUBTITLE New Solutions for Energy Absorbing Materials				5a. CONTRACT NUMBER W911NF-11-1-0032	
				5b. GRANT NUMBER	
				5c. PROGRAM ELEMENT NUMBER 611102	
6. AUTHORS Michael R. Haberman, Carolyn C. Seepersad, Preston S. Wilson, Kim Alderson, Andrew Alderson, Fabrizio Scarpa				5d. PROJECT NUMBER	
				5e. TASK NUMBER	
				5f. WORK UNIT NUMBER	
7. PERFORMING ORGANIZATION NAMES AND ADDRESSES The University of Texas at Austin The Univ. of Texas at Austin, DBA Applied Res. Lab 10000 Burnet Road Austin, TX 78758 -4423				8. PERFORMING ORGANIZATION REPORT NUMBER	
9. SPONSORING/MONITORING AGENCY NAME(S) AND ADDRESS(ES) U.S. Army Research Office P.O. Box 12211 Research Triangle Park, NC 27709-2211				10. SPONSOR/MONITOR'S ACRONYM(S) ARO	
				11. SPONSOR/MONITOR'S REPORT NUMBER(S) 58520-EG.4	
12. DISTRIBUTION AVAILABILITY STATEMENT Approved for Public Release; Distribution Unlimited					
13. SUPPLEMENTARY NOTES The views, opinions and/or findings contained in this report are those of the author(s) and should not be construed as an official Department of the Army position, policy or decision, unless so designated by other documentation.					
14. ABSTRACT The objective of this project was to understand, design, and evaluate composite materials containing engineered microstructures that display negative stiffness (NS) and negative Poisson's ratio (auxetic) behavior. The ultimate aim for understanding such microstructural elements is to enable the creation of composite materials that are significantly more dissipative than currently available materials to enhance existing mechanical absorption and isolation capabilities without degrading stiffness performance. Progress has been made in the design and analysis of					
15. SUBJECT TERMS energy absorption, composite materials, metamaterials, auxetic materials, negative stiffness					
16. SECURITY CLASSIFICATION OF:			17. LIMITATION OF ABSTRACT UU	15. NUMBER OF PAGES	19a. NAME OF RESPONSIBLE PERSON Michael Haberman
a. REPORT UU	b. ABSTRACT UU	c. THIS PAGE UU			19b. TELEPHONE NUMBER 512-835-3149

## Report Title

New Solutions for Energy Absorbing Materials

### ABSTRACT

The objective of this project was to understand, design, and evaluate composite materials containing engineered microstructures that display negative stiffness (NS) and negative Poisson's ratio (auxetic) behavior. The ultimate aim for understanding such microstructural elements is to enable the creation of composite materials that are significantly more dissipative than currently available materials to enhance existing mechanical absorption and isolation capabilities without degrading stiffness performance. Progress has been made in the design and analysis of NS microstructures that exploit buckled element geometry to produce NS behavior. The nonlinear effective material properties of the microstructure have been obtained using finite element analysis and the overall behavior of a composite material containing NS inclusions has been determined using combined FEA and analytical effective medium theory. Auxetic materials work has produced particulate composite materials containing auxetic  $\gamma$ -crystalite inclusions. The resulting composite materials have been characterized using quasistatic, modal vibration, and ultrasonic methods together with extensive microscopy. The knowledge gained during the work of this project can be used in future research to provide a basis for the design of microstructures that can aid in absorbing vibroacoustic energy to improve overall composite material performance through variations of engineered microstructure.

---

**Enter List of papers submitted or published that acknowledge ARO support from the start of the project to the date of this printing. List the papers, including journal references, in the following categories:**

**(a) Papers published in peer-reviewed journals (N/A for none)**

Received

Paper

**TOTAL:**

**Number of Papers published in peer-reviewed journals:**

---

**(b) Papers published in non-peer-reviewed journals (N/A for none)**

Received

Paper

**TOTAL:**

**Number of Papers published in non peer-reviewed journals:**

---

**(c) Presentations**

1. M.R. Haberman, D.T. Hook, T.D. Klatt, A. Alderson, K.L. Alderson, T.A.M. Hewage, F.L. Scarpa, "Ultrasonic Characterization of Polymeric Composites Containing Auxetic Inclusions," Presented at The 164th Meeting of the Acoustical Society of America, Kansas City, MO, (22-26 October 2012).
2. T. Klatt, M.R. Haberman, D.W. Shahan, C.C. Seepersad, "Hierarchical Modeling and Design of Composite Materials with Negative Stiffness Inclusions," Presented at the 49th Annual Technical Meeting of the Society of Engineering Science, Atlanta, GA, (10-12 October 2012).
3. T.A.M. Hewage, K. Alderson and A. Alderson, "Microscopy of Auxetic particulate filled polymers," Auxetics 2011, 8th International Workshop on Auxetics and Related Systems, Szczecin, Poland, (2011).
4. T. A. M. Hewage , A. Alderson, K.L. Alderson, M.R. Haberman, T Klatt, F.L. Scarpa, "Design and Development of a Multifunctional System Displaying Negative Poisson's ratio and Negative Stiffness Behaviour," Materials KTN Annual Meeting: Materials Energising Manufacturing in the UK. London: Institute of Materials, Minerals and Mining, (2012).
5. T.A.M. Hewage, A. Alderson, K.L. Alderson, M.R. Haberman, T. Klatt, F.L. Scarpa, "A system incorporating two negative properties: negative Poisson's ratio and negative stiffness". Research and Innovation conference, University of Bolton. Bolton, UK, (2012).
6. A. Alderson, K.L. Alderson, D. Di Maio, M.R. Haberman, T. A. M. Hewage, T. Klatt and F.L. Scarpa, "New Solutions for Improved Energy Absorbing materials: Auxetic composites," Presented at Dynacomp, 1st International Conference on Composites Dynamics, Arcachon, France, (22 – 24 May 2012).
7. M.R. Haberman, T.D. Klatt, P.S. Wilson, C.C. Seepersad, "Negative Stiffness Metamaterials and Periodic Composites," Presented at Acoustics 2012, Joint 163rd Meeting of the Acoustical Society of America, the 8th meeting of the Acoustical Society of China, the 11th Western Pacific Acoustics Conference, and the Hong Kong Institute of Acoustics, Hong Kong, China, (13 – 18 May 2012).
8. T. Klatt, D. Shahan, M.R. Haberman, C.C. Seepersad, P.S. Wilson, "Investigation on the use of thermal expansion mismatch to produce engineered negative stiffness metamaterial inclusions," Presented at the Joint Conference on Advanced Materials, Szczecin, Poland, (6-9 September, 2011).
9. D. Shahan, B. Fulcher, C.C. Seepersad, M.R. Haberman, P.S. Wilson, "Robust Design of Constrained Bistable Structures for Selective Laser Sintering," Presented at the Twenty Second Annual International Solid Freeform Fabrication Symposium – An Additive Manufacturing Conference, Austin, TX, (8-10 September 2011).

**Number of Presentations:** 9.00

---

**Non Peer-Reviewed Conference Proceeding publications (other than abstracts):**

<u>Received</u>	<u>Paper</u>
08/31/2011	2.00 Klatt, T., Shahan, D., Haberman, M.R., Seepersad, C.C., Wilson, P.S.. Investigation on the use of thermal expansion mismatch to produce engineered negative stiffness metamaterial inclusions, 8th Workshop on Auxetics and Related Systems. 2011/09/06 01:00:00, . : ,
08/31/2011	3.00 Alderson, A., Alderson, K., Hewage, T.A.M.. Microscopy of auxetic particulate filled polymers, 8th Workshop on Auxetics and Related Systems. 2011/09/06 01:00:00, . : ,
<b>TOTAL:</b>	<b>2</b>

**Number of Non Peer-Reviewed Conference Proceeding publications (other than abstracts):**

---

**Peer-Reviewed Conference Proceeding publications (other than abstracts):**

Received

Paper

TOTAL:

Number of Peer-Reviewed Conference Proceeding publications (other than abstracts):

---

(d) Manuscripts

Received

Paper

TOTAL:

Number of Manuscripts:

---

Books

Received

Paper

TOTAL:

Patents Submitted

---

Patents Awarded

---

Awards

---

Graduate Students

<u>NAME</u>	<u>PERCENT SUPPORTED</u>	Discipline
Timothy Klatt	1.00	
Mawanane Hewage Trishan Akila	1.00	
<b>FTE Equivalent:</b>	<b>2.00</b>	
<b>Total Number:</b>	<b>2</b>	

#### Names of Post Doctorates

<u>NAME</u>	<u>PERCENT SUPPORTED</u>
<b>FTE Equivalent:</b>	
<b>Total Number:</b>	

#### Names of Faculty Supported

<u>NAME</u>	<u>PERCENT SUPPORTED</u>	National Academy Member
Michael R. Haberman	0.20	
Carolyn C. Seepersad	0.05	
Preston S. Wilson	0.05	
Andrew Alderson	0.05	
Kim Alderson	0.10	
Fabrizio Scarpa	0.05	
<b>FTE Equivalent:</b>	<b>0.50</b>	
<b>Total Number:</b>	<b>6</b>	

#### Names of Under Graduate students supported

<u>NAME</u>	<u>PERCENT SUPPORTED</u>	Discipline
Ryan Connell	0.10	Physics
<b>FTE Equivalent:</b>	<b>0.10</b>	
<b>Total Number:</b>	<b>1</b>	

#### Student Metrics

This section only applies to graduating undergraduates supported by this agreement in this reporting period

The number of undergraduates funded by this agreement who graduated during this period: ..... 1.00

The number of undergraduates funded by this agreement who graduated during this period with a degree in science, mathematics, engineering, or technology fields:..... 1.00

The number of undergraduates funded by your agreement who graduated during this period and will continue to pursue a graduate or Ph.D. degree in science, mathematics, engineering, or technology fields:..... 1.00

Number of graduating undergraduates who achieved a 3.5 GPA to 4.0 (4.0 max scale):..... 1.00

Number of graduating undergraduates funded by a DoD funded Center of Excellence grant for Education, Research and Engineering:..... 0.00

The number of undergraduates funded by your agreement who graduated during this period and intend to work for the Department of Defense ..... 0.00

The number of undergraduates funded by your agreement who graduated during this period and will receive scholarships or fellowships for further studies in science, mathematics, engineering or technology fields: ..... 0.00

#### Names of Personnel receiving masters degrees

<u>NAME</u>
Timothy Klatt
<b>Total Number:</b>

1

---

**Names of personnel receiving PhDs**

NAME

**Total Number:**

---

**Names of other research staff**

NAME

PERCENT SUPPORTED

**FTE Equivalent:**

**Total Number:**

---

**Sub Contractors (DD882)**

1 a. THE UNIVERSITY OF BOLTON

1 b. DEANE RD

BOLTON

BL3 5AB

**Sub Contractor Numbers (c):**

**Patent Clause Number (d-1):**

**Patent Date (d-2):**

**Work Description (e):** Fabrication, analysis, and characterization of auxetic inclusion composite materials

**Sub Contract Award Date (f-1):** 11/15/2010 12:00:00AM

**Sub Contract Est Completion Date(f-2):** 4/1/2012 12:00:00AM

---

1 a. THE UNIVERSITY OF BOLTON

1 b. DEANE RD

BOLTON

BL3 5AB

**Sub Contractor Numbers (c):**

**Patent Clause Number (d-1):**

**Patent Date (d-2):**

**Work Description (e):** Fabrication, analysis, and characterization of auxetic inclusion composite materials

**Sub Contract Award Date (f-1):** 11/15/2010 12:00:00AM

**Sub Contract Est Completion Date(f-2):** 4/1/2012 12:00:00AM

---

**Inventions (DD882)**

**Scientific Progress**

See attachment

**Technology Transfer**

# **New Solutions for Improved Energy Absorbing Materials**

Project Duration: 15 November 2010 – 31 July 2012

Reporting Period: 15 November 2010 – 31 July 2012

## **1 Abstract**

The objective of this project was to understand, design, and evaluate composite materials containing engineered microstructures that display negative stiffness (NS) and negative Poisson's ratio (auxetic) behavior. The ultimate aim for understanding such microstructural elements is to enable the creation of composite materials that are significantly more dissipative than currently available materials (see Figure 1) to enhance existing mechanical absorption and isolation capabilities without degrading stiffness performance. Progress has been made in the design and analysis of NS microstructures that exploit buckled element geometry to produce NS behavior. The nonlinear effective material properties of the microstructure have been obtained using finite element analysis and the overall behavior of a composite material containing NS inclusions has been determined using combined FEA and analytical effective medium theory. Auxetic materials work has produced particulate composite materials containing auxetic  $\alpha$ -cristobalite inclusions. The resulting composite materials have been characterized using quasistatic, modal vibration, and ultrasonic methods together with extensive microscopy. The knowledge gained during the work of this project can be used in future research to provide a basis for the design of microstructures that can aid in absorbing vibroacoustic energy to improve overall composite material performance through variations of engineered microstructure.

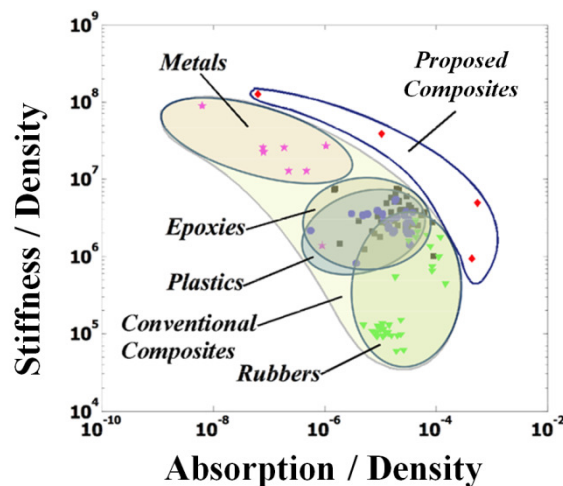


Figure 1: Plot (log-log scale) of stiffness and mechanical absorption normalized to mass density of existing materials and composites containing negative stiffness and auxetic inclusions. The proposed materials lie in the white space of currently un-attainable properties. Estimates were found using Mori-Tanaka model with 2%vol of negative inclusion.



## 2 Table of Contents

1	Abstract.....	1
2	Table of Contents.....	2
3	International Collaboration.....	3
4	Scientific Progress and Accomplishments.....	3
4.1	Negative Stiffness Materials .....	3
4.1.1	Negative stiffness.....	5
4.1.2	Mesoscale inclusion characterization .....	8
4.1.3	Benchmarking the energy derivative approach.....	12
4.1.4	Microstructure modeling .....	14
4.1.5	Mesoscale inclusion modeling and design.....	17
4.1.6	FEA of candidate negative stiffness mesoscale inclusion .....	18
4.1.7	Mesoscale → mesoscale effective medium modeling .....	26
4.1.8	Validation of the Mesoscale Effective Stiffness Approximation .....	29
4.1.9	Microstructural Design: Geometry Parameterization .....	33
4.1.10	Microstructural Design: Geometry Dependent Stiffness.....	34
4.1.11	Microstructural Design: Kriging Surrogate Modeling .....	37
4.2	Negative Poisson Ratio Materials .....	38
4.2.1	Processing routes to produce auxetic extruded fibers and films .....	40
4.2.2	Information on NPR materials selected and why they are of interest .....	45
4.2.3	Fabrication of $\alpha$ -cristobalite samples .....	45
4.2.4	Microscopy.....	45
4.2.5	Quasistatic Mechanical Testing of $\alpha$ -cristobalite Inclusion Composites.....	49
4.2.6	Energy absorptive capacity of the composites .....	52
4.2.7	Characterization of Particulate Composites Containing $\alpha$ -critobalite .....	53
5	Insights and Future Work.....	63
6	References .....	65

### 3 International Collaboration

Research supported by this project was carried out as an international collaboration between the University of Texas at Austin in the United States and the Universities of Bolton and Bristol in the United Kingdom. This project represents the first effort to establish and foster an international collaboration between these centers of excellence in the areas of negative stiffness and negative Poisson's ratio materials. The principle investigator and US team is located at the University of Texas at Austin and has led recent investigations into the design and testing of negative stiffness mechanisms for vibration isolation [1a,1b]. The members of the US team, Drs. Michael Haberman, Carolyn Seepersad, and Preston Wilson, have expertise in the areas of material modeling, materials design, wave propagation, and dynamic material testing and characterization. The UK team has been assembled with researchers at the Universities of Bolton and Bristol, consisting of Drs. Andrew and Kim Alderson at Bolton and Dr. Fabrizio Scarpa at Bristol. These researchers have extensively studied the static and dynamic behavior and fabrication of auxetic materials. Their combined areas of expertise include modeling, fabrication, and characterization of composite and honeycomb materials for both static and dynamic applications.

### 4 Scientific Progress and Accomplishments

As mentioned in the abstract, the project work consists of research in two coupled areas: composites containing (i) negative stiffness (NS) and (ii) negative Poisson's ratio (auxetic) inclusions. Initial efforts that incorporate NS elements into an auxetic network has also been investigated during this project. Progress on NS portions of the research is presented and discussed in Section 4.1 while auxetic material research is discussed in Section 4.2. Based on the information presented in those sections, insight for associated future research is provided in Section 5.

#### 4.1 Negative Stiffness Materials

The negative stiffness research effort of this project was guided by the materials design approach schematized in Figure 2. The results presented in this final report focus primarily on steps (i) and (ii) in the schematized multiscale material model shown in the blue box of Figure 2. The two steps are microstructural modeling and mesoscale homogenization of candidate microstructures, respectively, which are discussed in Sections 4.1.2 – 4.1.6. Progress made in these areas has provided the research team with a comprehensive understanding and robust modeling capability that captures the behavior of candidate microstructures exhibiting negative stiffness at the mesoscale. Initial progress on the exploration of the multi-dimensional nonlinear design space using surrogate models is reported in Sections 4.1.9–4.1.11. This tools and understanding provided by the coupled multiscale model and surrogate modeling approach can be leveraged in future materials design work to tailor microstructure to produce NS for improved stiffness and loss performance at the macroscale. Limited work has also been done on step (iii) of the multiscale material model and is discussed in Section 4.1.7.

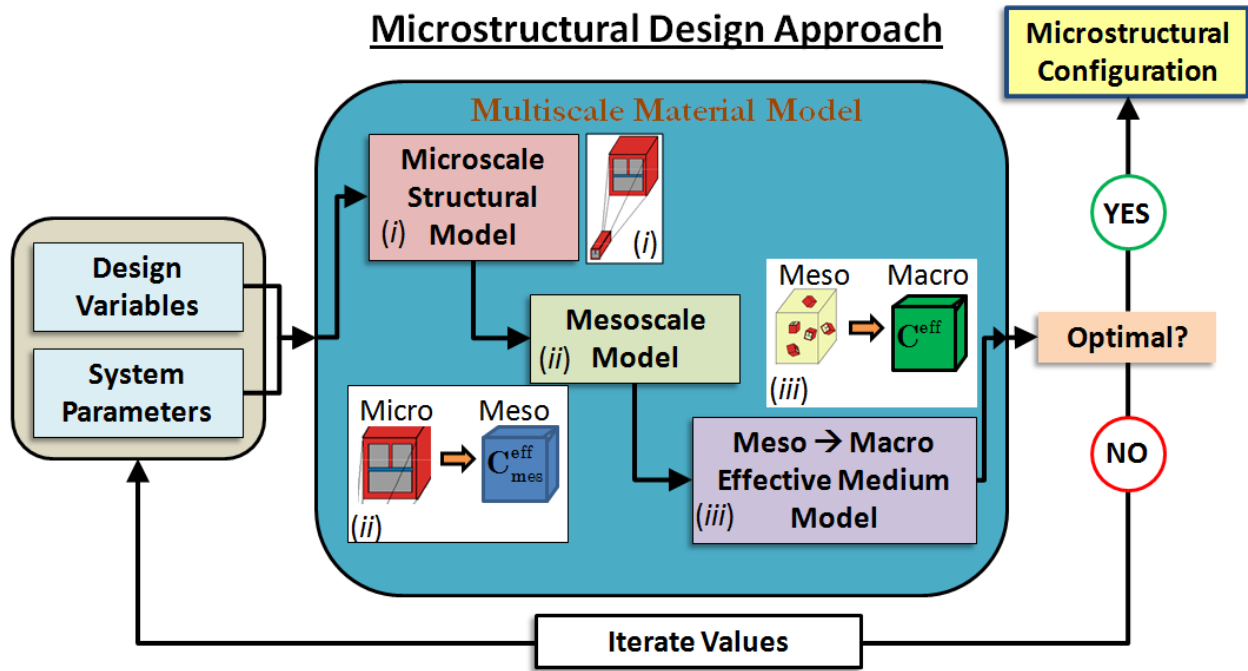


Figure 2: Schematic of the multi-scale materials design approach devised to design negative stiffness inclusions for improved macroscopic material performance.

Before discussing the results, it is important to define what is meant by the terms micro-, meso-, and macroscale in this work and to introduce the multiscale modeling scheme at the core of the materials design effort. In general, the material system is assumed to be well described on three distinct length scales: the micro-, meso-, and macroscales, in ascending order and indicated by boxes (i), (ii), and (iii) in Figure 2, respectively. Further, the materials design approach assumes that the overall behavior of the composite material, whose ultimate purpose is to absorb vibro-acoustic energy, can be predicted using a multiscale model that takes structure and properties at all length scales into account. Because the microscale behavior required to produce NS phenomena is inherently nonlinear, the homogenization scheme must also admit nonlinear microscale behavior and the design methodology must be of sufficient sophistication to enable efficient, yet complete, design space exploration of nonlinear systems. To achieve these goals, two distinct scale transition models were developed and a robust design space exploration scheme was adopted. The first scale transition model is the micro- to mesoscale transition model and the second is the meso- to macroscale transition model, indicated in the white boxes labeled (ii) and (iii) of Figure 2, respectively. Note that the output of the first scale transition model is part of the input to the second. These scale transition models are described in general in the following paragraphs and in detail in Sections 4.1.5–4.1.7. The design space exploration is introduced and discussed in Sections 4.1.9–4.1.11.

The materials modeled in this portion of the project are assumed to consist of a continuous matrix material containing a known volume fraction of structured inclusions. The macroscale is denoted with the length scale,  $L_M$ , which satisfies the condition  $L_m/L_M \ll 1$ . Here  $L_m$  is the descriptive length of the structured inclusions and is the descriptive dimension of the mesoscale. At the macroscale the the

particulate composite material is assumed to behave as an effective homogeneous medium. The properties of the effective medium can be estimated using well-established effective medium theories (EMT) if the elastic properties of the mesoscale structures as well as their volume fraction and spatial orientation distribution are known. This aspect of the multiscale material model, known as the meso- to macroscale transition model, is addressed in Section 4.1.7. In practice one notes that a scale discrepancy of  $L_m/L_M \sim O(1/10)$  is sufficient to enable reliable estimates of the macroscopic material properties using classical EMT methods [1c].

In the present work, as in most multiscale modeling literature [1c], the mesoscale is simply an intermediary scale between the inclusion structure feature size and macroscopic length scale. One key focus of the research reported here is the development of a nonlinear homogenization model to allow for the accurate approximation of the effective nonlinear elastic response of an arbitrarily shaped structured inclusion using finite element analysis (FEA). This homogenization step is known as the micro- to mesoscopic scale transition model. It is this scale transition model, a very unique contribution of the work associated with this project, which that enables the use of classical EMT to predict the macroscopic properties and their dependence on microscale structure and the associated NS. The final length scale of interest, the microscale, is defined as the descriptive lengths of the structure of within the inclusions and is denoted as  $L_\mu$ . It is the microstructure that leads to mesoscopic NS behavior and significant increases in absorptive capacity on the macroscopic scale. A detailed understanding of the impact of microscale structure to produce NS is therefore the principal importance for this project.

#### 4.1.1 Negative stiffness

Negative stiffness systems are rare in nature and therefore not as well understood or utilized as positive stiffness systems. Positive stiffness systems are simply defined by the ability of the system to offer increasing resistance to deformation due to externally applied forces. On the contrary, a negative stiffness system will offer decreasing resistance to an applied load and can even assist the applied force in deforming the system [1], [2]. This behavior leads to significantly larger system deformation than would be observed for the same force applied to a positive stiffness system. Recall that the stiffness of any object,  $k$ , is the force required to deform the object by a certain distance, or  $F = k\Delta x$ . One very simple example of a system displaying negative stiffness properties is a transversely loaded buckled beam. A buckled beam is a simple example of a bistable system. Negative stiffness can be observed for such a bistable system in one of two scenarios, the first of which is depicted by Figure 3. In this case, the beam starts in one of the two stable configurations and driven to the other bistable configuration. In this scenario, the buckled beam initially resists deformation, but once a certain force threshold is reached, the beam “snaps through” to a new configuration and remains in that configuration even after the force is removed. In this case, the negative stiffness behavior occurs during the snap through, is transient, and leads to large, and permanent, deformations. The second scenario where negative stiffness can be observed is the case where a buckled beam is constrained at its center point by another element, such as a spring. In this case, the beam remains in position (2) of Figure 3 but will move when perturbed by an outside force. The constraining element will then force the beam to return to position (2) when the outside force is removed. This scenario represents the case of constrained negative stiffness (CNS),

which is very useful for vibroacoustic damping where loads are low enough in amplitude to not force the beam to oscillate between bistable positions.

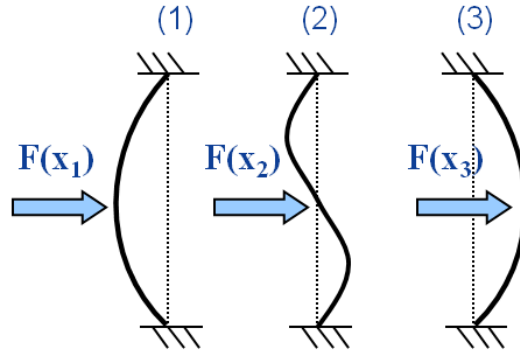


**Figure 3: Schematic of the behavior of a beam of original length  $L_0$  with buckled length  $L_0 - \delta L$ . The beam is loaded in displacement control from one bistable position, (configuration 1), to the other, (configuration 3).**

The behavior of both of these scenarios and how it relates to negative stiffness can be related to the positions and forces shown in Figure 3. Notably, the buckled beam force versus displacement response is in stark contrast to that of an unbuckled beam where an applied transverse force will cause the beam to deflect in proportion to the applied external force only to return to its original position when all forces are removed.

To better understand how this behavior is indicative of negative stiffness and what the roots of this behavior are in terms of mechanical metrics, it is useful to consider force and internal strain energy versus displacement behavior. Both of these metrics are depicted in curves shown in Figure 4 and compared with the behavior of an unbuckled beam for reference. The left panel of this figure shows the normalized force versus displacement of the beam center point. The normalized force is given as  $2F / P_{cr}$  where  $F$  is the transversely applied load and  $P_{cr}$  is the axial load that induces buckling as predicted by Euler-Bernoulli beam theory. The normalized displacement is  $\Delta x / L$  where  $\Delta x$  is the displacement from the  $x = 0$  position and  $L$  is the free beam length. There are several points illustrated in these curves that are worth highlighting. First of all, note that positions (1), (2), and (3) all represent configurations where zero force is required to maintain that shape. In other words, theory predicts that the c-shape of configuration (points 1 and 3) and the s-shape configuration (point 2) are points of ‘stability.’ These stability conditions can be qualified through inspection of the internal energy,  $U(x)$ , versus displacement curve shown in the right panel. Namely, these stability positions correspond to points of zero slope on the strain energy curve, *i.e.*  $\partial U / \partial x = 0$ . This is not surprising since mechanics relates internal energy, force,  $F(x)$ , and stiffness,  $k(x)$ , through the relations [3]

$$F(x) = \frac{\partial U(x)}{\partial x}, \quad (1)$$

and

$$k(x) = \frac{\partial F(x)}{\partial x} = \frac{\partial^2 U(x)}{\partial x^2}. \quad (2)$$

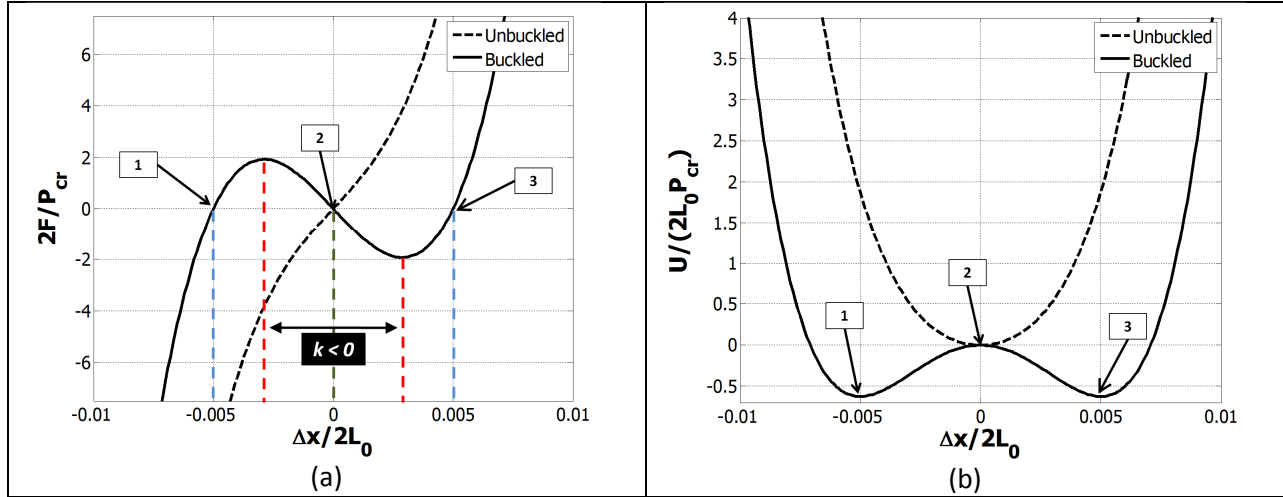


Figure 4: (a) Force versus displacement and (b) internal (strain) energy for a transversely loaded buckled beam such as the one shown in Figure 3.

Though these three configurations can be qualified as points of stability, physical intuition suggests that if one were to place the beam in position (2) it would not remain there when constraining forces are removed. This is a result of the fact that the position is not unconditionally stable, specifically, it is in a position of unstable equilibrium. For stable equilibrium, the change in the internal energy resulting from perturbations about the equilibrium position must be positive. Mathematically this means that the curvature, and therefore the stiffness, of the internal energy curve must be positive,  $\partial^2 U / \partial x^2 > 0$ .

This requirement implies that any deformation from the position leads to an increase in internal energy, which is another way of stating that a stable equilibrium position is one where the strain energy is at a local minimum, also known as an energy well [4]. Using this criteria, unconditional stability occurs at positions (1) and (3) where the slope of the internal energy curve is zero,  $\partial U / \partial x = F(x) = 0$ , and

where its curvature is positive,  $\partial^2 U / \partial x^2 = k(x) > 0$ . The unstable equilibrium position, configuration (2), is characterized as a point of zero force where the curvature of the internal energy curve is negative, *i.e.* a local maximum in the strain energy of the beam. Any unconstrained beam in this configuration will immediately be driven to one of the two unconditionally stable positions by any minor perturbation. Another very interesting point shown by Figure 4 is that the force-displacement curve for the buckled beam is non-monotonic. This implies that the slope, and therefore the stiffness, of the transverse force versus displacement of the buckled beam will display negative stiffness. In other words, the existence of a bistability alone implies that negative stiffness behavior exists and may potentially be advantageously used.

The force and internal energy versus displacement curves very clearly illustrate why the two scenarios discussed above will display negative stiffness. In the first case, when the beam is driven from one bistability to the other, the stiffness offered by the beam is negative between inflection points of

the internal energy curve. This region is highlighted in the left panel of Figure 4. In the second scenario, the beam is constrained to position (2), which is a local maximum in strain energy. As was pointed out above, a local maximum in internal energy corresponds to a region of negative curvature in the energy curve. Because the stiffness of the element is equal to the curvature of the internal energy curve, the beam will categorically display negative stiffness in the region for all perturbations about its constrained position. The constrained behavior of the system, referred to above as CNS, is not limited to large displacements and is therefore of high interest for vibroacoustic damping applications.

It is the focus of this portion of the project to exploit the unique non-monotonic force-displacement nature of bistable systems to produce highly absorptive composite materials. This can be achieved by designing and then embedding negative stiffness inclusions in a continuous viscoelastic matrix to effectively enhance the damping properties of the matrix material. As such, the objectives of this portion of the research were to (i) discover microstructure(s) that displays negative stiffness and (ii) validate a design approach using finite element analysis (FEA) that has the ability to quantify various microstructures that yield negative stiffness and approximate their behavior as an effective stiffness tensor.

#### 4.1.2 Mesoscale inclusion characterization

Though modeling conceptually begins at the microscale, it is practically useful to begin with a discussion of the mesoscale inclusion properties. Namely, it is of interest to detail how to reliably approximate a mesoscopic effective stiffness tensor,  $C_{ijkl}^m$ , of an inclusion with arbitrary internal geometry based on its stress-strain (force-displacement) behavior when subjected to various loading conditions. With a reliable method to approximate mesoscopic stiffness in place, it is then possible to focus on direct analysis and design of the inclusion microstructure. The work carried out during this project employed two approaches to calculate the effective mesoscopic stiffness. The first is referred to as the *direct energy* method which is reliable for linear elastic materials and structures. The second is called the *energy derivative* method which is well suited for materials and structures that display nonlinear constitutive stress-strain relationships.

The method referred to as the direct energy method is one that was employed by Odegard to calculate the effective behavior of a representative volume element of multiphase continuous piezoelectric materials using FEA [5]. The methodology is straightforward and involves computing the change in internal energy within a material volume, known as the representative volume element (RVE), which is assumed to represent the overall response of the material of interest when the volume is subjected to a prescribed set of boundary displacements. The mathematical details are summarized by Eqs. (3)-(7) and Table 1. Using the Einstein's summation convention for indicial notation, the linear elastic constitutive equation relating stress,  $\sigma_{ij}$ , and strain,  $E_{kl}$ , in stiffness form is

$$\sigma_{ij} = C_{ijkl} E_{kl}, \quad (3)$$

where  $C_{ijkl}$  is the stiffness tensor of the material (tacitly assumed to be linear in this formulation) and the (Green's) strain at a material point defined as the symmetric part of the gradient of the displacement field,  $E_{kl} = (u_{k,l} + u_{l,k})/2$ . The change in specific internal energy at a material point,  $U_E^{sp}$ , due to an imposed strain is given by

$$U_E^{sp} = \frac{1}{2} \sigma_{ij} (E_{ij}) E_{ij} \approx \frac{1}{2} C_{ijkl} E_{kl} E_{ij}. \quad (4)$$

Note that the middle equality in Eq. (4) is valid for materials with arbitrary elastic stress-strain relations while the approximate equality on the far right-hand side (RHS) is true for linear elastic materials for all imposed strains or nonlinear elastic materials in the limit where the imposed displacements at the boundaries are small. For orthotropic materials, Eq. (3) can be represented as follows with Voigt notation

$$\begin{bmatrix} \sigma_{11} \\ \sigma_{22} \\ \sigma_{33} \\ \sigma_{23} \\ \sigma_{13} \\ \sigma_{12} \end{bmatrix} = \begin{bmatrix} C_{11} & C_{12} & C_{13} & 0 & 0 & 0 \\ C_{12} & C_{22} & C_{23} & 0 & 0 & 0 \\ C_{13} & C_{23} & C_{33} & 0 & 0 & 0 \\ 0 & 0 & 0 & C_{44} & 0 & 0 \\ 0 & 0 & 0 & 0 & C_{55} & 0 \\ 0 & 0 & 0 & 0 & 0 & C_{66} \end{bmatrix} \begin{bmatrix} \varepsilon_{11} \\ \varepsilon_{22} \\ \varepsilon_{33} \\ \gamma_{23} \\ \gamma_{13} \\ \gamma_{12} \end{bmatrix}, \quad (5)$$

where  $E_{ij} \rightarrow \varepsilon_{ij}$  indicating small strains and  $\gamma_{ij} \equiv 2\varepsilon_{ij}$  to preserve symmetry.

Using COMSOL Multiphysics finite element modeling software, homogeneous strains are applied at boundaries of a cube of material. At boundary,  $B$ , the displacements,  $u_i(B)$ , can be related to the imposed strain,  $\varepsilon_{ij}^0$ , and the dimension of the RVE cube,  $L_m$ , in a general way by

$$u_i(B) = \varepsilon_{ij}^0 L_m n_j, \quad (6)$$

where  $\mathbf{n}$  is the unit normal vector of the RVE face where the displacement is imposed. Note that this formulation has made the assumption that the strain in the RVE is well represented as being homogeneous within the RVE. The resulting total elastic strain energy is then defined by the following relation:

$$U_E = \sum_{m=1}^n U_E^m = \frac{V}{2} C_{ijkl} \varepsilon_{ij}^0 \varepsilon_{kl}^0, \quad (7)$$



where  $U_E^m$  is the elastic strain energy of element  $m$ ,  $n$  is the total number of finite elements and  $V$  is the volume of the cube. The total energy is then summed over the entire volume. In order to determine the elements of the stiffness tensor it suffices to work out the mathematical relations of specific applied boundary conditions and the resulting strain energies by dividing the strain energy by the imposed strain and a constant. Table 1 summarizes the boundary conditions and related strain energy relations for the nine independent constants of an orthotropic material.

**Table 1: Summary of the displacements and expressions to determine the independent constants of an orthotropic medium using the direct energy approach.**

Property	Applied strain	Displacements	Elastic energy
$C_{11}$	$\varepsilon_{11}^0 = \varepsilon^0$	$u_1(B) = \varepsilon^0 L_m n_1$ $u_2(B) = 0$ $u_3(B) = 0$	$U_E = \frac{V}{2} C_{11} (\varepsilon^0)^2$
$C_{22}$	$\varepsilon_{22}^0 = \varepsilon^0$	$u_1(B) = 0$ $u_2(B) = \varepsilon^0 L_m n_2$ $u_3(B) = 0$	$U_E = \frac{V}{2} C_{22} (\varepsilon^0)^2$
$C_{33}$	$\varepsilon_{33}^0 = \varepsilon^0$	$u_1(B) = 0$ $u_2(B) = 0$ $u_3(B) = \varepsilon^0 L_m n_3$	$U_E = \frac{V}{2} C_{33} (\varepsilon^0)^2$
$C_{44}$	$\varepsilon_{23}^0 = \gamma^0/2$	$u_1(B) = 0$ $u_2(B) = (\gamma^0/2) L_m n_3$ $u_3(B) = (\gamma^0/2) L_m n_2$	$U_E = \frac{V}{2} C_{44} (\gamma^0)^2$
$C_{55}$	$\varepsilon_{13}^0 = \gamma^0/2$	$u_1(B) = (\gamma^0/2) L_m n_3$ $u_2(B) = 0$ $u_3(B) = (\gamma^0/2) L_m n_1$	$U_E = \frac{V}{2} C_{55} (\gamma^0)^2$
$C_{66}$	$\varepsilon_{12}^0 = \gamma^0/2$	$u_1(B) = (\gamma^0/2) L_m n_2$ $u_2(B) = (\gamma^0/2) L_m n_1$ $u_3(B) = 0$	$U_E = \frac{V}{2} C_{66} (\gamma^0)^2$
$C_{12}$	$\varepsilon_{11}^0 = \varepsilon_{22}^0 = \varepsilon^0$	$u_1(B) = \varepsilon^0 L_m n_1$ $u_2(B) = \varepsilon^0 L_m n_2$ $u_3(B) = 0$	$U_E = \frac{V}{2} \left[ C_{11} (\varepsilon^0)^2 + C_{22} (\varepsilon^0)^2 + 2C_{12} (\varepsilon^0)^2 \right]$

Property	Applied strain	Displacements	Elastic energy
$C_{23}$	$\varepsilon_{22}^0 = \varepsilon_{33}^0 = \varepsilon^0$	$u_1(B) = 0$ $u_2(B) = \varepsilon^0 L_m n_2$ $u_3(B) = \varepsilon^0 L_m n_3$	$U_E = \frac{V}{2} \left[ C_{22} (\varepsilon^0)^2 + C_{33} (\varepsilon^0)^2 + 2C_{23} (\varepsilon^0)^2 \right]$
$C_{13}$	$\varepsilon_{11}^0 = \varepsilon_{33}^0 = \varepsilon^0$	$u_1(B) = \varepsilon^0 L_m n_1$ $u_2(B) = 0$ $u_3(B) = \varepsilon^0 L_m n_3$	$U_E = \frac{V}{2} \left[ C_{11} (\varepsilon^0)^2 + C_{33} (\varepsilon^0)^2 + 2C_{13} (\varepsilon^0)^2 \right]$

Research during this project has illustrated that the direct energy method is ill-suited to determine the stiffness of structures displaying negative stiffness. There are two primary reasons for this shortcoming. First, the direct energy approach is formulated such that minor errors in the calculated strain energy can result in very large errors in the stiffness coefficient estimate because of the requirement of small imposed strains and the presence of the strain in the denominator of the stiffness calculation. Second, if the material or microstructure exhibits nonlinear stress-strain behavior, this approach has the potential to produce non-physical stiffness results. Given that the focus of the current research is the determination of inclusion structures that display negative stiffness, and that negative stiffness requires the presence of bistability, which is inherently nonlinear, the direct energy approach is likely to provide erroneous estimates of the stiffness of the structures of interest.

Fortunately, a method that uses much the same approach, what developed by the PI and has been named the *energy derivative method*. This approach can be implemented to estimate the effective nonlinear behavior of a structure that undergoes finite deformation and does not have the weaknesses of the direct approach. Much like the direct approach described above, the energy derivative method also applies prescribed strains on the surface of the RVE and calculates the resulting strain energy. The primary difference is that the energy derivative method requires the calculation of the strain energy for a large range of imposed deformations. Once the resulting strain energies are calculated, the stiffness of the element at a specified strain can be calculated from the determination of the local curvature of the strain energy versus strain plot. This approach does not require the stress-strain relation to be linear thereby implying that only the very general center equality of Eq. (4) hold. Research conducted during this project has shown that the energy derivative method is a robust approach for determining local stiffness and eliminates the error amplification inherent in the direct approach. Equations (8)-(10) describe the relationships between the strain energy curves created by applying a range of deformations at the boundaries of the RVE similar to those given in Table 1 and the nonlinear stiffness curves for the mesoscopic structure. Specifically, the total strain energy is related to the assumed homogeneous stress and strain fields as

$$U_E = \sum_{m=1}^n U_E^m = \frac{V}{2} \sigma_{ij} (E_{ij}) E_{ij}. \quad (8)$$

This implies that the stress at any strain level can be computed from the derivative of the strain energy – strain curve:

$$\sigma_{ij}(\varepsilon_{ij}) = \frac{2}{V} \frac{\partial U_E(\varepsilon_{ij})}{\partial \varepsilon_{ij}}. \quad (9)$$

Finally, the local stiffness is then simply found as the curvature of the strain energy versus strain curve,

$$C_{ijkl}(E_{ij}) \equiv \frac{\partial \sigma_{ij}(E_{ij})}{\partial \varepsilon_{kl}} = \frac{2}{V} \frac{\partial^2 U_E(E_{ij})}{\partial E_{ij}^2}. \quad (10)$$

Equation (10) implies that the prescribed displacements in Table 1 can be applied to an arbitrary RVE for varying magnitudes of displacement and the resulting total elastic strain energy in the RVE can be computed due to these imposed strains. Calculations of the local curvature at any given displacement (or strain) can then be related to the corresponding inclusion stiffness through Eq. (10). This approach is first benchmarked in Section 4.1.3 and then employed to calculate the effective mesoscopic stiffness of a candidate microstructure in Section 4.1.4.

#### 4.1.3 Benchmarking the energy derivative approach

To benchmark the energy derivative approach, FEA was carried out on a solid block of isotropic steel ( $E = 200$  GPa,  $\nu = 0.33$ ). The following figures contain the respective strain energy-displacement, force-displacement and stiffness-displacement values for  $C_{11}$ ,  $C_{12}$  and  $C_{66}$ . Neglecting numerical round-off from derivative calculations, the values converge to 296 GPa, 146 GPa and 75.2 GPa, respectively, for the full range of imposed displacement. These values are equivalent to the known properties of isotropic steel, providing a good initial benchmark of the energy derivative approach.

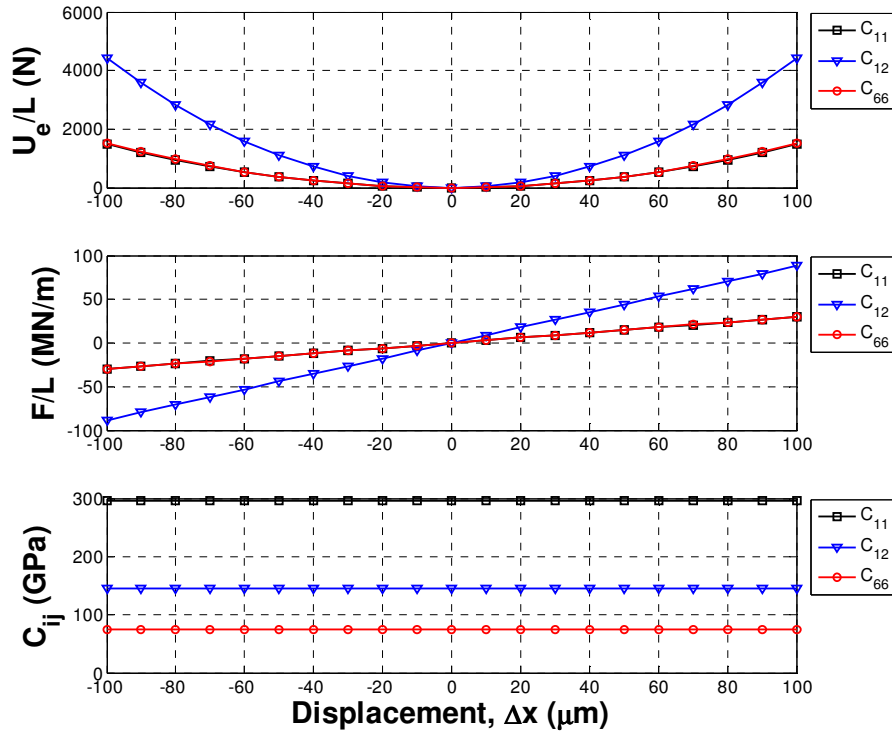


Figure 5: Calculated strain energy, force, and stiffness as a function of displacement imposed on the RVE for a steel cube using the energy derivative approach. For steel  $C_{11} = \lambda + 2\mu = 296$  GPa,  $C_{12} = \lambda = 146$  GPa and  $C_{66} = \mu = 75.2$  GPa.

To provide a more robust benchmark of the energy derivative approach, it is of interest to model the behavior of a heterogeneous system and compare the FEA results to results from well-established EMT. This was accomplished by modeling a RVE consisting of a cube of steel containing a spherical void of varying volume fraction. The same process for obtaining stiffness values was performed on this RVE as for the homogeneous cube and the results are displayed in Figure 6. This figure contains three plots, one of each constant of interest ( $C_{11}$ ,  $C_{12}$  and  $C_{66}$ ) for the heterogeneous RVE as the void fraction is varied from 0 to 20% by volume. The values are normalized by the element of the stiffness tensor of steel. The curves clearly show very strong agreement with the analytical models which provides a very reliable benchmark of the energy derivative approach for approximating the overall properties of a heterogeneous RVE. With a method for approximating the effective properties of a structured inclusion in place, attention is now turned to modeling microstructural elements that display negative stiffness.

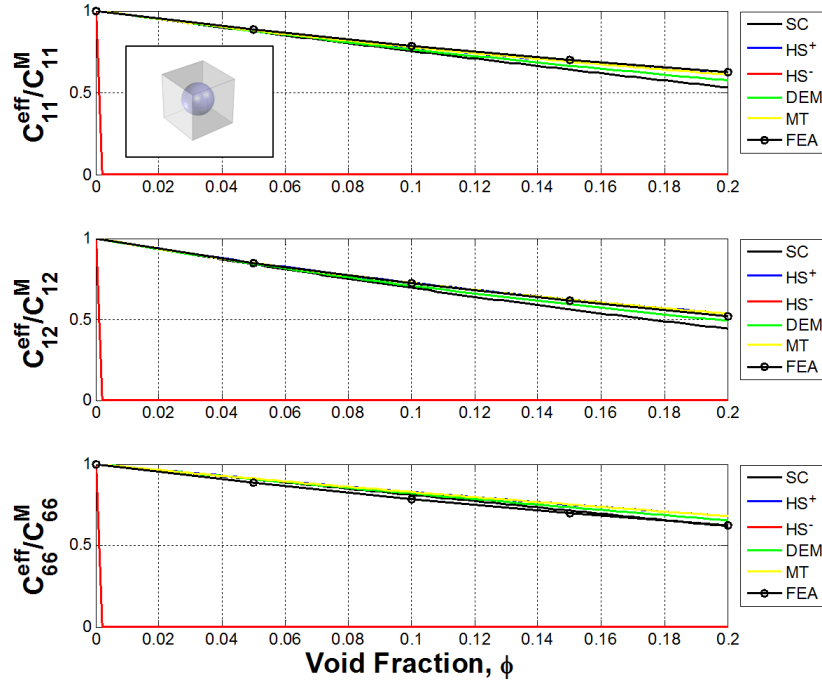


Figure 6: Effective properties of a RVE of steel containing varying amounts of spherical void (see inset in top panel). Stiffness values were calculated in FEA using the derivative approach and are compared with analytical estimates using the Self-Consistent (SC), Differential Effective Medium (DEM), and Mori-Tanaka (MT) models along with the Hashin-Shtrikman Upper (HS<sup>+</sup>) and lower (HS<sup>-</sup>) bounds.

#### 4.1.4 Microstructure modeling

As mentioned at the outset of this section, the physics underlying negative stiffness behavior that is of interest to this work is found and easily illustrated through an investigation of a buckled beam. For this reason, it is of interest to investigate a buckled beam through both analytical and FE methods. This serves the dual purpose of providing a clear example of the desired system behavior and a benchmark of FE modeling of post-buckled beam behavior. Consider the system shown in Figure 7 consisting of a beam with fixed ends subjected to both axial and transverse forces labeled as  $N$  and  $P$ , respectively.

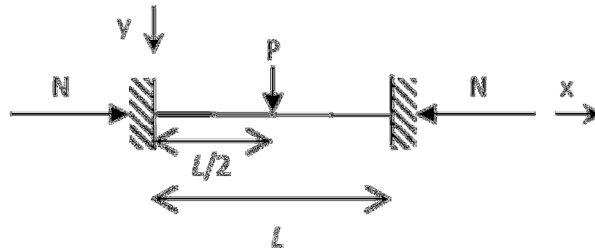


Figure 7: Geometry and variables for analysis of the behavior of pre- and post-buckled beam.

Through bending analysis, it can be shown that the transverse beam stiffness at the center of the beam,  $k_b$ , is equal to:

$$k_b = \frac{Pk}{\tan(kL/4) - kL/4}, \quad (11)$$

where  $k = \sqrt{N/EI}$ ,  $E$  is the Young's modulus of the beam materials, and  $I$  is the bending moment of inertia of the beam. One can also readily plot transverse stiffness versus axial compression, shown in Figure 8, by relating the axial compression force,  $N$ , to the resulting compressive displacement along the beam axis,  $u$ , with  $u = NL/AE$ .

Equation (11) and the relations above can be used to validate FEA results for a 2D plane-strain beam. A simple beam model was created for an alumina ( $E = 386$  GPa,  $\nu = 0.22$ ) beam of length .0017m and height of 50  $\mu\text{m}$ . A point displacement of 1  $\mu\text{m}$  was applied at the center-top of the beam at the same time as the beam ends were subjected to varying axial compressive displacements. The reaction force in the  $y$ -direction was monitored at the point of imposed displacement and the transverse stiffness of the system at the center was then calculated by noting that  $k_b^{FEA} \approx F_y^{\text{meas}} / u_y^{\text{imposed}}$ . Transverse stiffness values obtained using FEA and Eq. (11) are plotted in Figure 8 for varying amounts of axial compression. The results indicate a very good agreement between the analytical and FEA models. The slight deviations are attributed to discrepancies between the analytical equation which assumes a 1D beam and the 2D plane-strain approximation used in FEA. For the purposes of this research, these results validate this FEA approach for modeling pre- and post-buckled beam behavior. It is noteworthy that the stiffness curve crosses the point of zero stiffness for an axial compression of 480 nm. This value is equivalent to the critical compression load,  $N_{\text{critical}}$ , *i.e.* the loading at which buckling occurs, and is relevant to the discussion of the results that are presented below.

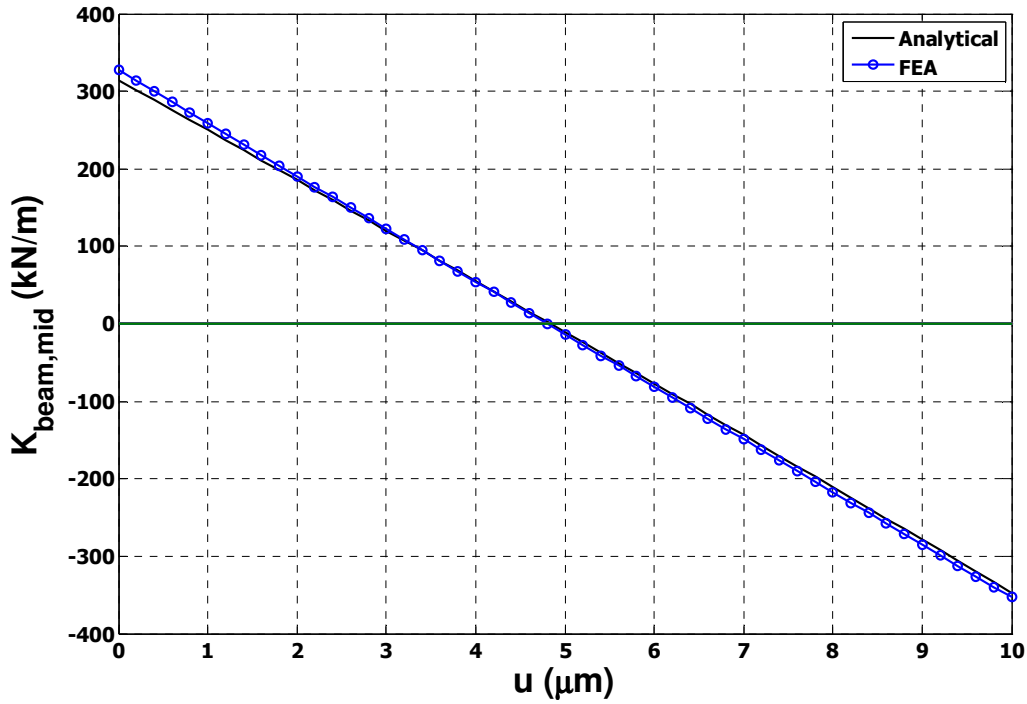


Figure 8: Transverse stiffness of a beam with a prescribed axial compression.

To further explore the FEA model, several studies were performed in order to validate the ability of the FE model to capture negative stiffness behavior. Specifically, the beam was subjected to 3 levels of compression:  $u = 0$ ,  $u = u_{\text{critical}}$ ,  $u > u_{\text{critical}}$  and the results are shown in Figure 9. In the first case, the beam acts as a conventional positive stiffness system. That is, the transverse force versus displacement curve is monotonically increasing and the strain energy has a minimum value at  $\Delta x = 0$ . This is reflected in the  $L = L_0$  case shown in Figure 9. As the amount of compression increases to the point of criticality, the stiffness approaches zero for  $\Delta x = 0$ . This is shown in Figure 9 as the slope of the force-displacement curve for the  $N = N_{\text{critical}}$  case is shown to be nearly zero for a range of displacement values around  $\Delta x = 0$  and the strain energy has a broad range of displacements around  $\Delta x = 0$  for which it is nearly constant. A buckled beam behaves quite different than both of the previous configurations. Starting at the first zero crossing on negative displacement part of the curve of Figure 9, the beam initially resists a transverse displacement by requiring increasing force to impose a displacement. As the displacement increases to a critical value, the beam will show decreasing incremental changes in force for an increase in displacement until it reaches the second zero crossing in the positive range of the imposed displacement. This behavior is indicated by the double-well nature of the strain energy curve for the 'Buckled' case in Figure 9. The results for these three different axial loading conditions are in very good agreement with the discussion about negative stiffness systems in Section 4.1.1 and the FEA approach is therefore validated for finite deformation systems that display negative stiffness.

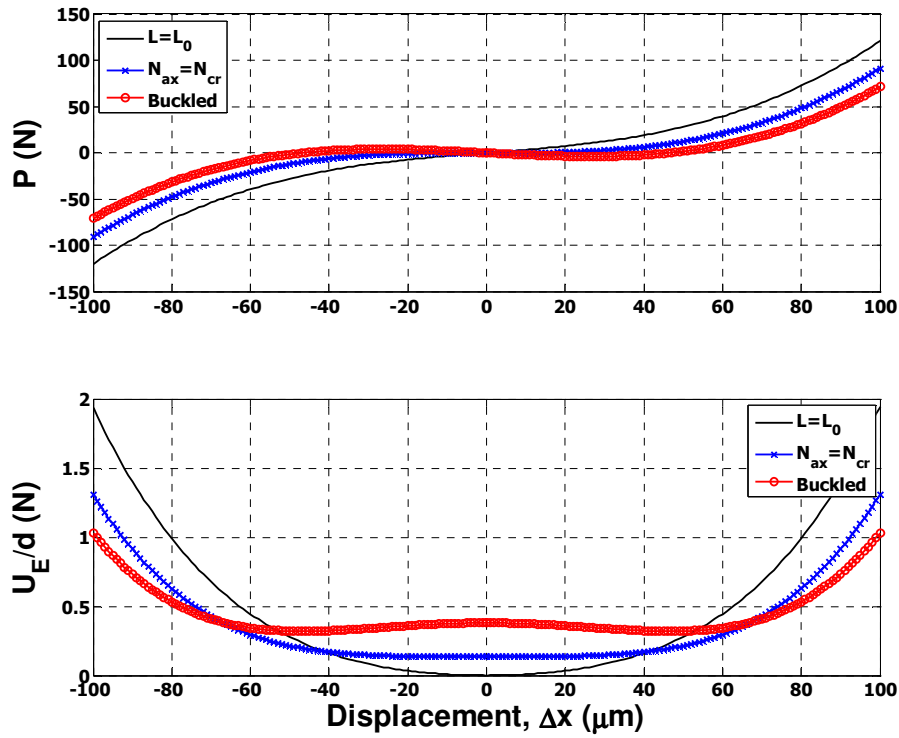


Figure 9: FEA results of the Force (top) and strain energy per beam width (bottom) versus displacement curves for a beam with varying axial load.

As mentioned in Section 4.1.1, the fact that negative stiffness implies the presence of a local increase in strain energy, they can only exist if constrained within an overall positive stiffness system which allows energy to be ‘stored’ locally in the negative stiffness system. When perturbed from this constrained position, NS systems can release more energy into their constraining systems than the energy input by external sources. This is the key point of the use of NS elements to absorb energy: negative stiffness systems can be used to perform work on their external constraining system. If the surrounding medium is lossy, then the presence of a NS domain will provide more energy to work that surrounding medium and thereby increase the absorptive capacity of the overall system. This is the basis of hypotheses of extreme damping using negative stiffness systems [6].

#### 4.1.5 Mesoscale inclusion modeling and design

The current inclusion design mimics a buckled beam system on four of the six faces of a cube to induce negative stiffness in two orthogonal directions. The structure shown in Figure 10 was designed to take advantage of a fabrication process known as micro co-extrusion which could be leveraged to fabricate and employ a coefficient of thermal expansion mismatch between  $\text{Al}_2\text{O}_3$  (alumina) and  $\text{Y}_2\text{O}_3$  Partially Stabilized Zirconia (YTZP), two ceramics that can be polymerized for co-extrusion, to produce buckled elements. Given a sufficient change in temperature, ample axial compression can be generated to buckle the alumina ‘web’ elements depicted in Figure 10. Attached to the web is a YTZP interface to the matrix material which will surround the mesoscale inclusions. The YTZP interface acts as a



distributed to point force translator to ensure that as much external loading is applied directly to the center of the web as possible. Without this concentration of force at the center of the web, FEA has shown that the web can contort into secondary modes, limiting or even eliminating its NS response.

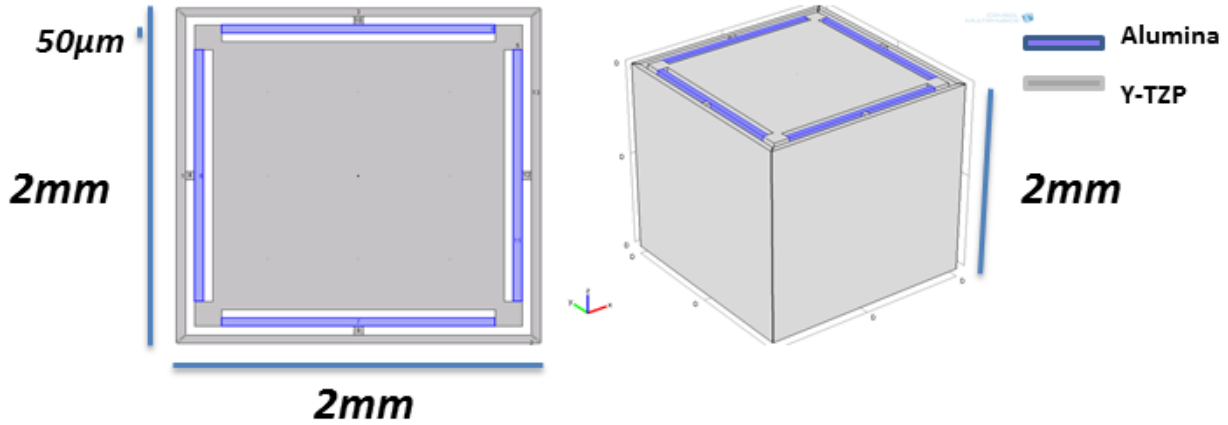


**Figure 10: Mesoscale inclusion with microscale structure that leads to negative stiffness in two dimensions. The inclusion is assumed to be fabricated from YTZP and alumina materials that employ thermal expansion mismatches to induce buckling.**

The objective for the design of the microstructure is ultimately to tailor design parameters for an existing application while considering existing manufacturing processes for future implementation. This means that the trade-space will be constrained not only with regard to material selection (for instance, materials similar to the ceramics indicated above), but geometry as well. Because 50  $\mu\text{m}$  is considered the smallest dimension that can be readily manufactured using micro co-extrusion, the initial design has restricted the smallest feature size to be a maximum of 50  $\mu\text{m}$ . As of the termination of this project, no further manufacturing processes have been considered. However, it is worth noting that a robust multiscale model coupled with the design space exploration methods described in Section 4.1.11 permit optimization of negative stiffness behavior through the alteration of inclusion structure rather than focusing on a specific manufacturing technique. This opens the door to evaluating what can be achieved within the limits of a specific manufacturing process rather than searching for a design process that can achieve the performance predicted by a specific geometric configuration.

#### 4.1.6 FEA of candidate negative stiffness mesoscale inclusion

Characterization of the temperature depending effective elastic constants of structured inclusions like the one shown in Figure 10 requires the implementation of a multi-step FEA study that considers both the thermal and mechanical deformation. The process devised requires two discrete steps. The first step is to solve the free thermal deformation for any given temperature change. The resulting deformed state of the current inclusion structure is shown in the top left image of Figure 11. The resulting displacements are monitored at the external boundaries of the inclusion. These displacements signify the new thermal equilibrium positions of the inclusion boundaries. The second step then simultaneously solves for the thermal deformation and the prescribed strain as outlined in Table 1 in order to determine each independent elastic constant of the mesoscale inclusion. The symmetries contained in the geometry lead to the observation that  $C_{11} = C_{22}$ ,  $C_{13} = C_{23}$ , and  $C_{44} = C_{55}$  leaving

the only independent constants to determine as  $C_{11}$ ,  $C_{33}$ ,  $C_{12}$ ,  $C_{23}$ ,  $C_{44}$ , and  $C_{66}$ . Figure 12 – Figure 18 show the results of this analysis for all independent constants of the inclusion while Figure 10 shows the deformed fields for a few representative loading conditions to aid in understanding the process.

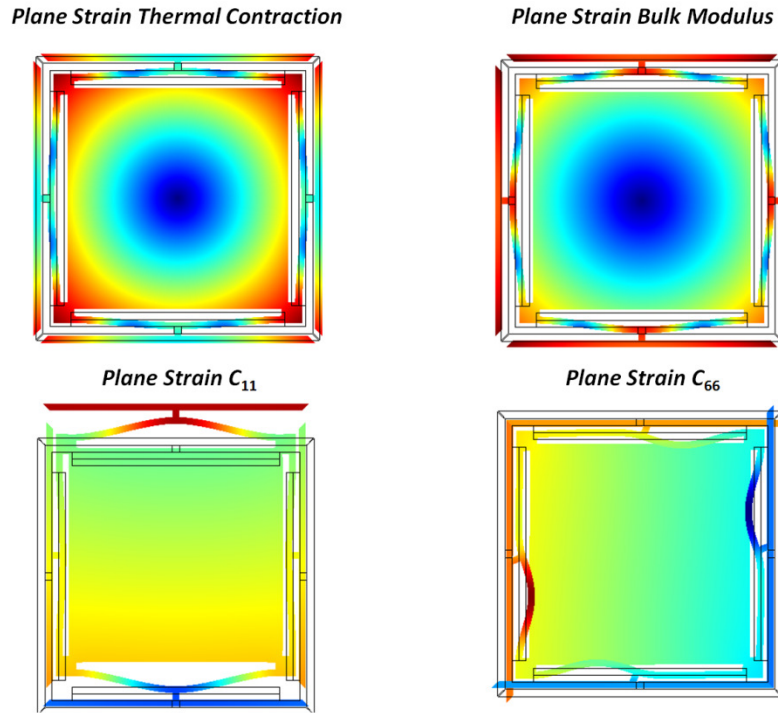


**Figure 11: Representative deformed microstructures showing the results of the thermal contraction-induced buckling and imposed displacements to determine strain energy curves for effective mesoscopic constant calculation. The deformed geometric is greatly exaggerated for easy visualization.**

The first set of results, shown in Figure 12, depicts the normalized strain energy and effective stiffness resulting from a plane-strain area change (equal displacements along orthogonal directions) for differing imposed temperature changes. The stiffness value resulting from this set of boundary conditions is the 2D bulk modulus,  $K_{2D}$ . The strain energy curves for large temperature change show two energy wells, clearly indicating bistable behavior. Consequently, the lower panel shows that for a range of imposed displacements the effective 2D bulk modulus will be negative. It is worth noting that the strain energy curve is not symmetric about the local maximum. This is due to the fact that the inclusion geometry is such that the ‘buckled-out’ configuration (shown in Figure 11) has lower energy levels than does the ‘buckled-in’ configuration. This does not change the fact that NS will be observed as is evidenced by the lower panel in Figure 12.

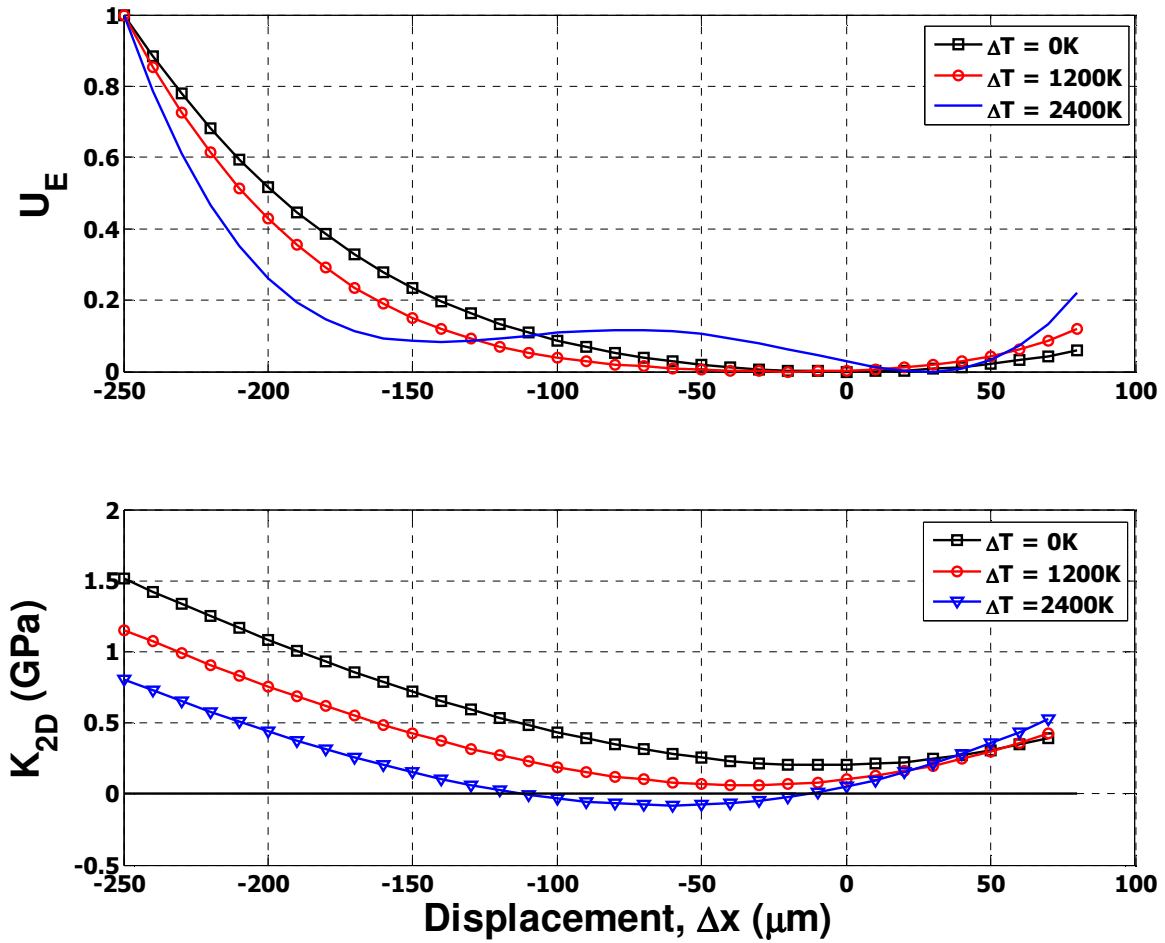


Figure 12: Effective 2D plane strain bulk modulus of the candidate microstructure for various imposed displacements for various changes in temperature. Top panel shows the strain energy curves (normalized by their maximum value) and the bottom panel shows the bulk modulus.

The results shown in Figure 12 suggest that the current inclusion design will indeed show negative stiffness given a certain level of temperature change to induce buckling in the ‘web’ elements. This is verified with the plots of the remaining effective stiffnesses in Figure 13 – Figure 18. Specifically, the constants  $C_{11} = C_{22}$  and  $C_{12}$  display negative stiffness behavior for a relatively large range of imposed displacements.

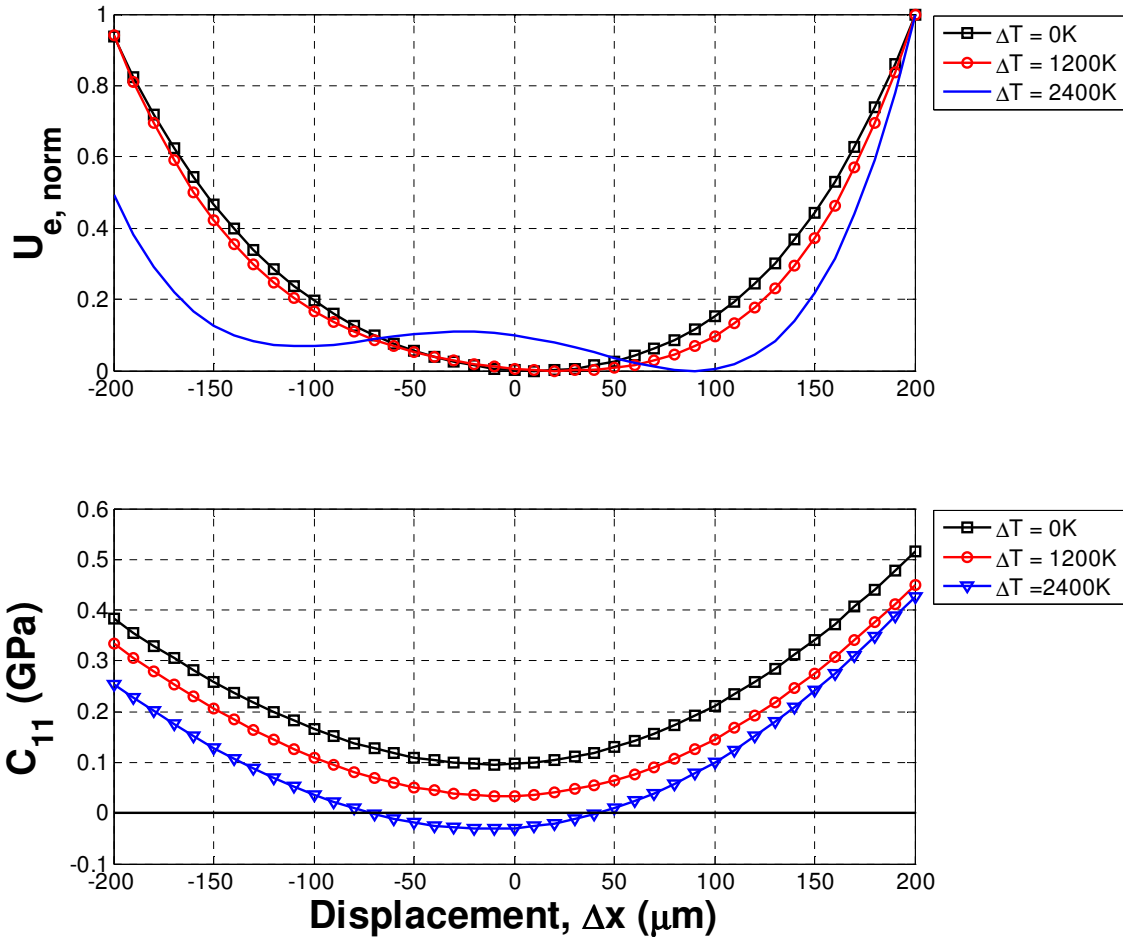


Figure 13: Effective plane wave modulus of the candidate microstructure along the  $x_1$  (and  $x_2$ ) direction at various imposed displacements and changes in temperature. Top panel shows the strain energy curves (normalized by their maximum value) and the bottom panel shows the modulus.

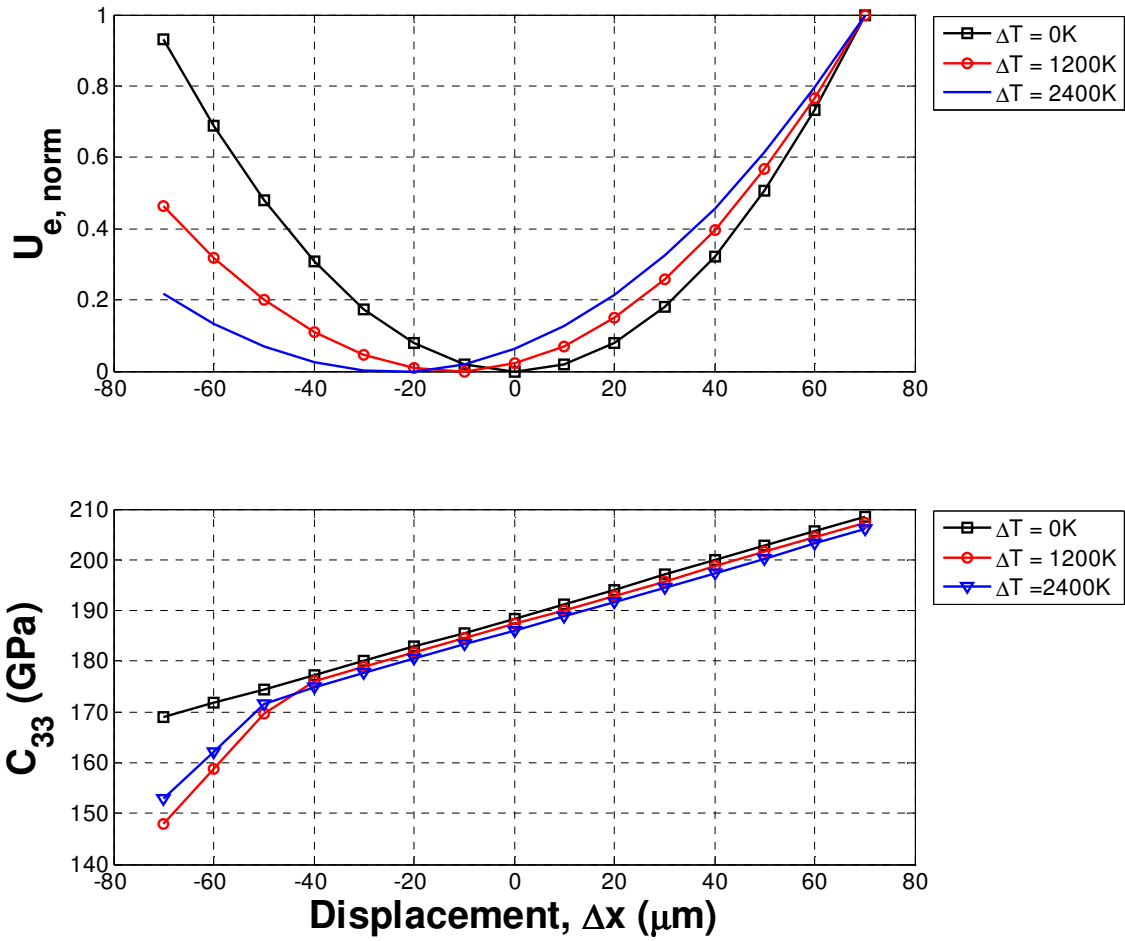


Figure 14: Effective plane wave modulus of the candidate microstructure along the  $x_2$  direction at various imposed displacements and changes in temperature. Top panel shows the strain energy curves (normalized by their maximum value) and the bottom panel shows the modulus.

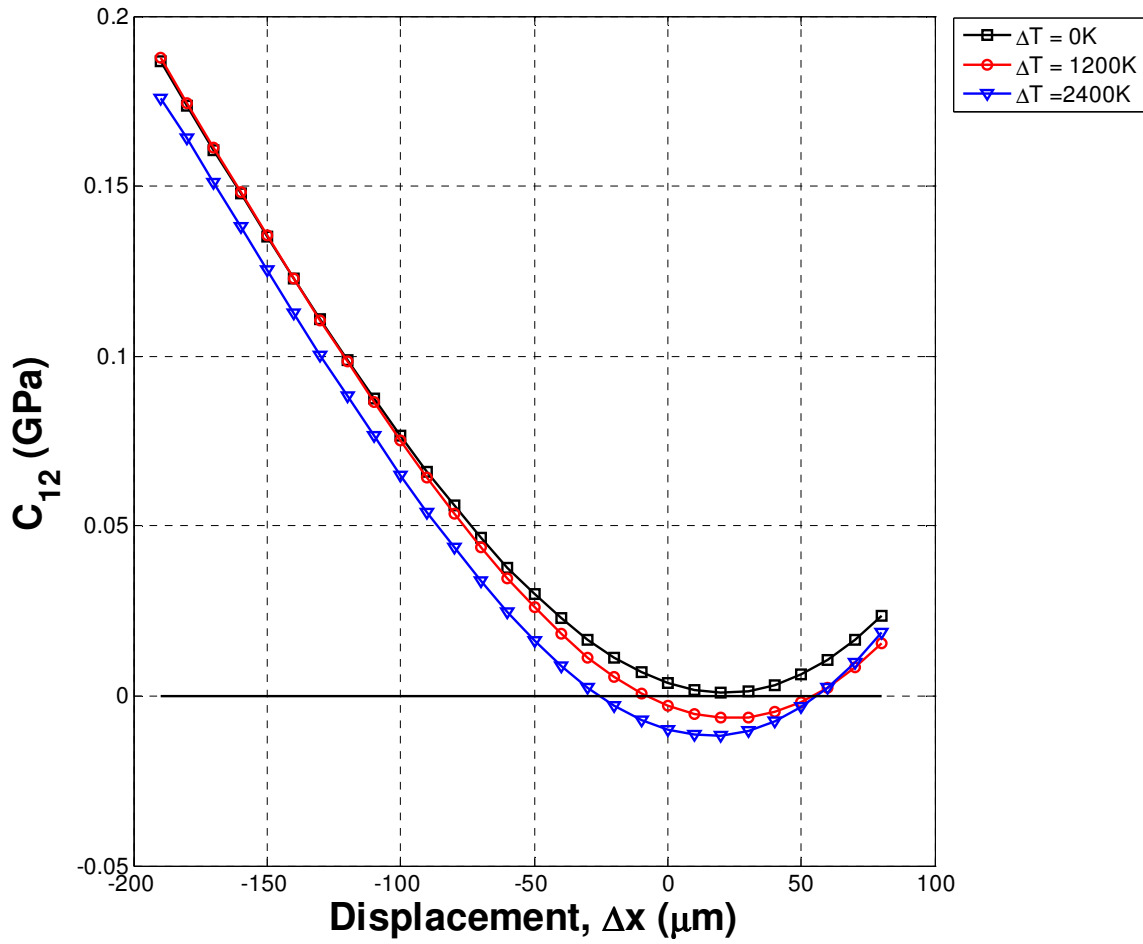


Figure 15: Effective dilatation modulus of the candidate microstructure in  $x_1 - x_2$  plane,  $C_{12}$ , at various imposed displacements and changes in temperature. As is shown in Table 1, this modulus is determined from the results of other moduli, so the strain energy curve is not shown.

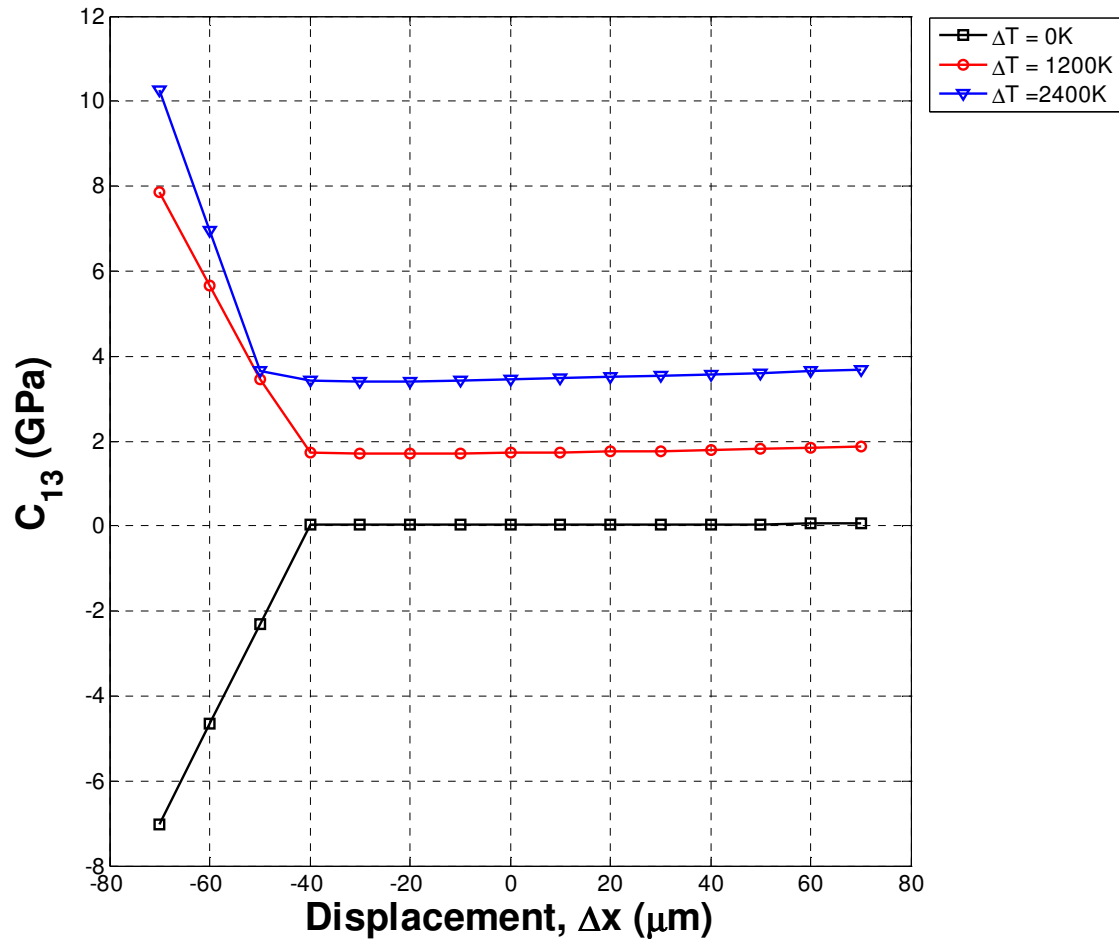


Figure 16: Effective dilatation modulus of the candidate microstructure in  $x_1-x_3$  plane,  $C_{13}$ , at various imposed displacements and changes in temperature. As is shown in Table 1, this modulus is determined from the results of other moduli, so the strain energy curve is not shown.

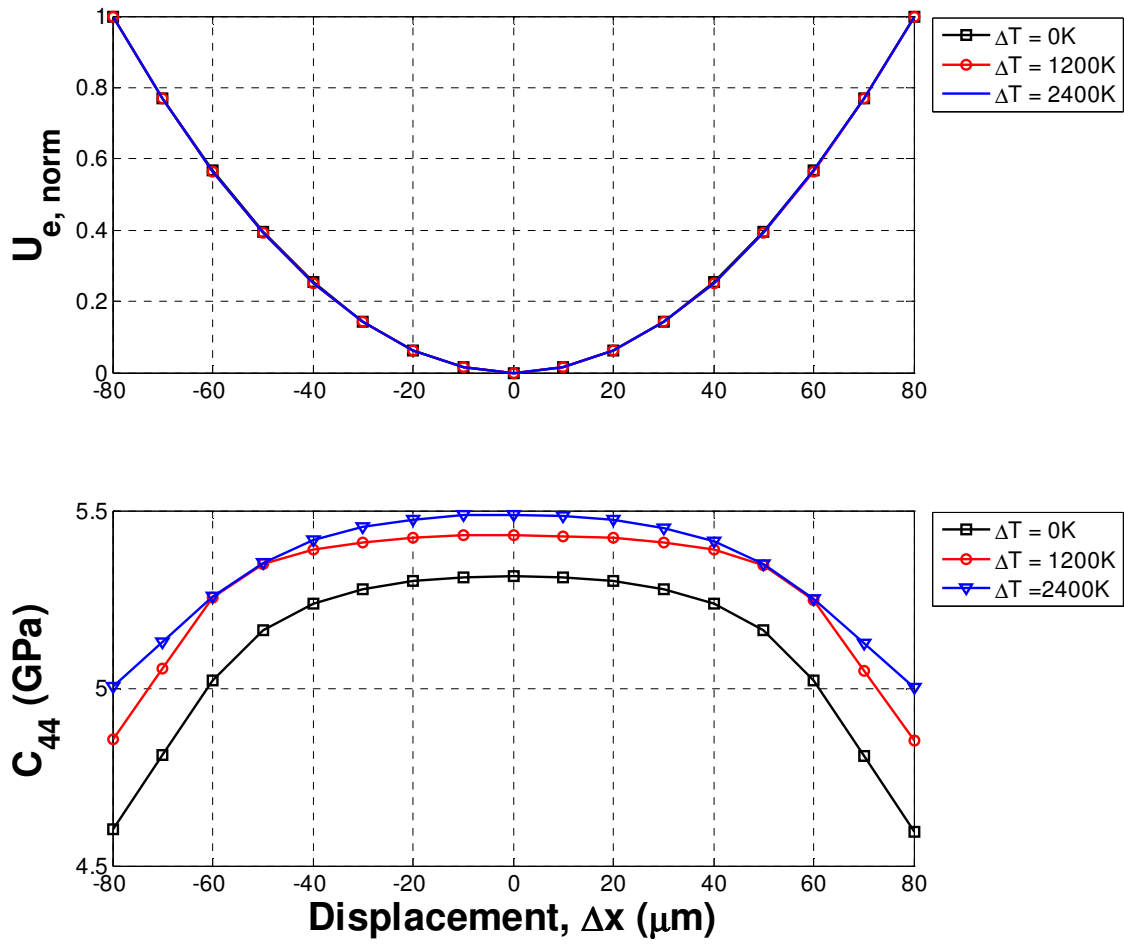


Figure 17: Effective shear modulus of the candidate microstructure in  $x_2 - x_3$  plane,  $C_{44}$ , at various imposed displacements and changes in temperature. Top panel shows the strain energy curves (normalized by their maximum value) and the bottom panel shows the modulus.



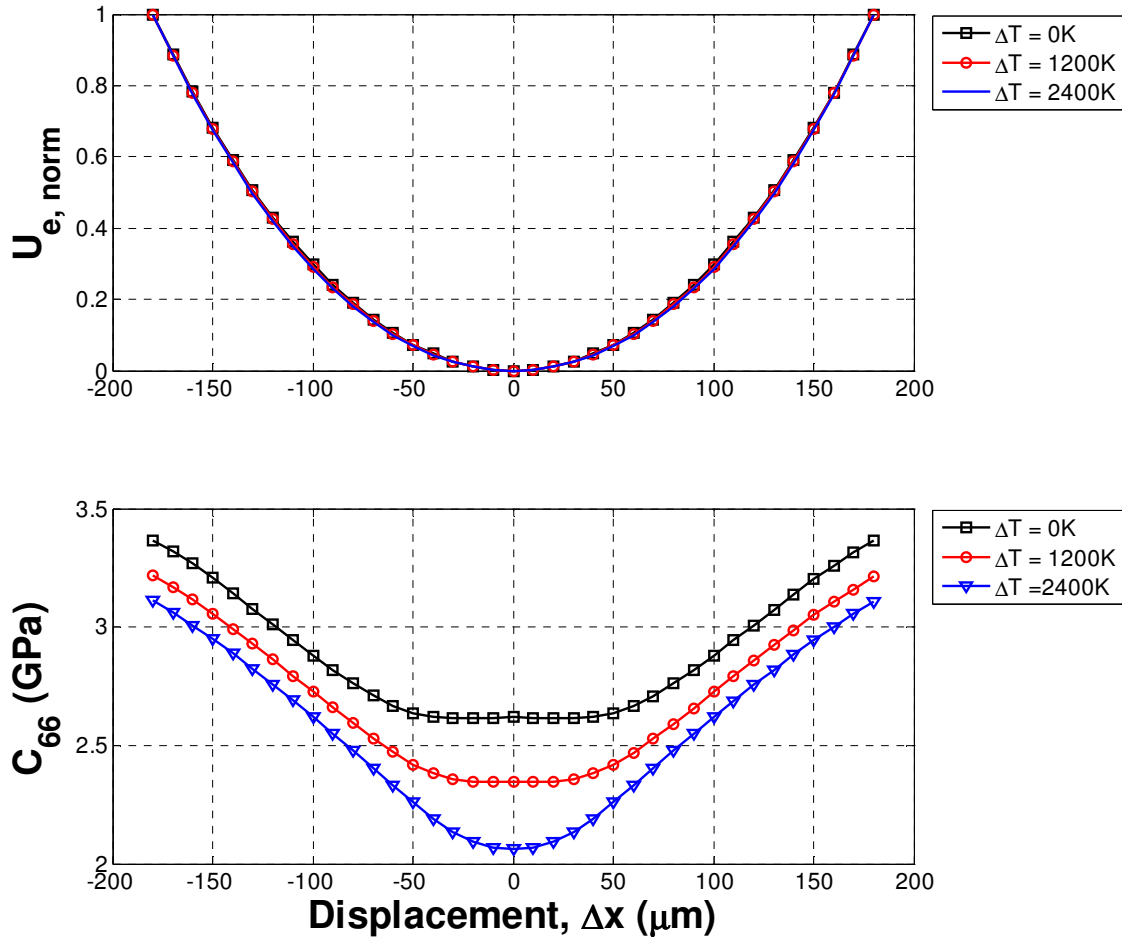


Figure 18: Effective shear modulus of the candidate microstructure in  $x_1 - x_2$  plane,  $C_{66}$ , at various imposed displacements and changes in temperature. Top panel shows the strain energy curves (normalized by their maximum value) and the bottom panel shows the modulus.

The above results validate the approach of exploiting a coefficient of thermal expansion mismatch to obtain a negative stiffness inclusion. It is important to note that the current level of temperature change required is too large for practical application, however we have established a benchmarked and validated approach for obtaining temperature-dependent inclusion stiffness values. Future work includes performing optimization of the inclusion structure and materials in order to bring the required temperature change down to a level that is practical for implementation using known processing techniques. Structure that displays negative stiffness but does not rely on temperature change, studied in micro-switch research, will also be investigated to remove that additional manufacturing difficulty.

#### 4.1.7 Mesoscale $\rightarrow$ mesoscale effective medium modeling

The remaining modeling step to complete the multi-scale model of our structured lossy composite material is the meso  $\rightarrow$  macro homogenization modeling step. This is completed by implementing an anisotropic EMT analysis that uses as an input the effective stiffness tensor of the mesoscale inclusion

introduced in the Sections 4.1.5 and 4.1.6. The micromechanical model employed is a three-phase coated inclusion self-consistent (SC) EMT developed in previous work [7]. The model employs localization and homogenization of the effects of viscoelastic contrast due to the presence of microscale coated inclusions, as indicated by the schematic in Figure 19. The model can consider inclusions of arbitrary anisotropic viscoelastic behavior, geometry, and orientation distribution to get a good approximation of the overall viscoelastic response of the medium and has been shown to have strong agreement with experimental data in static and quasistatic (inclusion size is much larger than propagating wavelengths) domains [7], [8]. The effective (complex valued) stiffness tensor of a composite containing coated inclusions are computed using Eqs. (12) – (16).

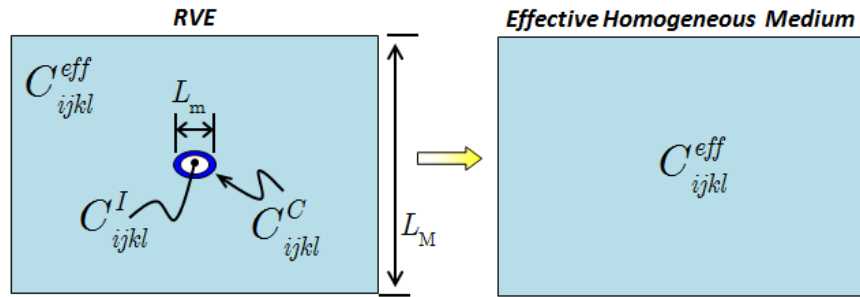


**Figure 19: Conceptual schematic of the homogenization approach of the Self-Consistent micromechanical model for a coated inclusion.**

In general, the SC model can be well understood as an intelligently weighted rule of mixtures approximation as shown in Eq. (12),

$$C_{ijkl}^{eff} = C_{ijkl}^M + f^I [C_{ijmn}^I - C_{ijmn}^M] A_{mnkl}^I + f^C [C_{ijmn}^C - C_{ijmn}^M] A_{mnkl}^C. \quad (12)$$

In this expression the stiffness tensors,  $\mathbf{C}^X$ , of each material are denoted with an  $M$ ,  $I$ , or  $C$  superscript to represent the matrix, inclusion or coating, respectively, and the tensors  $\mathbf{A}^I$  and  $\mathbf{A}^C$  represent quantities known as strain localization tensors for the inclusion and coating phases, respectively. The strain localization tensors relate the macroscopic strain,  $\varepsilon_{ij}^g$ , to the average inclusion (or coating) strain,  $\bar{\varepsilon}_{ij}^I$ , through the relation

$$\bar{\varepsilon}_{ij}^I = A_{ijkl}^I \varepsilon_{kl}^g. \quad (13)$$

For the current problem, the volume fraction of coating material is set equal to zero,  $f^C = 0$ , leaving only the inclusion fraction of inclusion,  $f^I$ , to influence the overall properties. The strain localization tensors represent the intelligent weighting parameters and have significant influence on the effective properties calculated. They take into account not only the material anisotropy of each constituent

phase, but also the inclusion form. For the special case of no coating, the inclusion strain localization tensor reduces to,

$$A_{ijkl}^I = \left[ I_{ijkl} + T_{ijmn}^I \left( C_{ijkl}^{eff} \right) \left( C_{mnkl}^I - C_{mnkl}^{eff} \right) \right]^{-1}, \quad (14)$$

where  $I_{ijkl} \equiv \mathbf{I}_4$  is the fourth order identity tensor and  $\mathbf{T}^I(\mathbf{C}^{eff})$  is the volume average of the volume integral of the what is known as the modified Green's tensor,  $G_{ij}^{eff}(\mathbf{r} - \mathbf{r}')$ ,

$$T_{ijkl}^I(C_{ijkl}^{eff}) = \frac{1}{V^I} \int_{V^I} \int_{V^I} -\frac{1}{2} \left[ G_{ik,jl}^{eff}(\mathbf{r} - \mathbf{r}') + G_{jk,il}^{eff}(\mathbf{r} - \mathbf{r}') \right]. \quad (15)$$

Here  $V^I$  represents the volume of the inclusion and the Green's tensor calculates the displacement in the  $i$ -direction at the point  $\mathbf{r}$  due to a unit force in the  $j$ -direction at resulting from an inhomogeneity located at point  $\mathbf{r}'$ .  $G_{ij}^{eff}(\mathbf{r} - \mathbf{r}')$  is defined as the tensor that satisfies the differential equation

$$C_{ijkl}^{eff} G_{km,lj}^{eff}(\mathbf{r} - \mathbf{r}') + \delta_{im} \delta(\mathbf{r} - \mathbf{r}') = 0. \quad (16)$$

Full evaluation of Eq. (15) is a non-trivial task and details of the Fourier transform technique for to find an approximate solution can be found in reference [9]. Further, inspection of Eq. (14) shows that the SC model is implicit and numerical methods are required for its implementation. However, it is known to provide very accurate solutions for a wide range of problems [7], so its use has been adopted for this project.

Using the results of the FEA presented in the previous sections to find the effective stiffness of the mesoscopic inclusion, Figure 20 shows the effective properties calculated for a composite containing 2% by volume of identically oriented microstructured NS inclusions. The matrix material was assumed to be isotropic and the real part of the plane wave modulus in the  $x_1$ -direction ( $C_{11}^M$ ) was calculated for various properties of the matrix,  $C_{11}^I / \mathbb{R}[C_{11}^M]$ , were calculated based on the results above where maximum negative plane-strain bulk modulus values were observed. The matrix was assumed to have a small loss factor,  $\eta^M = 0.05$  and its Poisson's ratio was set at  $\nu^M = 0.30$ . The results present the overall properties normalized by the properties of the matrix for a wide range of possible inclusion to matrix stiffnesses. The objective in making these plots is to determine what ratio of negative inclusion stiffness to matrix stiffness provides the desired overall performance. Inspection of the resulting effective anisotropic properties clearly show that drastic changes in overall stiffness and loss factor occur for stiffness ratios of  $C_{11}^I / \mathbb{R}[C_{11}^M] \in [-0.25 \quad -0.125]$  (approximately). Note that the scale of the normalized loss factor is logarithmic in order to clearly display the large range of increase due to the

inclusion of negative stiffness particles in the lossy matrix. The largest predicted increase occurs for the  $C_{12}^{eff}$  and  $C_{11}^{eff} = C_{22}^{eff}$ , which show maximum loss factor ratios of  $\approx 40\eta^M$  and  $\approx 10\eta^M$ , respectively. It is worth noting that these plots indicate that it is possible to *simultaneously* increase both the stiffness and loss of a composite compared to the matrix material by using just a very small amount of constrained NS inclusions. These encouraging results suggest that viscoelastic materials containing even very low volume fractions of inclusions structured as shown in Figure 10 will display drastic increases in energy absorption while the change in overall stiffness can be tuned based on the ratio of the inclusion to matrix stiffness.

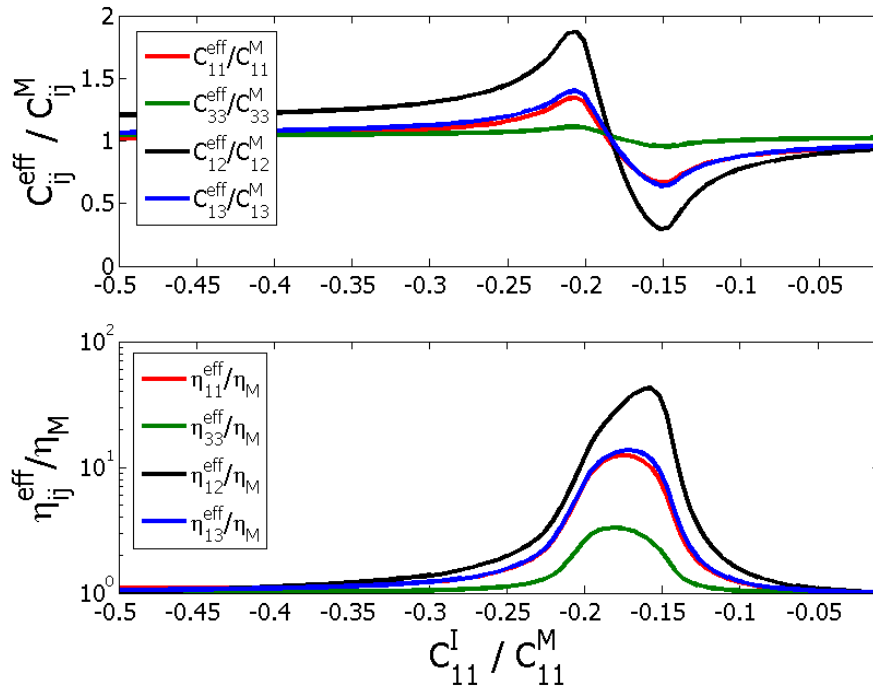


Figure 20: Effective stiffness and loss properties predicted by the Self-Consistent model for a composite containing identically oriented 2% by volume of the mesoscale inclusions modeled in Sections 4.1.5 and 4.1.6. The matrix is assumed to have  $\nu = 0.30$  and  $\eta = 0.05$ .

#### 4.1.8 Validation of the Mesoscale Effective Stiffness Approximation

The multi-scale modeling approach developed by this research is a two-step nonlinear homogenization method. It employs finite element models to simulate the force-displacement behavior of the structured inclusion for a series of boundary conditions. The FE model considers the nonlinear elastic response resulting from the geometric nonlinearity on the inclusion structure. The methodology then assumes that the nonlinear stress and strain behavior resulting from the inclusion structure can be well-represented as a continuous elastic solid inclusion with nonlinear mesoscopic effective elastic properties,  $\mathbf{C}_{meso}^{eff}(\mathbf{E}_{meso})$ , where  $\mathbf{C}$  is the effective nonlinear mesoscopic stiffness tensor and  $\mathbf{E}$  is the Green's strain tensor evaluated at the mesoscale. This is the micro- to meso scale transition model. The mesoscopic stiffness tensor is then used as a strain-dependent input to the meso-to-macro scale

transition model which is based on standard self-consistent micromechanical effective medium theory [7,8]. Using this approach, one is thus capable of direct evaluation of the influence of nonlinear microscale structural response on the macroscopic effective behavior of a composite containing a specified volume fraction of structured inclusions. To validate and benchmark this unique multiscale modeling approach, the following three different models were developed for determining the effective macroscopic properties,  $\mathbf{C}_{\text{macro}}^{\text{eff}}$ , of a composite consisting of a matrix containing with a known volume fraction of structured inclusions:

1. Micromechanical effective medium models of a matrix containing homogeneous linear elastic particulate inclusions
  - a. The three micromechanical models used were the Differential Effective Medium (DEM), the Self-Consistent (SC), and the Mori-Tanaka (MT) models.
2. FEA of representative volume element (RVE) consisting of a matrix containing a homogeneous cubic inclusion with known elastic properties
3. FEA of a RVE consisting of a matrix containing a structured inclusion

The figure below depicts the geometric representation of these 3 model sets.

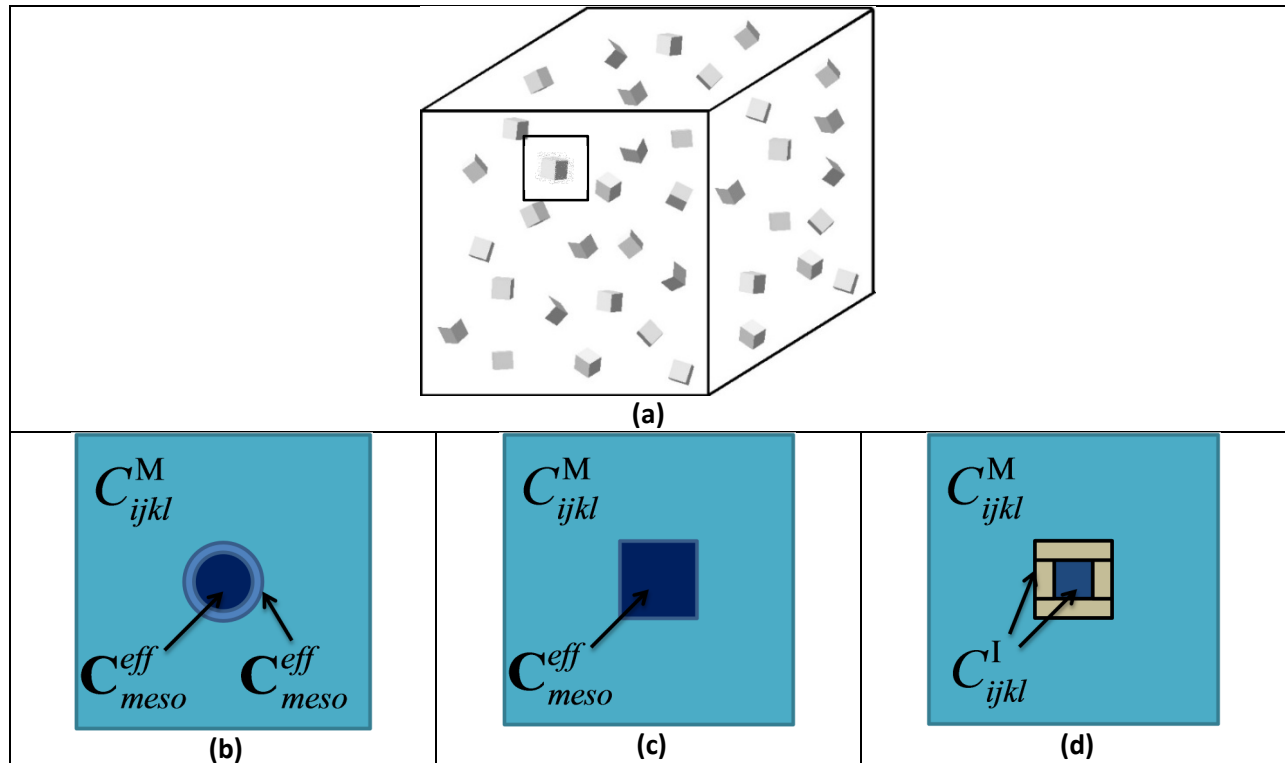


Figure 21: Three multiscale modeling validations of increasing complexity. (b) Depicts the composition and geometry used associated with analytical modeling called for in bullet 1, (c) shows the geometry and properties used in FEA effective medium models associated with bullet 2, and (d) depicts the geometry and properties employed doing a single-step multiscale FEA approximation model as discussed in bullet 2.

Micro- to mesoscale transition homogenization benchmarking was first done for linear inclusion behavior and was validated for the case of nonlinear inclusion behavior by extension. In order to determine  $\mathbf{C}_{\text{meso}}^{\text{eff}}(\mathbf{E}_{\text{meso}}) \rightarrow \mathbf{C}_{\text{meso}}^{\text{eff}}$  of the inclusion for input into model sets 1 and 2, a linear direct energy method was carried out on the structured inclusion to determine the small strain (linearized) stiffness tensor of the structured inclusion. The effective mesoscale stiffness results for the suite of applied displacements at the boundaries of the inclusion per the description provided in Table 1 are given in Table 2.

**Table 2: Strain energy and stiffness in a candidate structured inclusion using the direct FEA micro- to mesoscale transition model.**

	$C_{11}$	$C_{12}$	$C_{13}$	$C_{33}$	$C_{44}$	$C_{66}$
Strain Energy Function (J)	3.28E-10	6.68E-10	3.96E-06	3.96E-06	2.54E-07	3.49E-08
Stiffness (Pa)	1.87E+07	3.44E+05	4.28E+06	2.26E+11	3.62E+09	4.98E+08

The meso- to macroscale effective medium scale transition modeling was run for the case where the matrix material was considered to be isotropic constraining with Young's modulus,  $E = 1$  GPa and Poisson's ratio,  $\nu = 0.3$ . Several compositions were considered with volume fractions,  $\phi$ , of structured inclusions taking values of:  $\phi \in [0.1 \ 1, 2, 3, \dots 10]\%$ . The results from each of the models are shown in Figure 22–Figure 24.

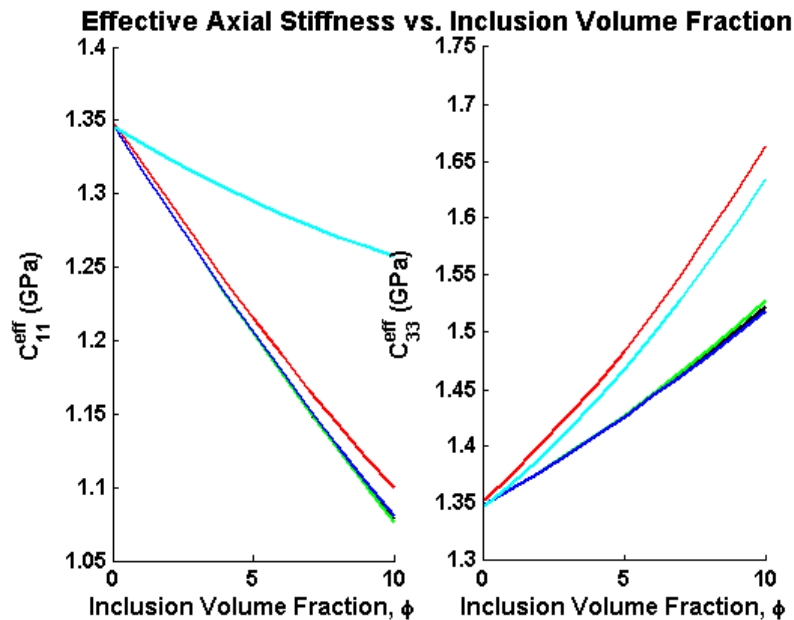


**Figure 22. Effective axial stiffnesses versus inclusion volume fraction. Black = differential effective medium; green = generalized self-consistent model; dark blue = Mori-Tanaka; red = FEA with  $\mathbf{C}^I = \mathbf{C}_{\text{meso}}^{\text{eff}}$ ; and light blue = FEA with structured inclusion with  $\mathbf{C}^I$ .**

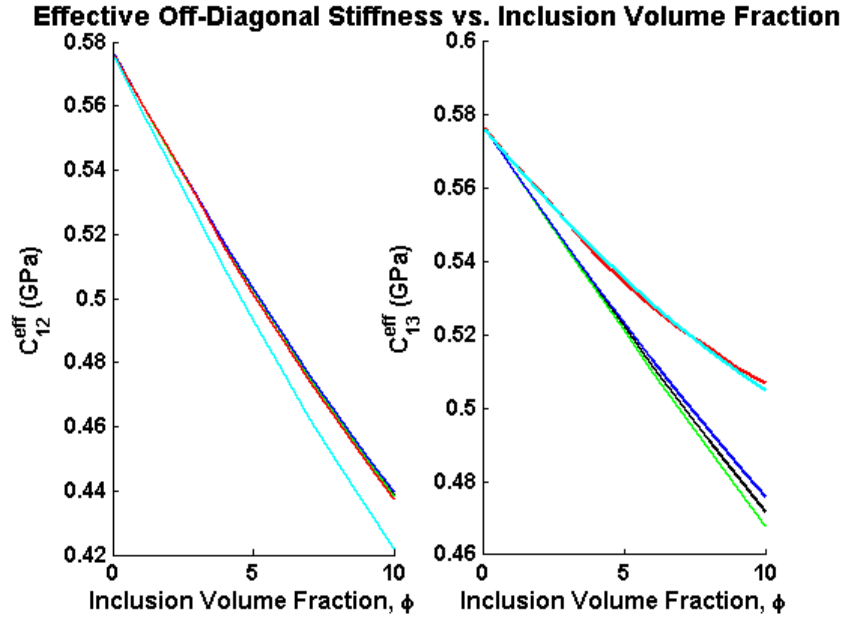


Figure 23. Effective off-diagonal stiffnesses versus inclusion volume fraction. Black = differential effective medium; green = generalized self-consistent model; dark blue = Mori-Tanaka; red = FEA with  $C^I = C_{meso}^{eff}$ ; and light blue = FEA with structured inclusion with  $C^I$ .

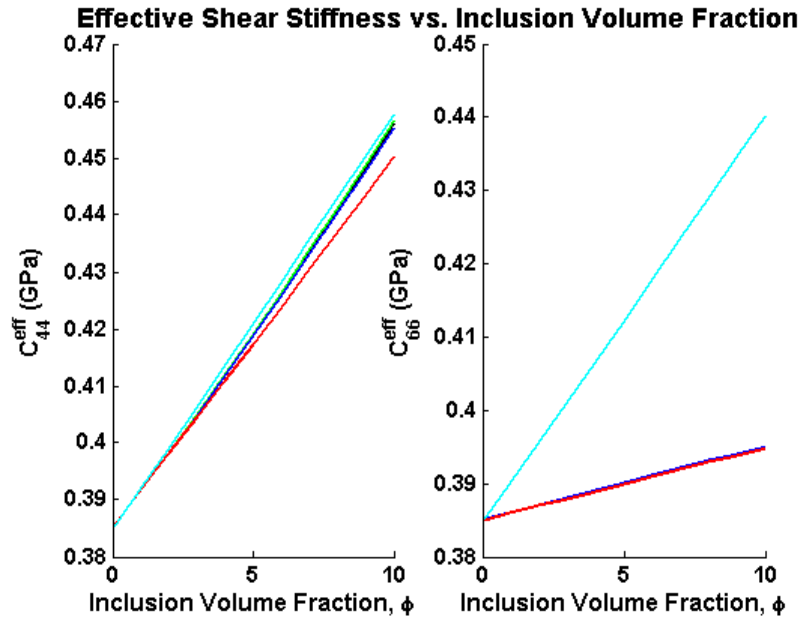


Figure 24. Effective shear stiffnesses versus inclusion volume fraction. Black = differential effective medium; green = generalized self-consistent model; dark blue = Mori-Tanaka; red = FEA with  $C^I = C_{meso}^{eff}$ ; and light blue = FEA with structured inclusion with  $C^I$ .

These results show that there is good agreement between the various modeling approaches for determining effective macroscopic stiffness properties. It is worth noting that the three analytical EMT models produce essentially the same values for all inclusion volume fractions and that both sets of FE model results closely follow these trends. At the extreme volume fraction of 10%, the FEA-structured

inclusion case differs from the EMT results by no more than 20%. For the purposes of this research, where volume fractions of interest are limited approximately 2%, the results of the EMT and FEA approaches are much more similar. We can therefore be certain that the micro- to mesoscale transition approach employed in this research captures the physics dominating the influence of microscale structure on the effective properties at the macroscale. Given the good agreement between stiffness values and general trending among all models, the assumption that the stress/strain state of a structured inclusion can be well-represented by a solid inclusion of bulk properties is thus considered validated and of utility for multiscale design purposes, while it is acknowledged that there exists levels of discrepancy that are higher than desired, specifically with respect to the effective shear moduli of the composite.

#### 4.1.9 Microstructural Design: Geometry Parameterization

In light of the ultimate aim of designing a microscale inclusion tuned for desired macroscale stiffness and loss characteristics, the inclusion geometry was parameterized to allow for a comprehensive study of the attainable stiffness values given the material and thermal loading constraints. The figure below illustrates the 2D inclusion geometry along with the geometric parameters of interest. The external boundaries of the inclusion, and the mesoscale, is defined by the parameter  $L$ . The parameter  $2H$  defines the height of T-shaped interface. The parameter  $T$  defines the width of the connection between the interface and the buckled element. The parameter  $L1$  is defined by the overall length  $L1 = L/2 - 2H$  and locates the midpoint of the inclusion. The parameter  $B$  defines the height of the buckled element and the voided region below it. Finally,  $L2$  defines the buckled element length.

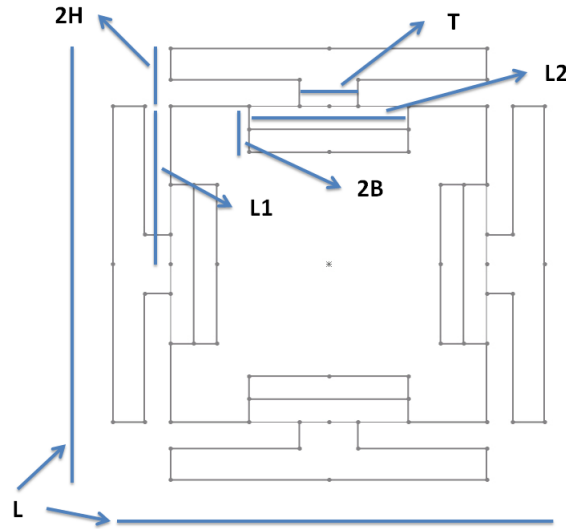


Figure 25. Cross-section view of parameterized inclusion geometry with all critical parameters labeled.

Having thus established the various geometric parameters, a wide range of inclusion geometries can be constructed by means of implementing a select number of parametric ratios. The ratios of interest are

$$R_{L1L2} = \frac{L2}{L1}, \quad R_B = \frac{2B}{L1 - L2}, \quad \text{and} \quad R_{L2T} = \frac{T}{L2}. \quad (17)$$



In the following section, these ratios are varied over a wide range of possible values to generate a highly populated design space consisting of a large set of possible geometries that may produce NS behavior.

#### 4.1.10 Microstructural Design: Geometry Dependent Stiffness

In order to provide a full inspection of the design space for this particular inclusion shape, a range of values for each geometric ratio was established and particular geometries were constructed using a Halton sequence. A Halton sequence is a deterministic sequencing approach based on a prime number base. The Halton sequence offers a means to produce quasi-random sampling of a wide design space, and allows one to easily add permutations to the dataset, provided that the ranges of parameters to be inspected remain constant. For this study, the number of geometric trials was set at 1000 within the specified ranges of values that the parameters can take. The ranges for each ratio specified for design space exploration are contained in Table 2. These ranges were chosen to provide a broad sampling range resulting in both negative and positive values of effective mesoscopic stiffness.

**Table 3: Range of possible values taken by the ratios defined in Eq. (17) for NS inclusion design space exploration.**

Ratio	Min	Max
$R_{L1L2}$	0.6	0.99
$R_B$	0.1	0.98
$R_{L2T}$	0.05	0.2

Below is a plot of each parameter value for any given trial. The data points illustrate the quasi-random nature of the Halton sequence and illustrate the degree of coverage of the design space for inspection.

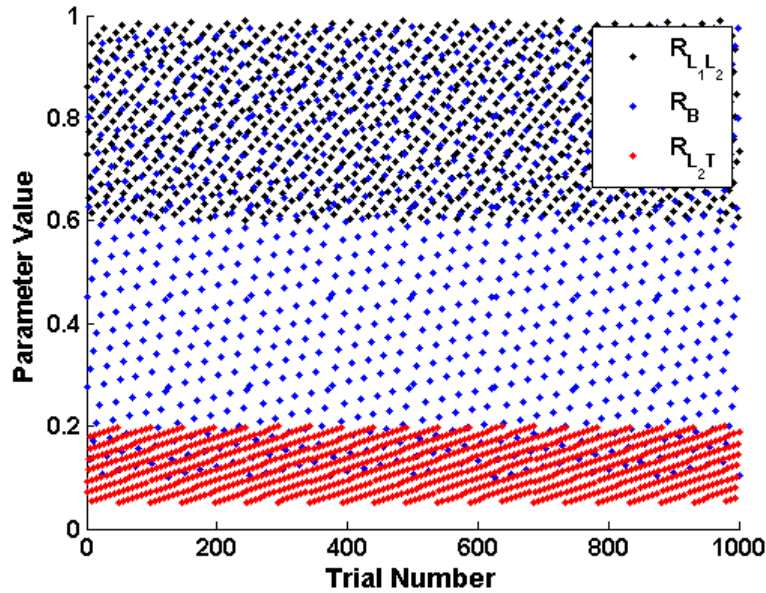


**Figure 26. Parameter value versus trial number for the ratios used to generate inclusion geometries.**

Using Comsol Livelink for MATLAB, two different Finite Element Analysis (FEA) studies were implemented. Each study contained an automated inclusion geometry construction and meshing routine. The first study analyzed the nonlinear 2D plane strain temperature dependent elasticity constants  $C_{11}$ ,  $C_{12}$ , and  $C_{66}$  over a range of imposed displacements. The second study analyzed the 3D elasticity constants,  $C_{11}$ ,  $C_{12}$ ,  $C_{13}$ ,  $C_{33}$ ,  $C_{44}$ , and  $C_{66}$ . Below are nine example geometric configurations with associated FEA meshes which illustrate the wide range of geometries simulated during this exhaustive design space inspection.

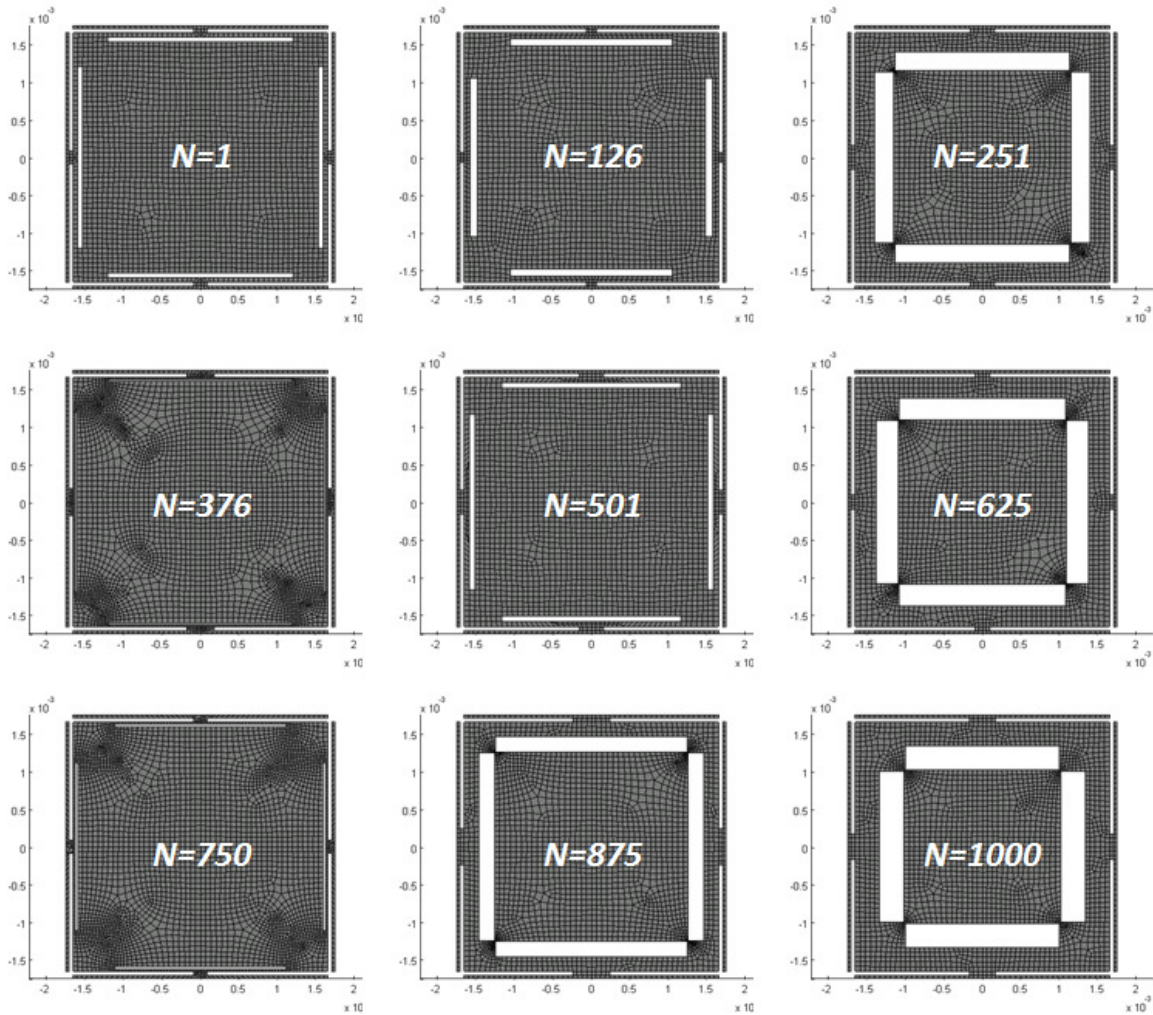


Figure 27. Example geometries generated using a Halton sequence from the 1000 trials run for design space exploration.

Below is a plot of the nonlinear plane strain stiffness values ( $C_{11}$ ,  $C_{12}$ , and  $C_{66}$ ) versus applied displacement for all 1000 geometric simulations.

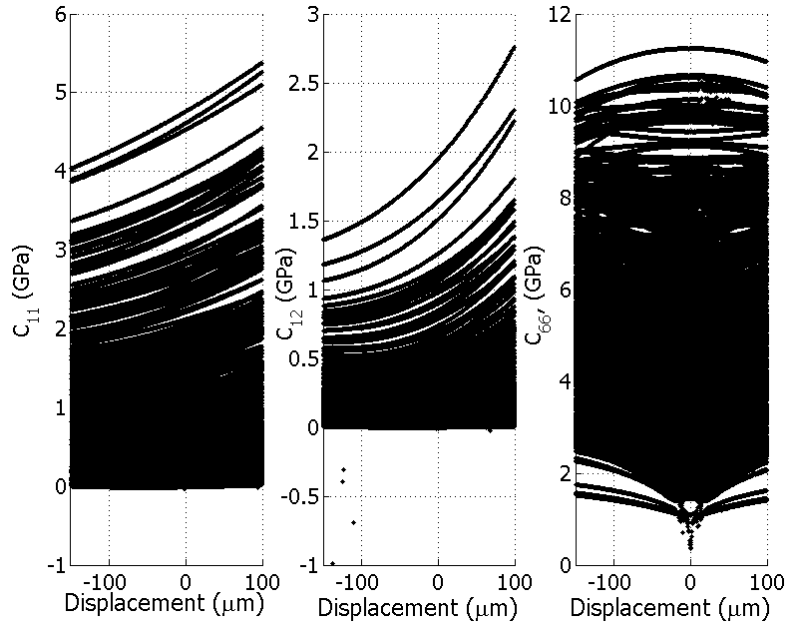


Figure 28. Stiffness versus displacement values for  $C_{11}$ ,  $C_{12}$ , and  $C_{66}$  for all 1000 trials.

A zoomed section of the displacement dependent mesoscopic  $C_{11}$  verifies that negative values for the  $C_{11}$  stiffness were obtained for a percentage of the designs generated during the design space exploration.

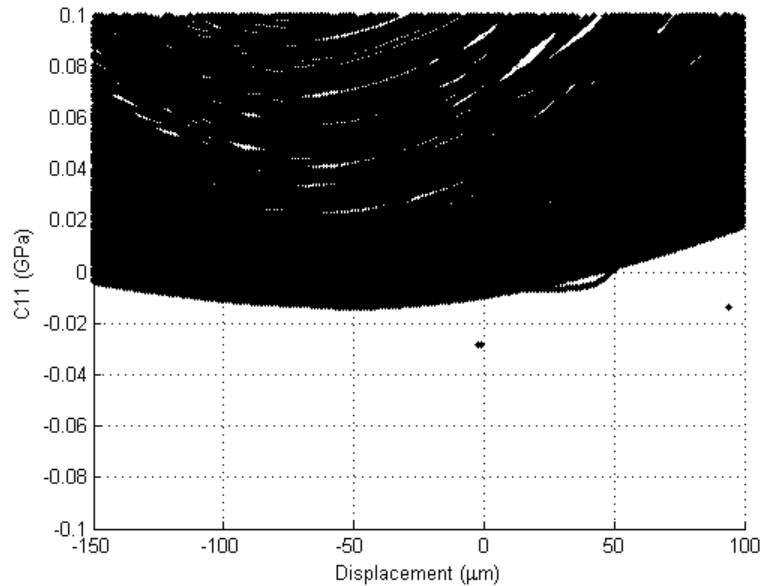


Figure 29. Zoomed view of  $C_{11}$  stiffness versus displacement values for each of the 1000 trials run during this research.

This data, along with values of the 3D elastic constants, which altogether amounted to over 500,000 data points, was used to build a surrogate model of the stiffness data as a function of the structured inclusion parameters. A surrogate model is an analytical function that is fitted to arbitrary data points, in this case points generated using computationally expensive FEA models, in order to save time and

computational expense. There are many approaches to generating surrogate models and the approach used in this project is known as “Kriging” [9a].

#### 4.1.11 Microstructural Design: Kriging Surrogate Modeling

Kriging surrogate modeling is a data fitting technique that was initially developed in the field of topology to interpolate the value of a random field at an unobserved location using observations of its value at nearby locations. It can be simply described as a known global function with additional departures from the base model, as described in Eq. (18)

$$y(x) = \sum_{j=1}^k \beta_j f_j(x) + Z(x). \quad (18)$$

In this expression,  $\beta_j$  are unknown coefficients of the base fitting function,  $f_j(x)$  are pre-defined functions, and  $Z(x)$  provides the departures from the base function in order to interpolate the training points [9b].  $Z(x)$  is the realization of a stochastic process with a mean of zero, variance of  $\sigma^2$ , and nonzero covariance of the form:

$$\text{cov}[Z(x_i), Z(x_j)] = \sigma^2 R(x_i, x_j), \quad (19)$$

where  $R$  is a user-specified correlation function. Similar to the approach employed by Backlund et al. [9b], this study employs a constant term for  $f(x)$  and a Gaussian curve in the form shown in (20) is employed as the correlation function:

$$R(x_i, x_j) = \exp\left[-\theta_i (x_i - x_j)^2\right]. \quad (20)$$

In Eq. (20)  $\theta_i$  are unknown correlation parameters that are automatically determined during the model fitting process.

While Kriging has been shown to be slow in terms of build and prediction time compared with other surrogate modeling techniques [9c], Kim et al. demonstrate the ability of Kriging to successfully model nonlinear and multimodal problems [9d]. For this reason, a Kriging approach was selected for generating a surrogate model of the nonlinear effective mesoscopic inclusion stiffness as a function of the geometric parameters of interest to this project.

In general terms, surrogate models were developed for this project using a Kriging approach in order to determine the effective nonlinear mesoscopic stiffness as a function of inclusion geometry, constituent material properties, and thermo-mechanical loading. This can be stated in a pseudo-mathematical representation as illustrated below:

$$\mathbf{C}_{\text{meso}}^{\text{eff}} = f(\text{geometry}, \text{materials}, \Delta T, \text{displacement}).$$

The advantage of this functional approach is that the effective mesoscopic stiffness can be calculated using an analytical function rather than a computationally expensive FE model. Clearly, this is a powerful tool. It permits the estimation of the mesoscale inclusion stiffness for any arbitrary geometry (within the provided bounds) in a matter of seconds as opposed to the hours required to generate results using computationally-intensive FEA methods. It is important to note, however that one must generate a large dataset using FEA results in order to produce the surrogate model. Further, the models are established in order to generate the training data points for subsequent surrogate models should inclusion materials or temperatures change. Thus, a very general approach to obtaining accurate estimates of inclusion stiffness based on arbitrary geometries has been established and leveraged in this work to generate significant computational capabilities for a highly nonlinear constitutive microscale geometry that can be exploited to produce negative stiffness behavior. This will greatly enhance the future design of multiscale materials that employ microscale structure to generate negative stiffness behavior.

#### **4.2 Negative Poisson Ratio Materials**

In recent years there has been an increased general interest in a group of materials, the properties of which have been described as auxetic [10]. An auxetic material is one in which the Poisson's ratio,  $\nu$ , is negative, i.e. an applied tensile strain in the longitudinal direction results in a positive strain in the transverse direction. It has been found that a number of naturally occurring materials are auxetic in behavior, for example, a range of crystalline structures including iron pyrites [11], [12] and some forms of skin [13] and cancellous bone structures [14], though it should be noted that Poisson's ratios for bone are usually reported as positive [15]. However, it is also possible to engineer auxetic behavior and this has been shown to be possible for a number of synthetic materials. These have included polyurethane and metallic foams [16-21], composite laminates [22] and a range of microporous polymers namely polytetrafluoroethylene (PTFE) [23], ultrahigh molecular weight polyethylene (UHMWPE) [24], nylon [25], polypropylene (PP) [26], and polyester [27].

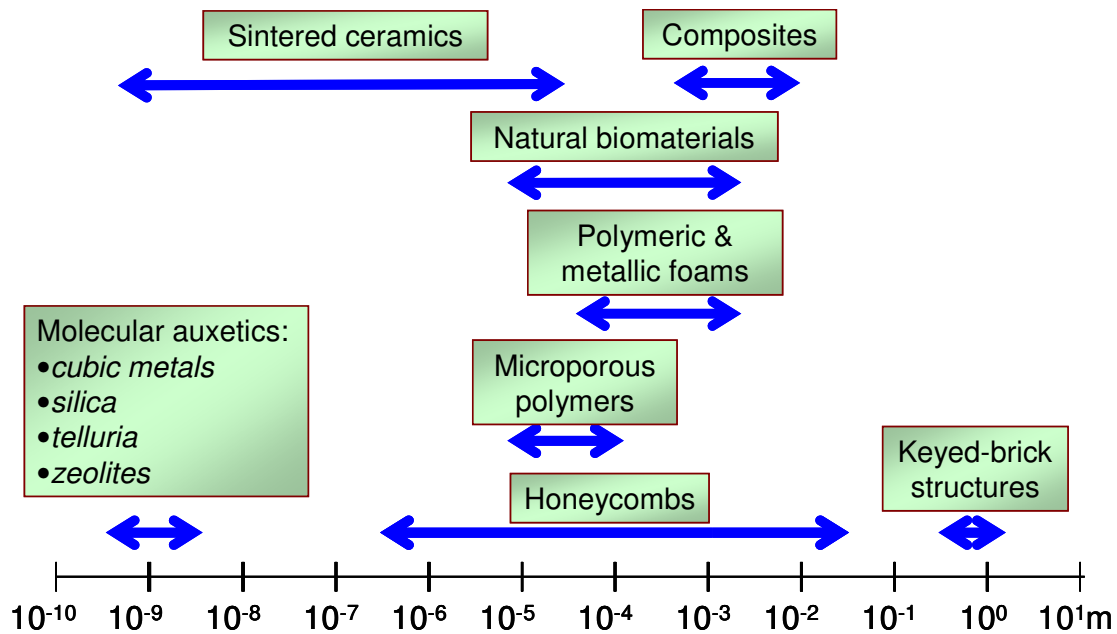
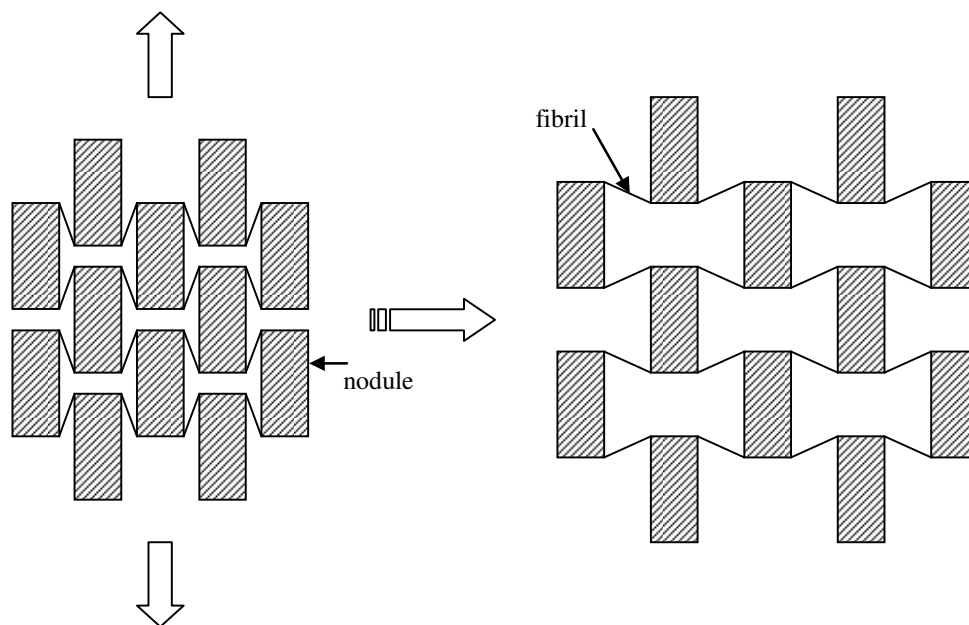


Figure 30: Auxetic materials and structures across the length scales.

Considering polymers, it was found that, for larger cross section cylinders, the auxetic effect is due to their complex microstructure [23-26]. This is essentially a network structure, which has been described as a system of nodules interconnected by fibrils and the mechanism for this effect is well defined [28], [29]. In essence, the re-entrant structure of auxetic foams had been reproduced by the nodule-fibril structure [26], the schematic structure for which is shown in Figure 31 and a similar deformation mechanism was noted. In this case, it is the fibrils which are hinging, though, rather than the cell ribs as is seen in the foams. This hinging of the fibrils in turn causes the nodes to translate, producing the auxetic effect. It was also noted that there was a variation in the number and size of the fibrils formed during the production of the cylinders for the various polymers, in particular, the degree of fibrillation for PP was much lower than that for PTFE or UHMWPE [26].



**Figure 31: Two dimensional schematic diagram of nodule-fibril model for auxetic behavior in polymeric cylinders**

#### *4.2.1 Processing routes to produce auxetic extruded fibers and films*

In 2001, a novel processing route was developed to produce auxetic polypropylene fibers based on the powder processing route used to produce auxetic PP cylinders [30],[31]. The same powder and processing temperature were employed, *i.e.* Coathylene PB0580 and at a temperature of 159°C. The powder processing technique was adapted to take place within an Emerson and Renwick Ltd Labline melt extruder. The extruder has 5 temperature zones, each with individual thermostatic control, a 3:1 compression ratio, a 25.4mm (1 inch) diameter screw and a length/diameter ratio of 24:1. A schematic of the extruder is shown in Figure 32. Powder is fed into the hopper and is transported through the extruder by the screw. In conventional melt extrusion, the polymer is fully molten. In this case, however, processing occurs at a much lower temperature with the aim being to partially melt the powder only. To produce fibers, the extruder is fitted with a spinneret plate. The first fibers were produced using a 40 hole spinneret plate with hole diameters of approximately 0.55mm [30],[31]. The fibers produced were characterized by measuring their Poisson's ratio using Biax 200C micro-tensile testing equipment, which was fitted with a 10 Newton load cell and specialized Messphysik videoextensometry software, shown schematically in Figure 33.

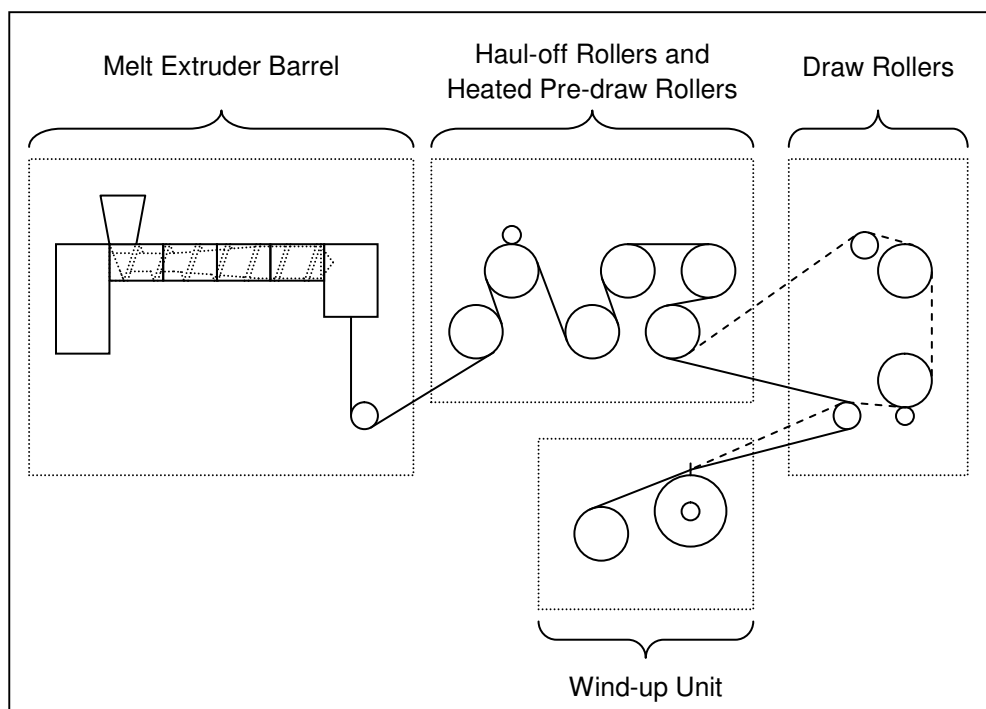


Figure 32: Schematic of extruder used to produce auxetic fibers.

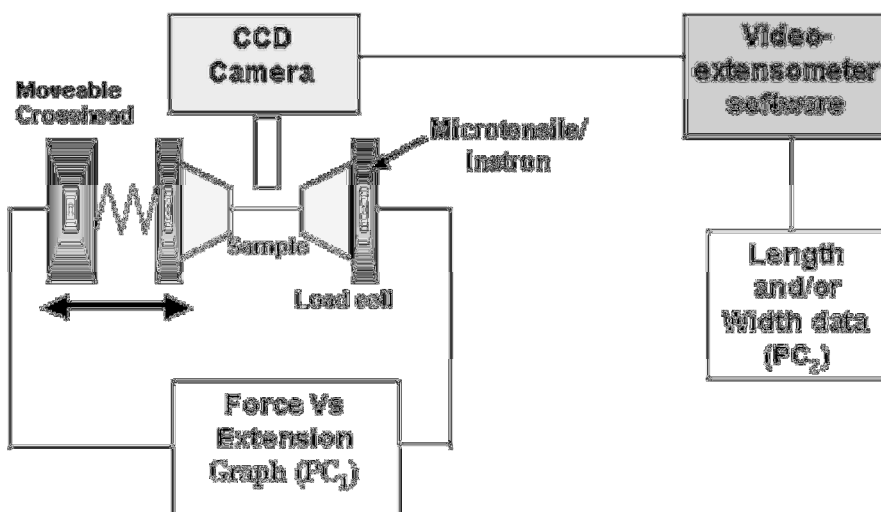


Figure 33: Schematic of the videoextensometry measurement system used to characterize auxetic fibers.

The Messphysik software simultaneously measures length and width data from changes in contrast between attached markers (along the length) and the edges (across the width) of the fibers. This allowed the optimum conditions to be defined as a processing temperature of 159°C, screw speed of  $1.047\text{rads}^{-1}$  (equivalent to 10 RPM and resulting in a throughput of 6g/mm) and a take-off speed of 2m/min. No drawing other than that caused by gravity as the fiber exited the spinneret was employed.



Using these conditions, 40% of the fibers tested displayed auxetic character. These fibers were found to be inhomogeneous along their length with, on average, 20 – 30% of their lengths consisting of auxetic material *i.e.* their auxeticity is 20 – 30%. The Poisson's ratio of the auxetic region was found to be, on average,  $\nu = -1.62$  and the overall Poisson's ratio of the entire fiber length was also negative, being  $\nu = -0.7$  [32]. The auxetic fibers produced are undrawn, and, as such, as well as being inhomogeneous, they have low mechanical properties, with a modulus of 1.3 GPa, strain to yield of 7.5% and tensile strength of 25MPa

For the fibers, auxetic behavior is based on a closely packed particulate or granular microstructure with a low void content, which is a close approximation to the actual microstructure, see Figure 34.

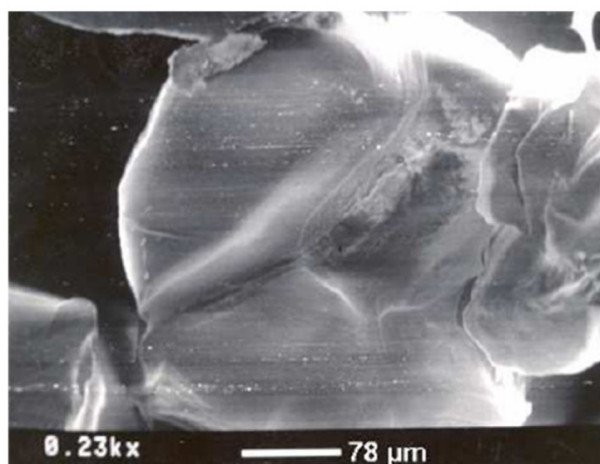


Figure 34: Microstructure of an auxetic polypropylene fiber.

The nodule-fibril model used to study auxetic behavior in cylinders is clearly not appropriate here. In this case, mechanisms for auxetic behavior are based on a rough particle model described by interlocking rigid hexagons as shown in Figure 35 [33], [34]. The interlocked structure is formed by rectangular radial 'keys' and geometrically matched 'keyways' and is derived from the geometry employed in the Tokai nuclear reactor designed in the 1950's [35], [36]. These structures consist of free-standing columns of graphite bricks laterally connected by loose side and/or corner keys in keyways. The key-keyway combinations produce, effectively, a rough macroparticle assembly in which interactions are characterized by having tangential stiffness exceeding normal contact stiffness. The keyed-brick structures expand in all radial directions when subjected to a tensile load in the horizontal plane by translation of the bricks through sliding of the bricks and radial keys along the keyways [34]. To study the auxetic fibers, the interlocking hexagon geometry has been selected for simplicity.

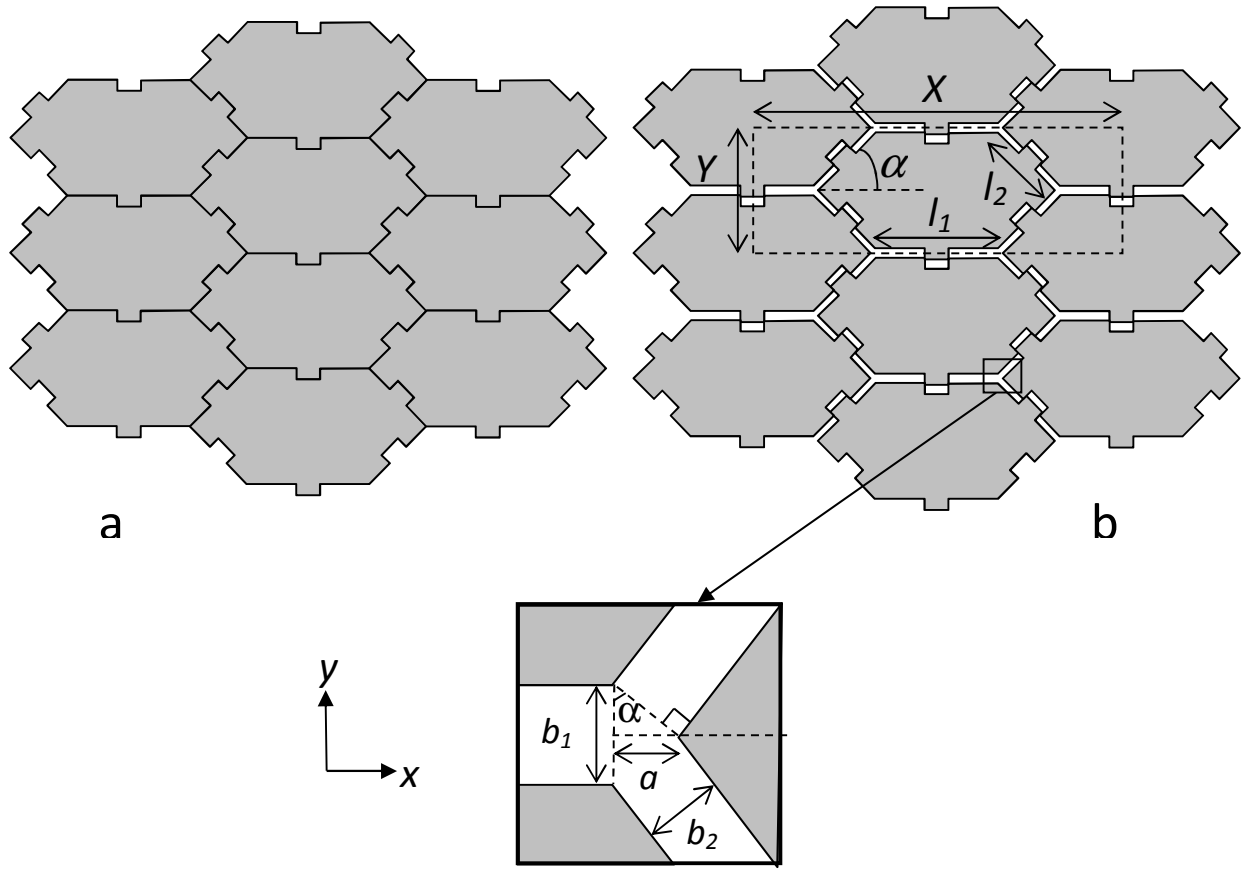


Figure 35: Schematic of the interlocking hexagon model. In (a), the material is fully densified; in (b), the material is partially expanded.

Looking at Figure 35, the hexagons have edge lengths  $l_1$  and  $l_2$ . The edges of  $l_1$  are aligned parallel to the x-axis and the edges of  $l_2$  are at an angle  $\alpha$  to the x-axis. Thus, the unit cell lengths are given by

$$X = 2(l_1 + l_2 \cos \alpha + a), \quad (21)$$

and

$$Y = 2(l_2 \sin \alpha + a \cot \alpha), \quad (22)$$

where  $a$  is the parameter defined in Figure 35 as the gap between adjacent hexagon particles.

For deformation of the structure by the mechanism of particle translation,  $a$  is the variable parameter. So, the changes in unit cell lengths are thus

$$\frac{dX}{da} = 2 \quad \text{and} \quad \frac{dY}{da} = 2 \cot \alpha, \quad (23)$$

and the Poisson's ratio in the x-direction is given by

$$\nu_{xy} = -\frac{d\varepsilon_y}{d\varepsilon_x} = -\frac{dY/Y}{dX/X} = \left(\frac{dY}{da}\right)\left(\frac{dX}{da}\right)^{-1}\left(\frac{X}{Y}\right). \quad (24)$$

Combining Eqs. (21)-(24) one finds  $\nu_{xy}$  to be

$$\nu_{xy} = -\frac{\cos \alpha (l_1 + l_2 \cos \alpha + a)}{l_2 \sin^2 \alpha + a \cos \alpha}, \quad (25)$$

and similarly  $\nu_{yx}$  is

$$\nu_{yx} = -\frac{l_2 \sin^2 \alpha + a \cos \alpha}{\cos \alpha (l_1 + l_2 \cos \alpha + a)}. \quad (26)$$

The expressions for Young's moduli of this network were derived by using the conservation of energy approach [34]. In the x-direction,  $E_x$  is given by

$$E_x = k_h \left( \frac{2 \cos^2 \alpha + 1}{\sin \alpha} \right) \left( \frac{l_1 + l_2 \cos \alpha + a}{l_2 \sin^2 \alpha + a \cos \alpha} \right), \quad (27)$$

where  $k_h$  is the stiffness of a spring assumed to connect each male-female interlock combination. Similarly, the Young's modulus in the y-direction is

$$E_y = k_h \left( \frac{2 \cos^2 \alpha + 1}{\sin \alpha \cos^2 \alpha} \right) \left( \frac{l_2 \sin^2 \alpha + a \cos \alpha}{l_1 + l_2 \cos \alpha + a} \right). \quad (28)$$

Predictions show that interlocking hexagons having  $0 < \alpha < 90^\circ$  lead to auxetic behavior for the assembly. The models show good agreement with experimental values at low strains [33], [34].

A further experimental variation on the extrusion process was introduced by changing the spinneret plate employed to produce fibers to a slit orifice of dimensions 63.5 x 14.2 x 0.38mm. Using this, films were produced from polypropylene, initially based on the process window that was used successfully to produce PP fibers [27], [33]. The PP films produced at 159°C with screw speed 1.05 rads<sup>-1</sup> and 0.0225 ms<sup>-1</sup> take off speed were found to have  $\nu_{xy} = -1.12$  and  $\nu_{yx} = -0.77$  at low strain, typically up to 1%. The Young's moduli in this case were  $E_x = 0.34$  GPa and  $E_y = 0.20$  GPa. Beyond 1%, the film undergoes an auxetic-to-nonauxetic transition [27]. A detailed processing parameter study was undertaken to assess the effect of the change in cross-section of the die-head from circular for the fibers to rectangular for the films [37]. There were several interesting findings. For the first time, a 100%

auxetic extruded product was produced for several processing parameter sets. For example, 100% auxeticity was measured for films extruded at 159<sup>0</sup>C, screw speed 1.05 rads<sup>-1</sup> and take up speed 0.0225 ms<sup>-1</sup> and for those extruded at 159<sup>0</sup>C, screw speed 1.05 rads<sup>-1</sup> and take up speed 0.15 ms<sup>-1</sup>.

#### *4.2.2 Information on NPR materials selected and why they are of interest*

The inclusions selected for this project are  $\alpha$ -cristobalite and samples produced from auxetic extruded products comprising polypropylene (PP) fibers or films. The  $\alpha$ -cristobalite was selected as it has a high modulus,  $E = 65.4$  GPa, combined with a small negative Poisson's ratio of  $\nu = -0.16$ . Conversely, the modulus of the auxetic fibers and films is much lower at  $E = 1.3$  GPa for the fibers and  $E = 0.34$  GPa for the films, but the Poisson's ratio in both cases is higher. On average for both systems the Poisson's ratio, which is strain dependent, is  $\nu = -0.6$ . The fibers can have a Poisson's ratio as low as  $\nu = -1.6$  with auxeticity of 20 – 30%. The films, while of a lower modulus, can be produced to have  $\nu = -0.95$  and be 100% auxetic. Thus, the inclusions selected for this project are available or can be readily manufactured, and comprise a high modulus, low negative Poisson's ratio inclusion or a low modulus, high negative Poisson's ratio inclusion.

#### *4.2.3 Fabrication of $\alpha$ -cristobalite samples*

Samples have been manufactured to the specification of 0, 5, 10, 15, 20 and 25wt%  $\alpha$ -cristobalite, which is a naturally occurring high modulus auxetic mineral. The resin used was a room temperature curing epoxy system (Epon E828/D400) together with a viscosity modifier (silicone polycarbonate urethane, CarbiSil®) in trace amounts. The inclusions were added to the resin, vigorous mixing was undertaken for 1 hour and then the homogeneous slurry was cast in aluminum moulds and cured at room temperature.

#### *4.2.4 Microscopy*

Optical microscopy was not successful in revealing the microstructure of the samples due to their opacity, as can be seen in Figure 36 and Figure 37 which optical micrographs of the 0wt% and 25wt% samples, respectively.

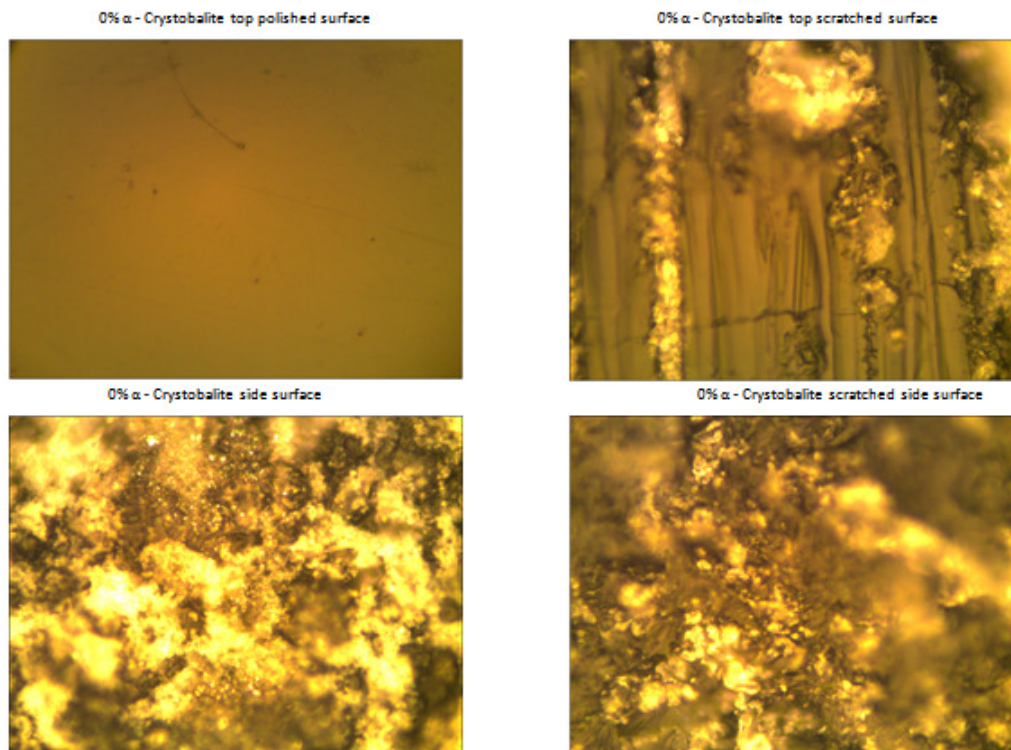


Figure 36: Optical micrograph of a 0%  $\alpha$ -cristobalite sample.

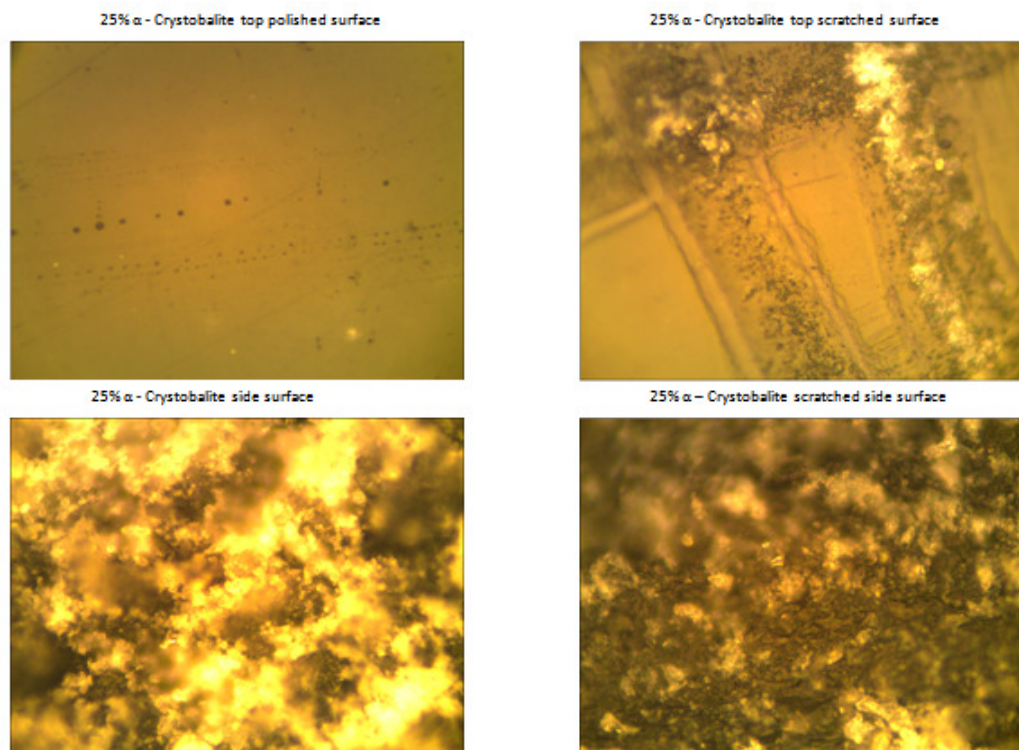


Figure 37: Optical micrograph of a 25%  $\alpha$ -cristobalite sample.

It was therefore decided that scanning electron microscopy be carried out in place of optical microscopy and that this should be in conjunction with elemental mapping to begin a study of the distribution and interfacial bonding of the  $\alpha$ -cristobalite particles. The findings of the elemental mapping are given in Table 4 and Table 5.

**Table 4: Weight % of carbon, oxygen and silicon in the  $\alpha$ -cristobalite inclusion samples**

% $\alpha$ -cristobalite	Weight % of		
	C	O	Si
0	75.18	23.69	-
5	74.21	24.35	1.05
10	71.85	26.55	1.61
15	70.405	26.605	3.09
20	70.69	25.54	3.77
25	68.21	26.62	5.03

**Table 5: Atomic % of carbon, oxygen and silicon in the  $\alpha$ -cristobalite inclusion samples.**

% $\alpha$ -cristobalite	Atomic % of		
	C	O	Si
0	80.74	19.10	-
5	79.60	19.93	0.48
10	77.71	21.55	0.74
15	76.84	21.72	1.45
20	77.28	20.97	1.76
25	75.46	22.11	2.38

Table 6 and Table 7 show that while the distribution is not homogeneous throughout, the particles do not float to the top of the samples or sink to the bottom, creating intensely rich  $\alpha$ -cristobalite inclusion regions. The data presented in these tables indicate that SEM micrographs allow for a clearer picture of the internal structure of the samples.

**Table 6: Weight % of carbon, oxygen and silicon in the top, bottom and middle of the 25%  $\alpha$ -cristobalite inclusion samples**

Surface examined	Weight % of		
	C	O	Si
Top	71.72	26.93	1.27
Middle	68.21	26.62	5.03
Bottom	71.31	26.89	1.80

**Table 7: Atomic % of carbon, oxygen and silicon in the top, bottom and middle of the 25%  $\alpha$ -cristobalite inclusion samples**

Surface examined	Atomic % of		
	C	O	Si
Top	77.52	21.89	0.59
Middle	75.46	22.11	2.38
Bottom	77.29	21.88	0.84

To illustrate the structures seen during SEM imaging of the samples constructed for this project, two micrographs are presented below. The first, Figure 38, shows the side view of a resin only sample.

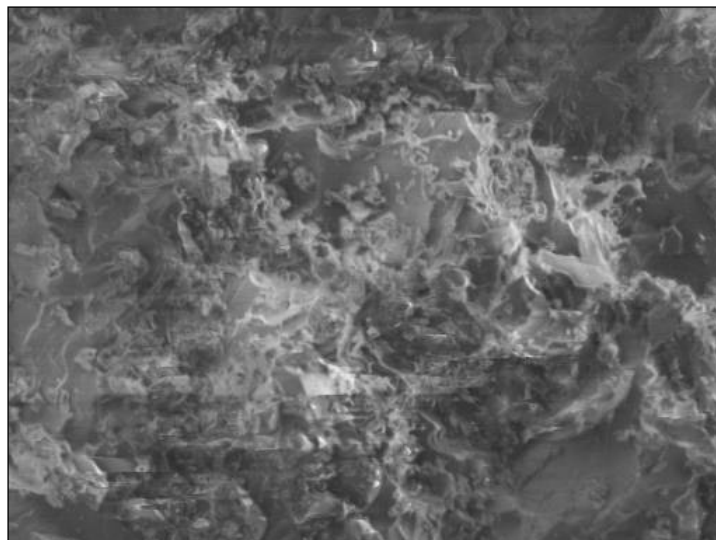


**Figure 38: SEM image of a pure resin sample for reference with composite consisting of resin and  $\alpha$ -cristobalite inclusions shown in Figure 39.**

The second image shows the side view of a 25wt% composite. The red circles indicate the locations of  $\alpha$ -cristobalite inclusions, confirmed by the elemental mapping. The resulting changes in material properties for various samples are discussed in Section 4.2.5.

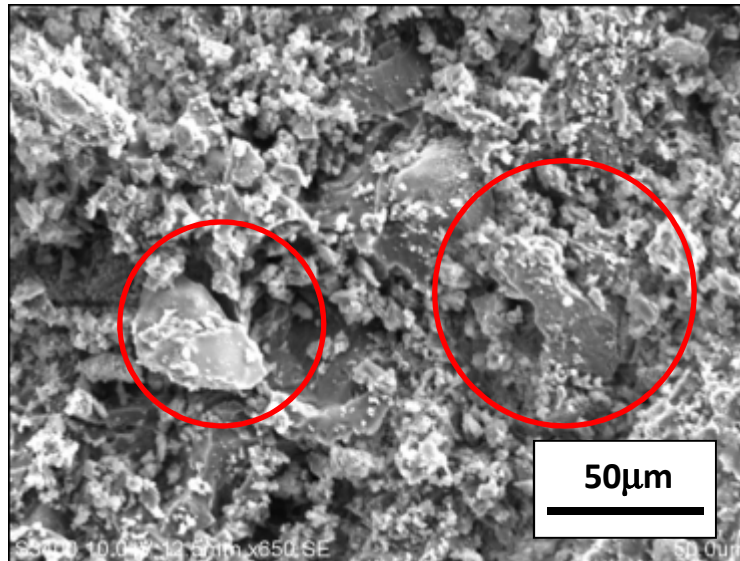


Figure 39: SEM image of a composite consisting of resin and 25wt%  $\alpha$ -cristobalite inclusions. Red circles indicate inclusions.

#### 4.2.5 Quasistatic Mechanical Testing of $\alpha$ -cristobalite Inclusion Composites

An average of 6 samples were tested for each of the composites manufactured with 0, 5, 10, 15, 20 and 25wt%  $\alpha$ -cristobalite, each specimen being 150mm long by 15mm wide by 5mm thick. Tensile tests were carried out to measure the mechanical properties of the composites using an Instron 3369, in conjunction with videoextensometry using a Messphysik ME 46 videoextensometer. A crosshead speed of 0.3mm/min was used with a gauge length of 100mm and a load cell of 100N. The Poisson's ratio measurement was obtained using a rectangular box of 30 by 10mm marked on the samples for the videoextensometer to track. The strain-strain plots for the control sample (*i.e.* with no  $\alpha$ -cristobalite) and for the 25%  $\alpha$ -cristobalite sample are shown below in Figure 40. In both cases, the Poisson's ratio is positive but it can be seen that the addition of the 25wt%  $\alpha$ -cristobalite reduces the Poisson's ratio value. In the cases shown, this reduction is from  $\nu = +0.33$  to  $\nu = +0.20$  for the  $\alpha$ -cristobalite inclusion sample. A complete set of the results from these tests is given in Table 8.

The observed reduction in Poisson's ratio is in agreement with the trend shown by theoretical predictions carried out using the self-consistent (SC) analytical model and FEA, both of which are shown in Figure 41 together with the experimental data. The system used here has  $E_f/E_m = 24$ . The effect of using  $E_f/E_m = 40$  is also shown in the same graph given that it is of interest since it should cause the Poisson's ratio to be further reduced. Agreement is very good at low volume fraction of  $\alpha$ -cristobalite.

Similar plots were obtained for the Young's modulus, and these can be seen in Figure 42. Here, the experimental data are compared to FE analysis and analytical values calculated using the SC and Hashin-Shtrikman (HS) upper and lower bounds. For ease of comparison, the modulus value plotted is that of the composite relative to the matrix. The addition of  $\alpha$ -cristobalite leads to a rise in the Young's modulus of the composite, with the HS lower bound predictions agreeing very well with the experimental values.



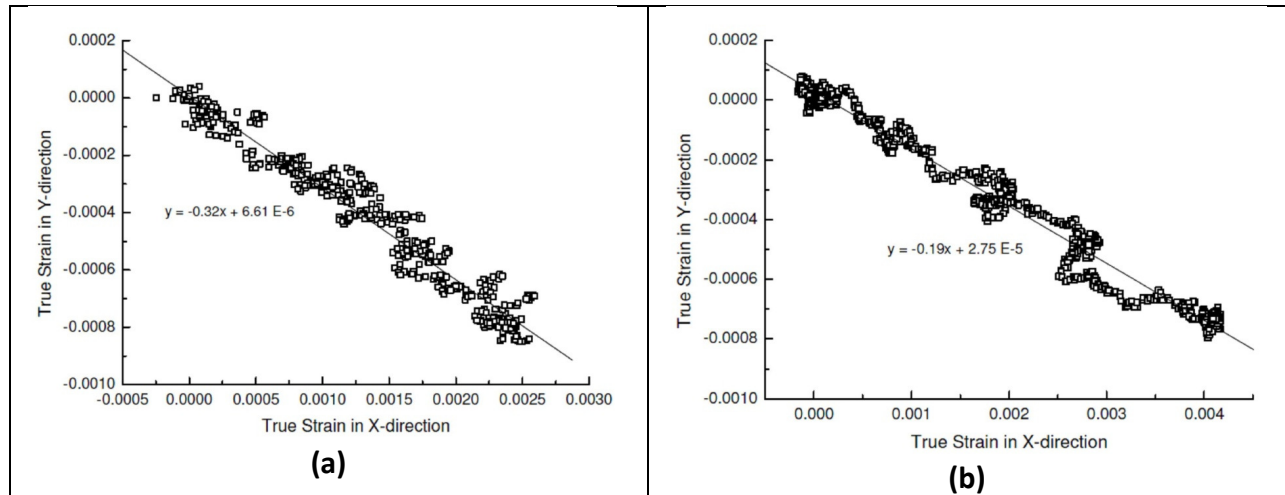


Figure 40: True strain-strain plot for the (a) control and (b) 25wt% composites.

Table 8: Experimental Poisson's ratio values for the  $\alpha$ -cristobalite composites.

Sample	Specimen number						Average Poisson's ratio
	1	2	3	4	5	6	
Resin	0.44	0.33	0.24	0.30	0.20	0.32	0.32±0.09
Resin + 5%	0.33	0.16	0.18	0.18	0.33	0.26	0.24±0.08
Resin + 10%	0.22	0.18	0.19	0.24	0.28	0.28	0.23±0.04
Resin + 15%	0.20	0.17	0.17	0.23	0.25	0.30	0.22±0.05
Resin + 20%	0.11	0.24	0.26	0.18	0.21	0.21	0.20±0.05
Resin + 25%	0.10	0.18	0.17	0.19	0.28	0.27	0.20±0.07

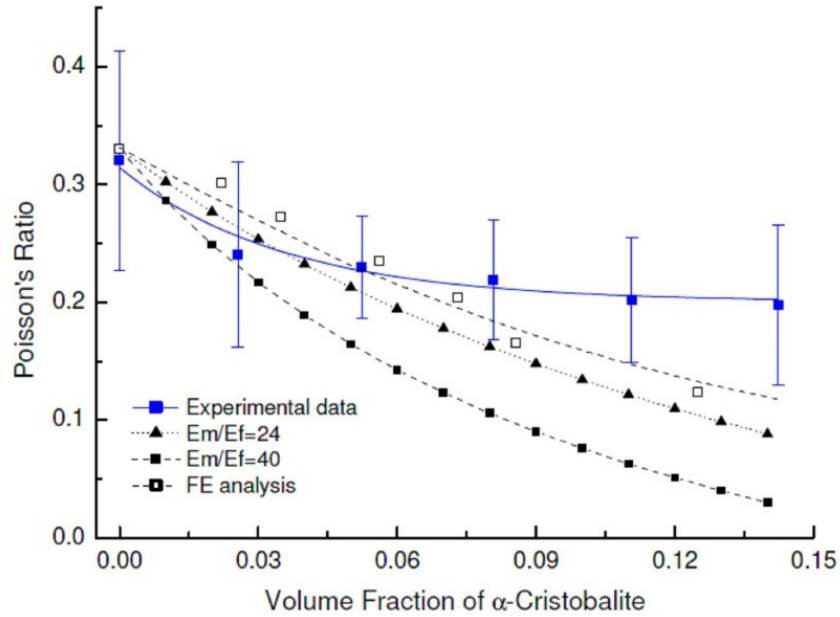


Figure 41: Plot of Poisson's ratio against volume fraction of  $\alpha$ -cristobalite inclusions for  $E_f/E_m = 24$  and 40.

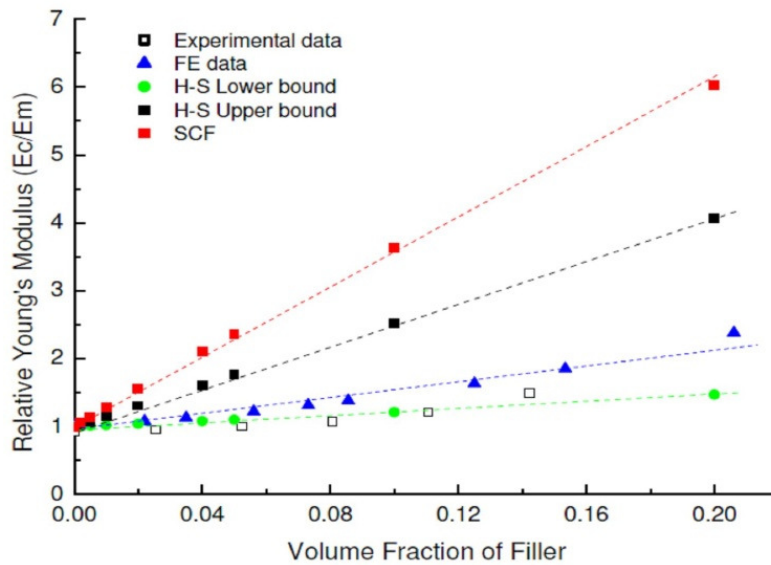


Figure 42: Plot of relative Young's modulus against volume fraction of  $\alpha$ -cristobalite inclusions

A number of reasons for the disagreement between the modeling and experimental results have been considered. The first of these is that the models are idealized. The second is that we think that despite the use of the viscosity modifier, the particle distribution of the cristobalite is not perfect, leading to some particle to particle contact, especially as the % volume of the cristobalite increases. The models are based on complete distribution with no particle to particle contact, which would tend to reduce the properties. The interface on inspection in the SEM appears to be a further possible source of difference between the model and experimental values. The project was stopped prior to detailed

examination of these hypothetical problems, but results clearly suggest that the samples are imperfect, which is not unexpected. An idealized bond between particle and matrix is an assumption of the models used for comparison, so the interface should be a focus of future work on these types of composite materials in order to gain maximum properties. A final reason for the observed difference could be that the samples have reduced volume fractions than those reported. The samples were made externally to our recipe but the initial elemental analysis appears to indicate that there may be less Si present than was desired. Eliminating the sources of all of these minor discrepancies should be the focus of future work in the area of auxetic composite materials.

#### 4.2.6 *Energy absorptive capacity of the composites*

There are many references which support the increased energy absorptive capacity of auxetic materials in, for example, foams [38],[39] and carbon fiber laminates [22]. More specifically for this project, investigations into the properties of auxetic UHMWPE cylinders were carried out and they revealed benefits in deploying auxetic polymeric materials. An interesting study was performed to measure the dynamic modulus of the auxetic UHMWPE using ultrasound [40] which resulted in measurement of the attenuation coefficient,  $\alpha$ , for auxetic, conventional compression molded plaques and compacted and single sintered UHMWPE. The microporous polymers, whether auxetic or sintered (which resulted in a positive Poisson's ratio), showed very large enhancements in the attenuation coefficient,  $\alpha$ . The authors report purely on experimental values, however, that the auxetic form was so good at absorbing the ultrasonic signal that in the highly fibrillar form, it was not possible to obtain a single measurement of  $\alpha$  as the signal was completely absorbed after 1 single back reflection.

The second of the directly related properties which has been studied in detail was the indentation resistance,  $H$ . This is related to the Poisson's ratio as

$$H \propto (1 - \nu^2)^{-x}, \quad (29)$$

with  $x$  dependent on the method of analysis considered. For example,  $x = 2/3$  for Hertzian indentation. Ball indentation tests were carried out on auxetic UHMWPE using conventional compression molded plaques and compacted, single sintered UHMWPE as comparison material. It was found that indentation resistance was enhanced by up to a factor of 3 at low loads, where the strain dependent negative Poisson's ratio has its highest values. The mechanisms at play in the indentation response were then examined [41]. Alderson, Fitzgerald and Evans propose that the fibrils pull the nodules under the indenter, leading to local and elastic densification under the indenter. This is underlined by the observation that the indents in the auxetic UHMWPE recover whereas the other conventional forms show permanent plastic deformation. The recovery is suggested to be due to the fibrils unwrapping on removal of the indenter, allowing the nodules to return to, or close to, their original position. Though these previous studies showed increases in energy absorption when auxetic materials were tested, it is unclear whether particulate composite materials consisting of a conventional matrix material containing auxetic inclusions will also display increases in energy absorption capacity. The materials that introduced in Section 4.2.3 and tested quasistatically in Section 4.2.5 were further characterized using dynamic

mechanical analysis, modal damping, and ultrasonic methods. The results of those measurements are given in the following section.

#### *4.2.7 Characterization of Particulate Composites Containing $\alpha$ -cristobalite*

The auxetic inclusion composites fabricated by the University of Bolton were characterized across a broad range of frequencies to capture their dynamic stiffness and loss performance. This was accomplished through Dynamic Mechanical Analysis (DMA), modal damping, and ultrasonic characterization techniques. These tests were run by researchers at all three of the associated universities. The University of Bolton characterized the samples using DMA, the University of Bristol measured the dynamic response using forced vibration techniques, and the University of Texas at Austin measured the response using contact ultrasonic techniques. The results of these measurements are provided in the following subsections.

##### 3.2.7.1 Dynamic mechanical analysis

Mechanical properties of materials can be expressed via dynamics modulus represented with the a storage and loss modulus of the material [42]. One conventional means for measuring these quantities is through Dynamic mechanical analysis technique. Dynamic Mechanical Analysis is a well-established, robust technique, which is frequently used to characterize the viscoelastic behavior of the polymers and polymeric composite materials [43]. When a material is tested using the DMA technique, an oscillatory (sinusoidal) strain (or stress) is applied to the material and the resulting stress (or strain) developed in the material along with its relative phase to the imposed loading is measured to yield a complex modulus. The complex modulus is thus the frequency-dependent material resistance to the deformation. It has two components, the storage modulus, which is a parameter describing the elastic energy stored during a single cycle of loading, and the loss modulus, which is a parameter of the energy dissipated through conversion to heat in a single loading cycle. The Dynamic Mechanical Analyzer produces very important information on all changes in the state of molecular motion as temperature or frequency is scanned and can be used to characterize material over a very broad range of temperatures and frequencies.

DMA test was performed at the University of Bolton using dual cantilever clamp on Isothermal frequency sweep mode for the series of  $\alpha$ -cristobalite samples. Because the stiffness of the samples is moderate, dual cantilever clamp was used for the experiment. The sample sizes, were 60mm x 15mm x 5mm, were determined based on the defined standards to insure accurate measurements. The isothermal frequency sweep test was performed at 35°C under 15 $\mu$ m amplitude which limited deformation to the linear regime. The storage modulus and  $\tan \delta$  (ratio of the loss to storage modulus) was recorded in the frequency range of 1 -100Hz. These tests were repeated to check the reproducibility of the results. The average values were taken for both the runs and recorded against the frequency and are presented in Figure 43 and Figure 44.

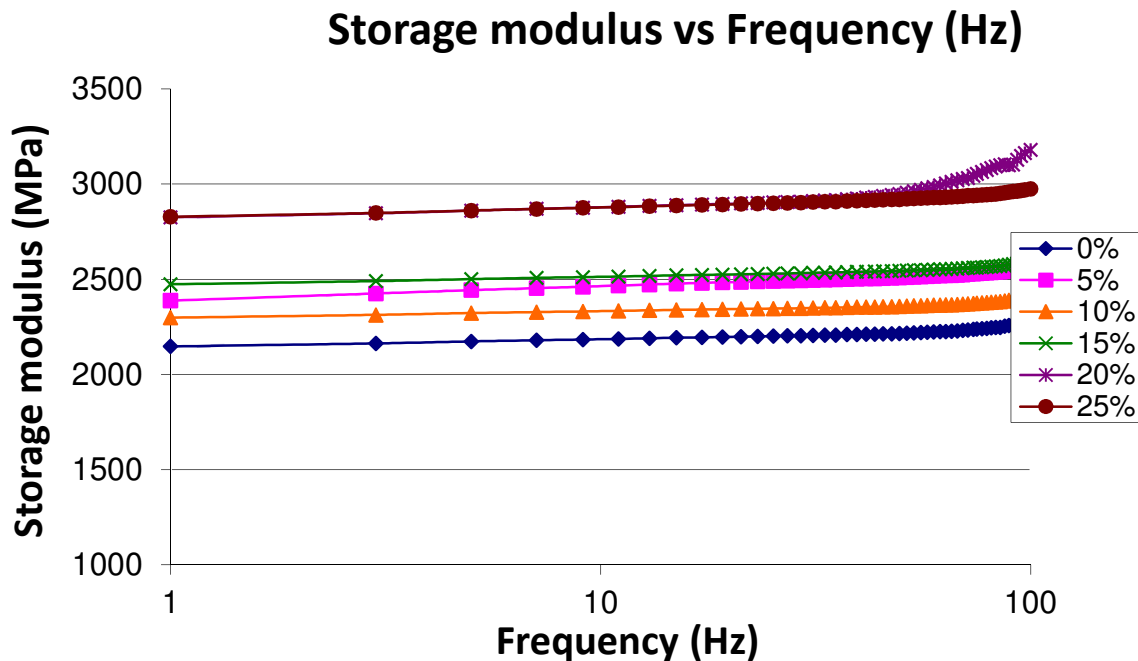


Figure 43: Storage modulus of auxetic inclusion composites tested using dual cantilever DMA.

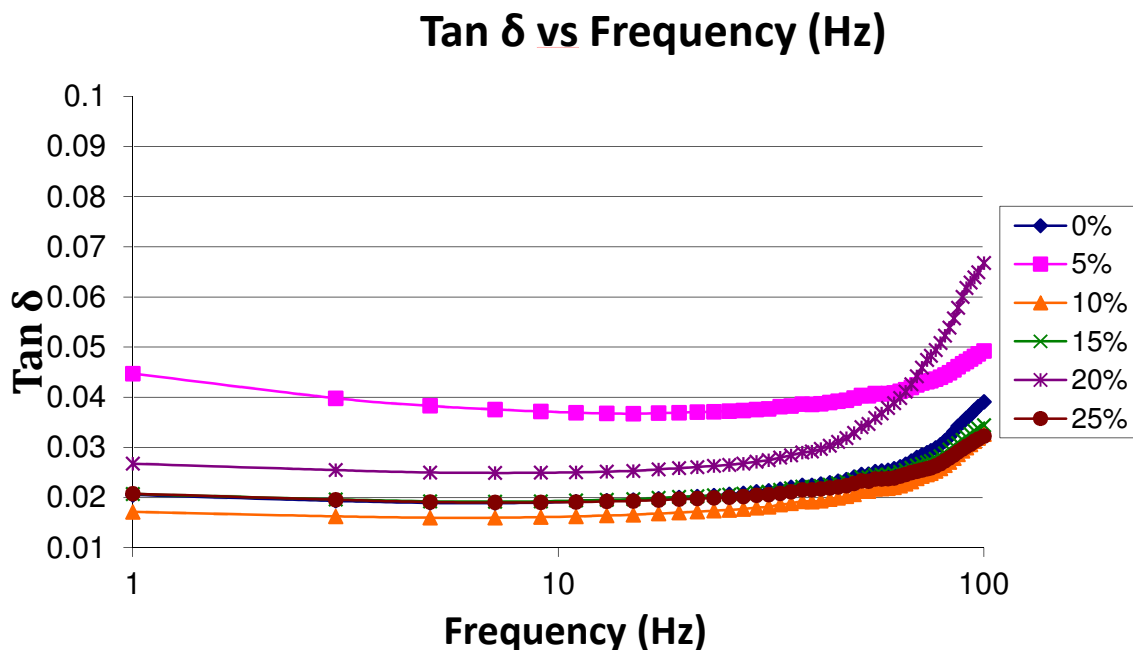


Figure 44: Tan  $\delta$  of auxetic inclusion samples acquired using dual cantilever DMA measurements.

These results shown in Figure 43 and Figure 44 shows a generally increasing stiffness with increase  $\alpha$ -cristobalite content but they do not provide a clear picture of the influence of increasing weight fraction on the loss behavior. Specifically, Figure 44 shows that the largest tan  $\delta$  values were observed for a 5% wt composite, while the lowest values were observed for the 10% wt composite. As with the quasi-static

tests, it is suspected poor bonding, non-uniform distribution of inclusions, or both may have contributed to this observed behavior. Due to the limited time of this project, however, a conclusive physical basis for the observed inconsistent loss behavior was not able to be identified.

### 3.2.6.2 Modal damping analysis

After DMA testing, modal analysis tests were performed at the University of Bristol using a custom-made rig employing electrodynamic excitation and scanning laser vibrometry (SLV). The tests were carried out of aluminium beams with a deposition of an epoxy/ $\alpha$ -cristobalite composite material patches attached to the beam center, as shown in Figure 45a. Typical sample dimensions are illustrated in Figure 45a and the test setup is indicated in Figure 45b and c.

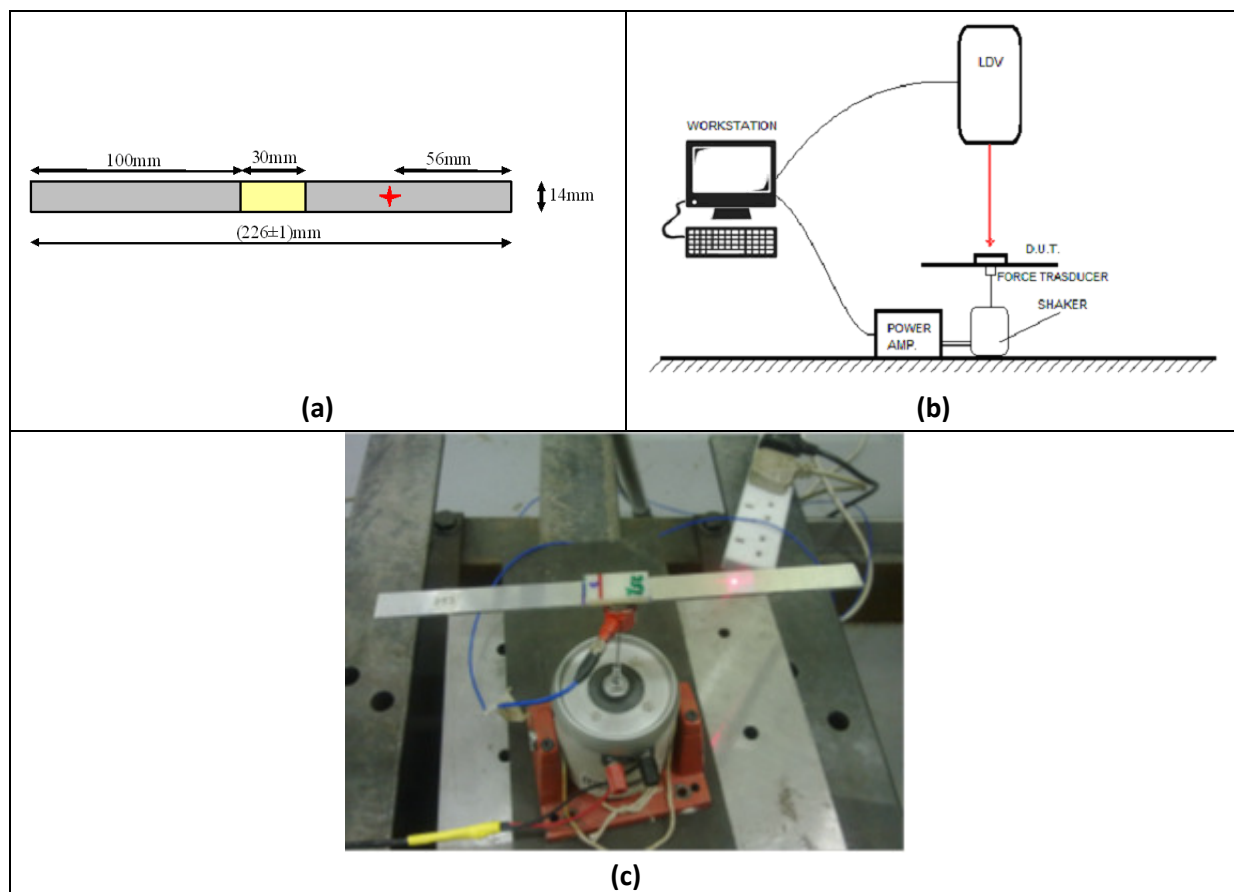


**Figure 45: Details of the force vibration measurements of modal damping. (a) shows the dimensions of the samples (both the aluminum and composite patch), (b) shows the a schematic of the test setup, and (c) provides a photo of the experimental setup.**

The beams were initially subjected to random white noise to identify the spacing of the natural frequencies, with subsequent pseudo-random sweep between 950 Hz and 1050 Hz, (corresponding to the 3<sup>rd</sup> flexural mode of the beam). The pseudo-random sweep was driven at a maximum amplitude of 1 V for sweep times of 2 seconds. The input force was measured with a PCB force transducer (calibration factor 42.24N/V, with range of 200 mV). Simultaneously, a SLV (Polytec PSV-400 F, velocity factor

25mm/s/V with channel range of 10V) was used both as single and multi-point velocity acquisition device. The frequency response functions (FRFs) were acquired through complex averaging, with a central frequency of 1.02 kHz and 0.1 kHz of bandwidth and 201 spectral lines.

The modal damping ratio was estimated using a half-power bandwidth technique implemented in Modent 2008 software. To maximize the signal-to-noise ratio, the technique was applied to the maximum amplitude point of the FRF. For each wt% of the epoxy/amorphous silica coatings, five samples were tested to acquire a sufficient statistical reproducibility of the results. Two input voltages (1 V and 5 V) were considered to identify any nonlinearity in the response. The mode chosen as reference was the third flexural mode because it resulted in the highest nodal strain for the free-free configuration considered.

An initial test carried out on a reference uncoated aluminium beam has provided the following values for the undamped natural flexural frequencies: 150 Hz, 500 Hz, 1000 Hz. Figure 46 shows the operational mode shapes as detected by the SLV.

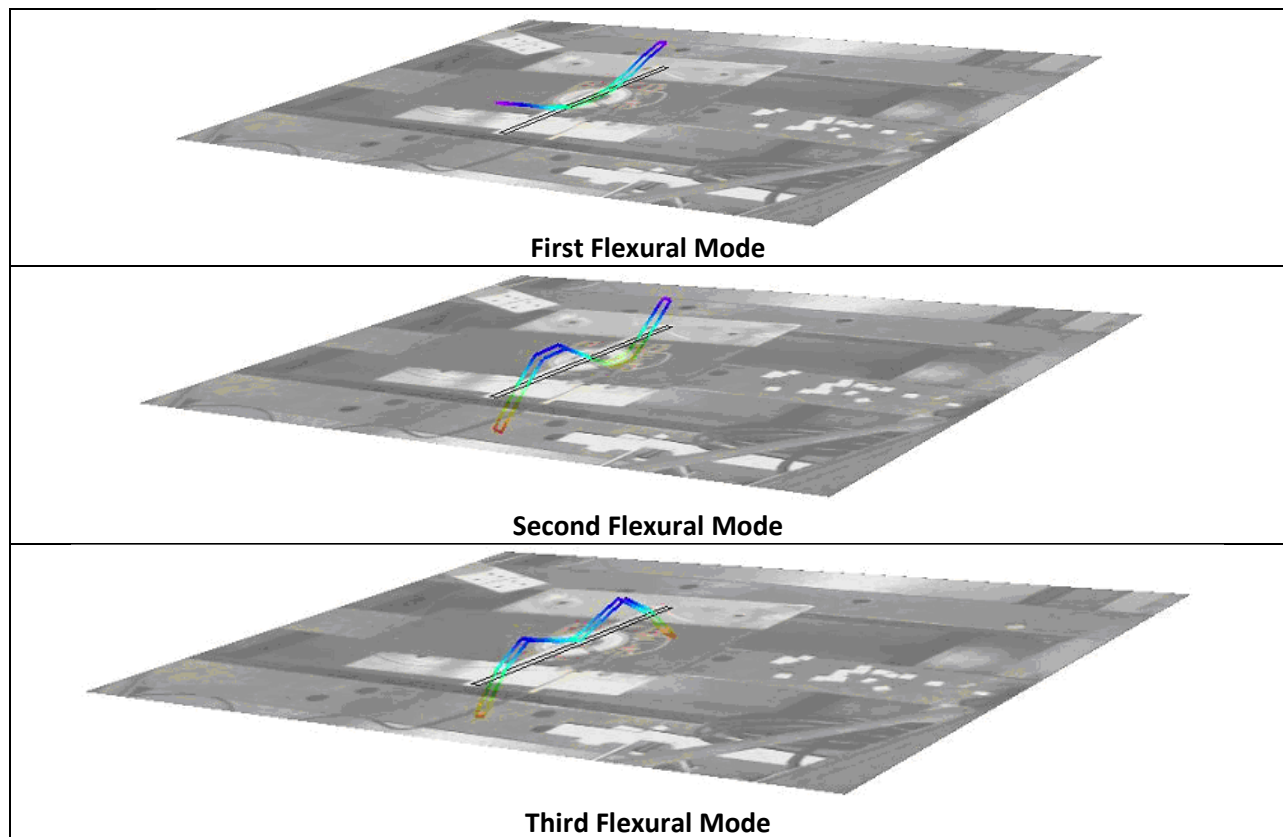
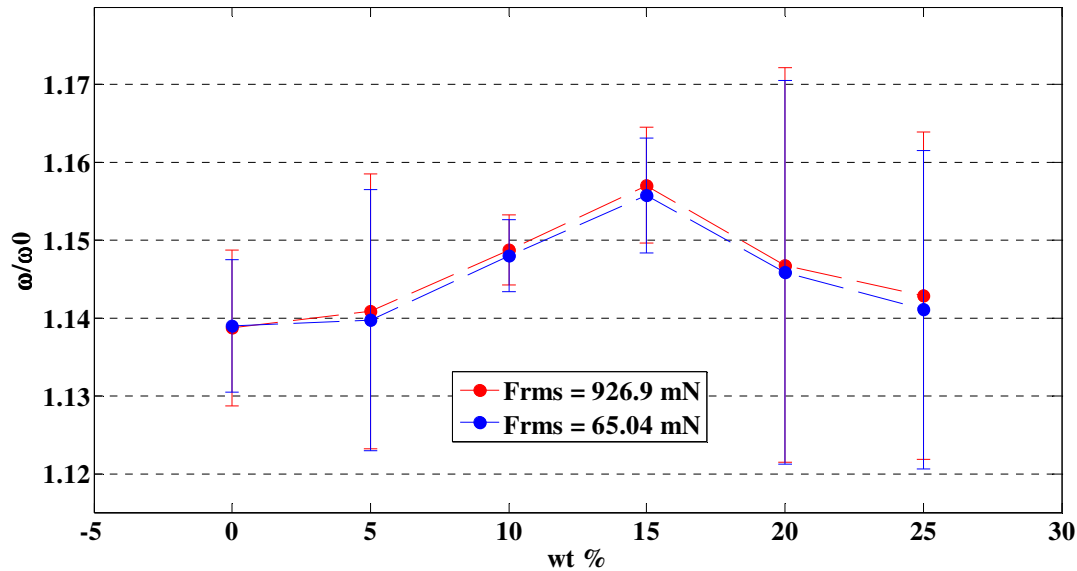


Figure 46: SLV Images of the first, second, and third flexural modes of the aluminum beams with auxetic inclusion patches.

The resulting impact on the patch on the stiffness of the beam-patch composite is summarized in Figure 47 which shows the variation of the third natural frequency normalized against the analogous one belonging to the uncoated beam sample.



**Figure 47: Variation in the resonant frequency of third mode of vibration for two different driving amplitudes as a function of the weight fraction of auxetic inclusion patches.**

These experimental results show that there is no apparent dependence of the natural frequency behavior against the value of the input force. The results suggest that the assumptions of linearity of the system (at least in terms of natural frequencies) are satisfied. However, it is worth noticing the large standard deviations existing for the 5 wt%, 20 wt% and 25 wt% samples. It is apparent that a more than a 15% increase in natural frequency occurs for the 15 wt% samples. The assumption of linearity is weaker, however, for the identification of the modal damping ratio, as it can be observed in Figure 7. An average 20 % increase of the modal damping ratio is observed passing  $F_{rms} = 65$  mN to  $F_{rms} = 923$  mN. Due to the amplitude of the standard deviations associated to the measurements, it is difficult to identify a clear trend existing between modal damping ratios and amount of amorphous silica reinforcement. However, it does appear that a clear increase in loss factor exists for the samples with the highest wt% considered and the highest amplitude of the root mean square force.



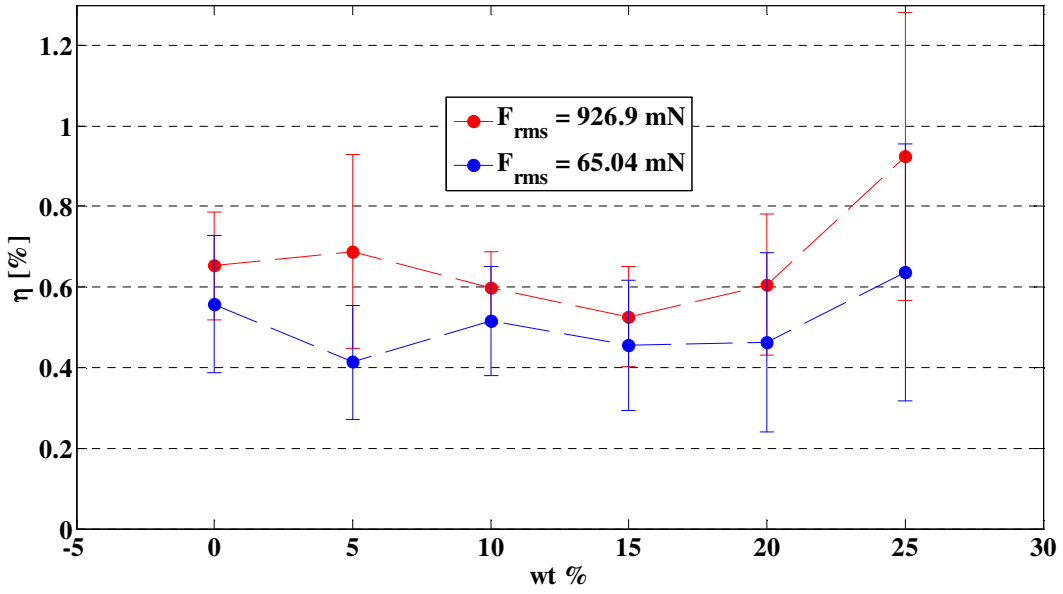


Figure 48: Variation in the modal loss factor (in percent) of third mode of vibration for two different driving amplitudes as a function of the weight fraction of auxetic inclusion patches.

### 3.2.7.3 Ultrasonic characterization

The final set of characterization testing done to understand the behavior of the auxetic composite materials was ultrasonic measurement of the effective stiffness and loss in a frequency band around 1 MHz. The test was accomplished using a contact ultrasonic method first described by Trieber and co-workers [44]. The test consists of six separate measurements which combine reflected wave and transmitted wave acquisition to simultaneously measure the phase speed and attenuation. These separate measurements permit direct measurement of the reflection coefficient between the transducer and the material sample which, unmeasured, would negatively influence the accurate estimate of the attenuation coefficient in the material. The parameters directly measured during the tests are the phase speed,  $c_{ph}$ , and attenuation coefficient,  $\alpha$ . For plane wave propagation, these parameters are related to the wave disturbance as shown in Eq. (30),

$$u(z, t) = u_0 e^{j(\omega t - kz)} = u_0 e^{-\alpha z} e^{j(\omega t - k'z)}. \quad (30)$$

In this formulation, the wavenumber is complex and defined with real and imaginary parts given by  $k = k' - j\alpha$ . The attenuation coefficient is a metric of the rate at which a forward progressing plane wave amplitude decreases in space due to inherent losses in the medium. The real part of the wave number,  $k'$ , is related to the phase speed,  $c_{ph}$ , through the relationship  $k' \equiv \omega/c_{ph}$ . Using the waveforms captured during the six measurements shown in Figure 49 it is possible to get estimates of the stiffness and loss properties of each sample, examples of which are shown in Figure 52 and Figure

53. During ultrasonic testing, six samples of each weight fraction (0, 5, 10, 15, 20, and 25%) were measured to get statistical information on the properties of the composites.

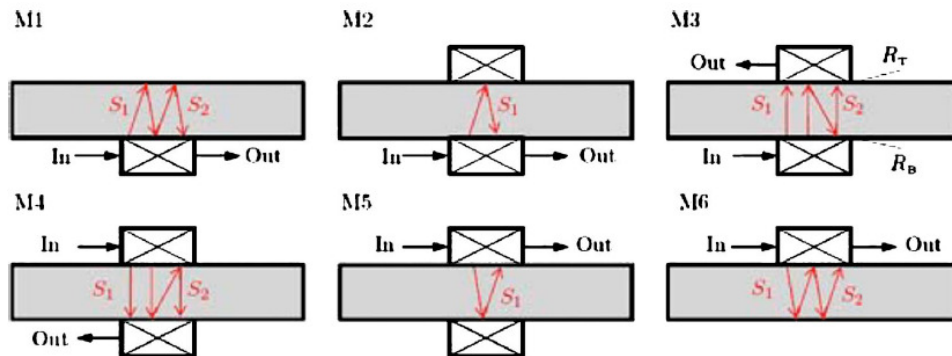


Figure 49: The six separate measurements associated with the ultrasonic characterization method used to characterize the auxetic inclusion samples. Measurements M1, M2, M5, and M6 use reflected signals, while measurements M3 and M4 use through transmission signals. Combinations of those signals permit direct calculation of the complex valued frequency dependent reflection coefficients at each interface.

The tests schematized in Figure 49 were realized by creating a test fixture like the one schematized in Figure 50. This fixture permits simple and repeatable attachment of the contact transducers while minimally influencing the position of the sample under test.

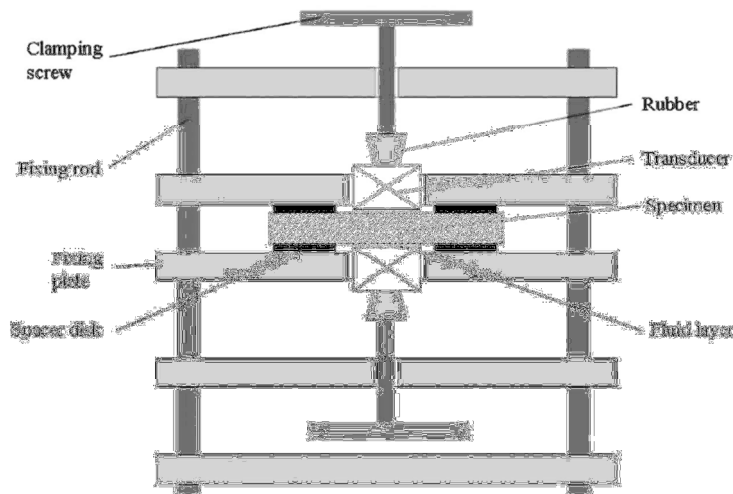
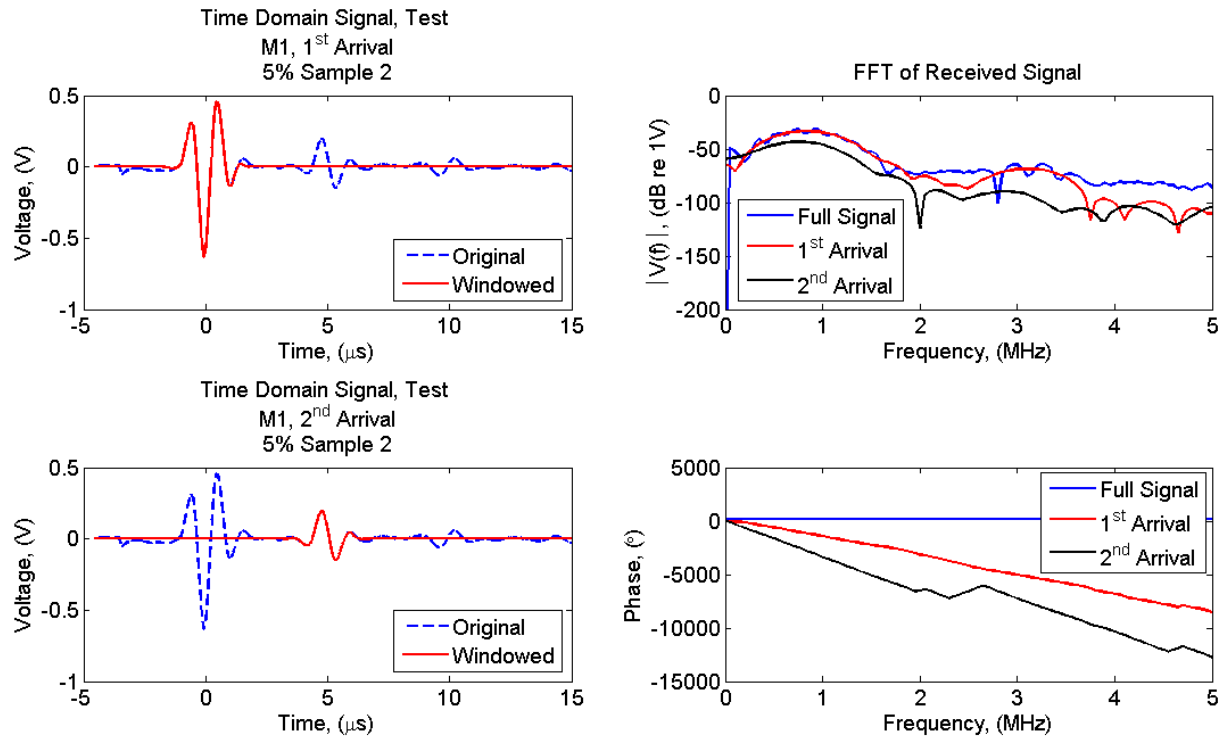


Figure 50: Schematic of the fixture created and used to complete ultrasonic attenuation measurements. The 'fluid layer' is the ultrasonic compliant used to improve the coupling between the transducer and auxetic composite.

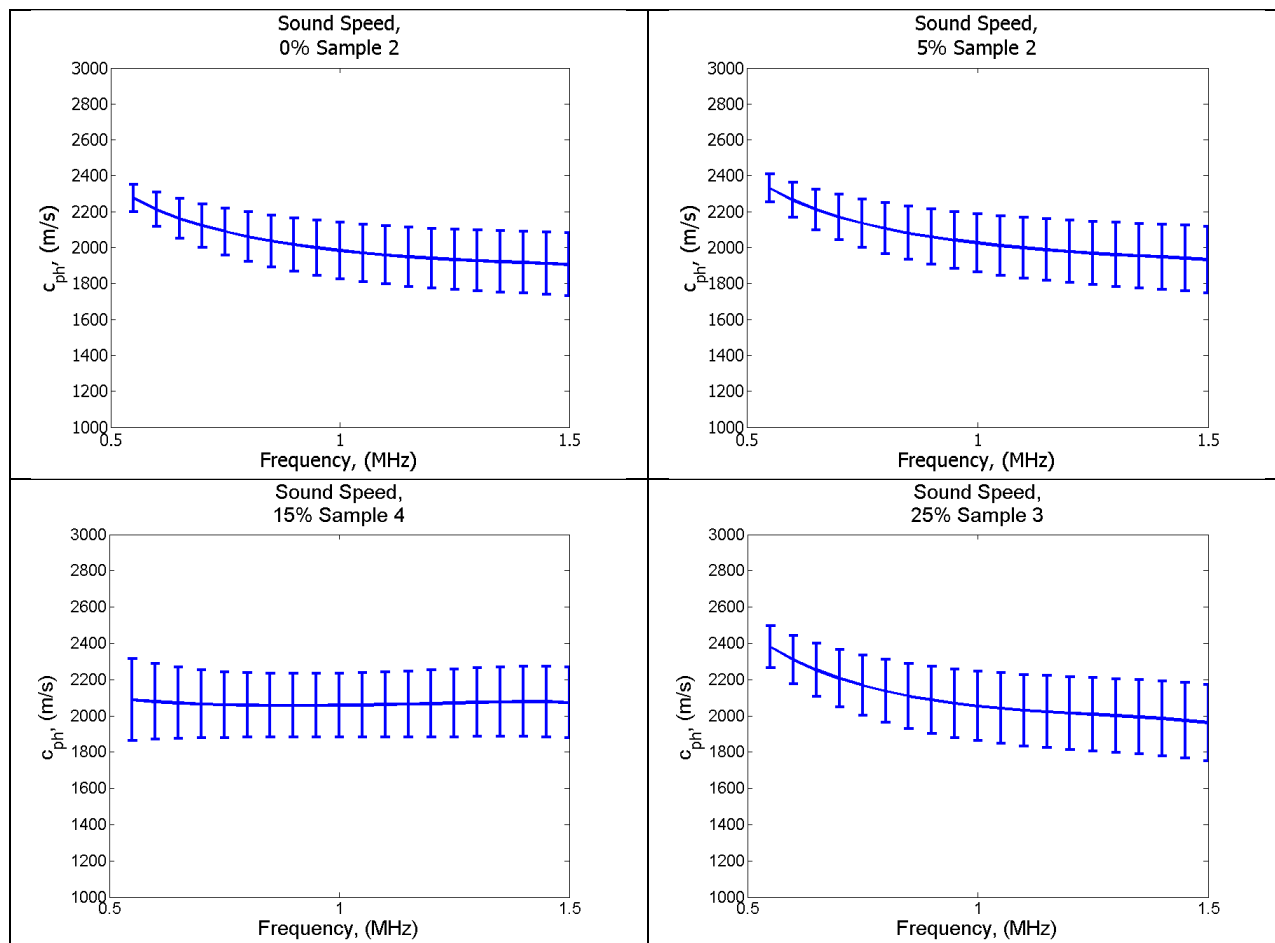
The ultrasonic tests were accomplished using traditional ultrasonic measurement components. A Panametrics square wave Pulse-Receiver supplied the source voltage and signal conditioning for the receive transducer (whether it be in pulse-echo or transmit-receive configurations). The transducers used were two Panametrics V603 Videoscan 1 MHz center frequency longitudinal reciprocal transducers, the signal was acquired using a Tektronix MSO5000 series digital oscilloscope. A representative signal acquired for M1 (pulse-echo with a free surface) is shown in Figure 51. As was the case in all measurements, a post-processing algorithm extracted the first and second arrivals through

peak detection and time windowing. The resulting spectrum for the full, first and second arrivals are shown in the right column of the same figure. The frequency dependent difference in magnitude between the first and second arrival is indicative of the signal attenuation (though this is not corrected for reflection losses at the transducer-material interface) while the difference in phase in combination with the sample thickness can be used to deduce the phase velocity of the sample.

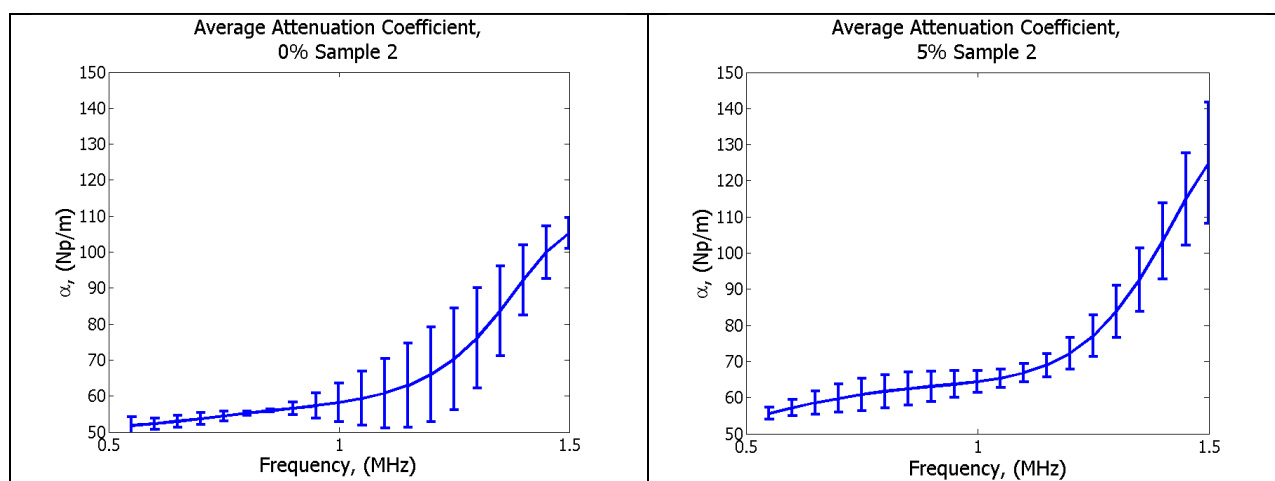


**Figure 51: Representative waveform and associated spectrum from a single measurement on an auxetic inclusion sample.**

As an example, estimates of the frequency dependent attenuation coefficient and phase speed for various samples are shown in Figure 52 and Figure 53. These results suggest that the materials show a slight anomalous dispersion (phase speed decreasing with increased frequency) and increasing attenuation with increasing frequency. The anomalous dispersion may likely results from processing artifacts, especially well away from the center frequency of the transducer, 1MHz. The increase in attenuation coefficient with increasing frequency is typical of most materials an due to a combination of material losses and scattering at the microscale.



**Figure 52: Measured frequency dependent sound speed for representative material samples with varying weight fraction of  $\alpha$ -cristobalite.**



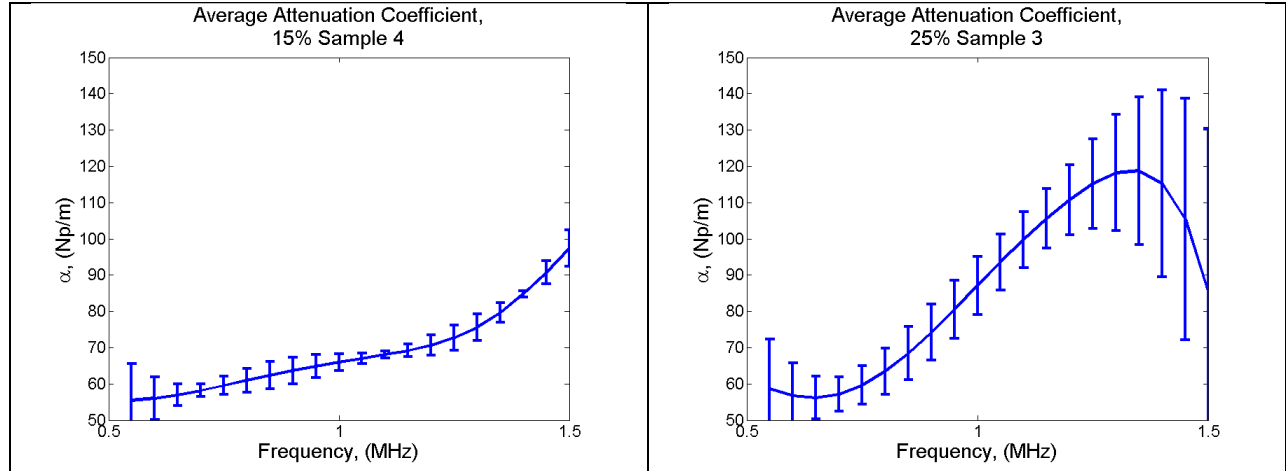


**Figure 53: Attenuation coefficient measured using contact ultrasonic methods of representative samples for varying weight fractions of  $\alpha$ -cristobalite inclusions.**

Using data like that shown in Figure 52 and Figure 53, one can directly the measured effective stiffness and loss of the auxetic composite materials using Eqs. (31) and (32):

$$\eta(f) = \frac{2\alpha}{k'} \frac{1}{1 - (\alpha/k')^2}, \quad (31)$$

$$M'(f) = \lambda + 2\mu = \rho c_{ph}^2 \frac{1 + \sqrt{1 + \eta^2}}{2(1 + \eta^2)} \approx \rho c_{ph}^2 \left[ 1 - \frac{3}{4} \eta^2 \right]. \quad (32)$$

The results of these calculations for all samples are shown in Figure 54 which plots the effective plane wave modulus and loss factor of the material at 1 MHz. Note that the raw and windowed data set shown in Figure 51 is just one of six time-series that was taken for a single sample of a single weight fraction of inclusion. All told, the entire data set used to generate estimates of the stiffness and loss of the auxetic composite, shown in Figure 54, consisted of 36 measurements per sample, or 216 individual measurements to measure the effective frequency-dependent properties of these composite materials.

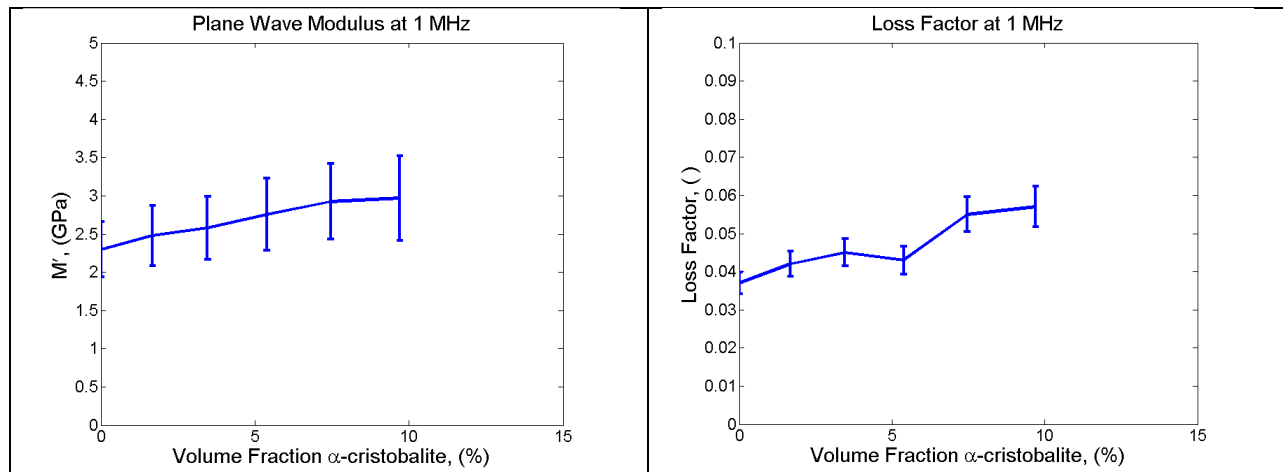


**Figure 54: Plane wave modulus and loss factor as a function of volume fraction  $\alpha$ -cristobalite. Increases in both stiffness (~30%) and loss (~54%) are observed for the auxetic composite 10% by volume composite over the pure matrix material.**

Results from the ultrasonic test seem to more clearly indicate increases in stiffness and loss as a function of increasing volume fraction of auxetic inclusions. Notably, the stiffness is shown to increase nearly 30% while the loss factor increases almost 50% with the use of only 10% by volume of auxetic inclusion. The augmentation of stiffness for this amount of cristobalite is in line with the measurements shown in Figure 42, while the enhancement in effective loss factor is greater than and more monotonic than what was measured using either DMA or vibration techniques. Overall, the ultrasonic measurement displays much less ambiguous trends than the results of the DMA and vibration measurements. However, due to the statistical nature of these results and the clear statistical significance of these trends, we are certain that the ultrasonic measurements indicate increases in lossy behavior of auxetic composites at ultrasonic frequencies.

## 5 Insights and Future Work

The results presented in this report were achieved through modeling (analytical and finite element) of specific structures designed to exhibit NS and experimental characterization of NPR inclusion composites. The work associated with this project has shown that structures that display NS behavior can indeed be designed using buckled elements. Further, a very general finite element energy based approach has been derived, implemented, and benchmarked to determine the nonlinear effective stiffness of a structured element. This approach is unique in the literature and very powerful for the future design of engineered microstructure, regardless of ultimate application. This model provides a powerful tool in the design of microstructured composite materials. This project also integrated this nonlinear homogenization model with more traditional multiscale micromechanical models to produce a multiscale model that predicts macroscopic stiffness and loss parameters as a function of microstructure and mesoscopic parameters like inclusion fraction and orientation distribution. This multiscale model was then employed to do an exhaustive design space exploration of a family of structured inclusion geometries. That exploration provided seed data to generate a Kriging-based surrogate model of the influence of microscale structure on mesoscale anisotropic stiffness. This combination of models provides a very powerful representation of this nonlinear multiscale system that will enable rapid design

of these materials for structure damping treatments [45]. In future work, NS research of this nature should focus on the implementation of the models validated during this project to perform an iterative exploration of the micro- and mesoscale design space to improve the elastic and absorptive properties of viscoelastic composites. Multiscale design model should be wrapped by a nonlinear optimization scheme, such as kernel-based Bayesian network mappings to identify optimal microscale designs that lead to amplified stiffness and loss performance through the use of NS [46].

Auxetic composite material work associated with this research focused on the fabrication of NPR composite materials and their stiffness and loss performance. It provided a broadband characterization of the viscoelastic response of composites containing auxetic inclusions, ranging from static to ultrasonic frequencies. This was achieved through tensile tests, dynamic mechanical analysis, modal damping analysis with damping patches, and ultrasonic measurements. The experimental data showed mixed results on the overall stiffness and loss of the composite. Low frequency measurements (DMA and modal analysis) suggest that no clear correlation between increases in the inherent stiffness and loss properties of the composite with increases in volume fraction of auxetic inclusions. However, ultrasonic measurements unambiguously indicated that both stiffness and loss increase with increases in auxetic fractions. The physical root causes of these observations were not clearly determined. The latter results suggest that auxetic inclusion composites may indeed present a unique means to engineer high loss composite materials without degrading the overall stiffness of the material, but more work must be done to validate this hypothesis. Future work should focus, through both theoretical and experimental methods, on the physical phenomena associated with energy absorption using auxetic inclusions.

## 6 References

- [1] R. S. Lakes and W. J. Drugan, "Dramatically stiffer elastic composite materials due to a negative stiffness phase?," *Journal of the Mechanics and Physics of Solids*, vol. 50, pp. 979-1009, 2002.
- [1a] L. Kashdan, C.C. Seepersad, M.R. Haberman, P.S. Wilson, "Design, fabrication, and evaluation of negative stiffness elements using SLS", *Rapid Prototyping Journal*, vol. 18(3) pp. 194 - 200, 2012.
- [1b] D. Shahan, B. Fulcher, C.C. Seepersad, M.R. Haberman, P.S. Wilson, "Robust Design of Negative Stiffness Elements Fabricated by Selective Laser Sintering," Proceedings of the 22<sup>nd</sup> Annual International Solid Freeform Fabrication Symposium – An Additive Manufacturing Conference, Austin, TX, (8-10 September 2011).
- [1c] G. Milton, *The Theory of Composites*, Cambridge University Press, Cambridge Monographs on Applied and Computational Mathematics (No. 6), 2002.
- [2] M. R. Haberman, "Design of High Loss Viscoelastic Composites through Micromechanical Modeling and Decision-Based Materials Design," Georgia Institute of Technology, 2007.
- [3] Y. C. Fung and P. Tong, *Classical and Computational Solid Mechanics*, vol. 1. Hackensack, New Jersey: World Scientific Publishing Co. Pte. Ltd., 2005, p. 930.
- [4] L. D. Landau, *The Classical Theory of Fields*, 4th ed., vol. 2. Oxford: Butterworth-Heinmann, 1987, p. 402.
- [5] G. Odegard, "Constitutive modeling of piezoelectric polymer composites," *Acta Materialia*, vol. 52, no. 18, pp. 5315-5330, Oct. 2004.
- [6] R. S. Lakes, "Extreme damping in composite materials with a negative stiffness phase," *Physical Review Letters*, vol. 86, no. 13, pp. 2897-2900, 2001.
- [7] M. R. Haberman, Y. B. Berthelot, and M. Cherkaoui, "Micromechanical modeling of particulate composites for damping of acoustic waves," *Journal of Engineering Materials and Technology*, vol. 128, no. 3, pp. 320-330, 2006.
- [8] M. Haberman, Y. Berthelot, and M. Cherkaoui, "Transmission loss of viscoelastic materials containing oriented, ellipsoidal, coated microinclusions," vol. 118, no. 5, pp. 2984-2992, 2005.
- [9] M. Berveiller, O. Fassi-Fehri, and A. Hihi, "The problem of two plastic and heterogeneous inclusions in an anisotropic medium," vol. 25, no. 6, pp. 691-709, 1987.
- [9a] J. Sacks, S.B. Schiller, W.J. Welch, "Designs for Computer Experiments," *Technometrics*, vol. 31(1), pp. 41-47, 1989.
- [9b] P. Backlund, D. Shahan, C.C. Seepersad, "Metamodeling Techniques for Multidimensional Ship Design Problems," *Ship Science & Technology, North America*, vol. 4(7), 2010.



- [9c] G.R. Ely, C.C. Seepersad, "A Comparative Study of Metamodeling Techniques for Predictive Process Control of Welding Applications," ASME International Manufacturing Science and Engineering Conference, West Lafayette, Indiana, Paper Number MESC2009-84189, 2009
- [9d] B.-S. Kim, Y.-B. Lee, D.-H. Choi, "Comparison Study on the Accuracy of Metamodeling Technique for Non-Convex Functions," *Journal of Mechanical Science and Technology*, vol 23, pp. 1175-1181, 2009.
- [10] K. E. Evans, M. A. Nkansah, I. J. Hutchinson, and S. C. Rogers, "Molecular network design," *Nature*, vol. 353, p. 124, 1991.
- [11] R. H. Baughman, J. M. Shacklette, A. A. Zakhidov, and S. Stafstrom, "Negative Poisson's ratios as a common feature of cubic materials," *Nature*, vol. 392, pp. 362-365, 1998.
- [12] A. E. H. Love, *A Treatise on the Mathematical Theory of Elasticity*, Fourth Edi. Cambridge, UK: Cambridge University Press, 1927, p. 643.
- [13] C. Lees, J. F. V. Vincent, and J. E. Hillerton, "Poisson's ratio in skin," *Bio-medical Materials and Engineering*, vol. 1, no. 1, pp. 19-23, 1991.
- [14] J. L. Williams and J. L. Lewis, "Properties and an anisotropic model of cancellous bone from the proximal tibial epiphysis," *Journal of Biomechanical Engineering*, vol. 104, no. 1, pp. 50-56, Mar. 1982.
- [15] D. T. Reilly and a H. Burstein, "The elastic and ultimate properties of compact bone tissue," *Journal of biomechanics*, vol. 8, no. 6, pp. 393-405, Jan. 1975.
- [16] R. Lakes, "Foam structures with a negative Poisson's ratio," *Science*, vol. 235, no. 4792, pp. 1038-1040, 1987.
- [17] E. A. Friis, R. S. Lakes, and J. B. Park, "Negative Poisson's ratio polymeric and metallic materials," *Journal of Materials Science*, vol. 23, no. 12, pp. 4406-4414, 1988.
- [18] J. B. Choi and R. S. Lakes, "Non-linear properties of polymer cellular materials with a negative Poisson's ratio," *Journal of Materials Science*, vol. 27, no. 17, pp. 4678-4684, 1992.
- [19] J. B. Choi and R. S. Lakes, "Nonlinear analysis of the Poisson's ratio of negative Poisson's ratio foams," *Journal of Composite Materials*, vol. 29, no. 1, pp. 113-128, 1995.
- [20] N. Chan and K. E. Evans, "Fabrication methods for auxetic foams," *Journal of Materials Science*, vol. 32, pp. 5945-5953, 1997.
- [21] K. E. Evans, "Tailoring the Negative Poisson's Ratio," *Chemistry and Industry*, vol. 20, p. 654, 1990.
- [22] K. L. Alderson, V. R. Simkins, V. L. Coenen, P. J. Davies, A. Alderson, and K. E. Evans, "How to make auxetic fibre reinforced composites," *Physica Status Solidi (B)*, vol. 242, no. 3, pp. 509-518, 2005.

- [23] K. E. Evans and B. D. Caddock, "Microporous materials with negative Poisson's ratios I: Microstructure and mechanical properties," *Journal of Physics D: Applied Physics*, vol. 22, pp. 1877-1882, 1989.
- [24] K. L. Alderson and K. E. Evans, "The fabrication of microporous polyethylene having a negative Poisson's ratio," *Polymer*, vol. 33, no. 20, pp. 4435-4438, 1992.
- [25] K. L. Alderson, A. Alderson, R. S. Webber, and K. E. Evans, "Evidence for uniaxial drawing in the fibrillated microstructure of auxetic microporous polymers," *Journal of Materials Science Letters*, vol. 17, pp. 1415-1419, 1998.
- [26] A. P. Pickles, K. L. Alderson, and K. E. Evans, "The effects of powder morphology on the processing of auxetic polypropylene (PP of negative poisson's ratio)," *Polymer Engineering & Science*, vol. 36, no. 5, pp. 636-642, Mar. 1996.
- [27] N. Ravirala, a Alderson, K. L. Alderson, and P. J. Davies, "Auxetic polypropylene films," *Polymer Engineering & Science*, vol. 45, no. 4, pp. 517-528, Apr. 2005.
- [28] A. Alderson and K. E. Evans, "Modelling concurrent deformation mechanisms in auxetic microporous polymers," *Journal of Materials Science*, vol. 32, pp. 2797-2809, 1997.
- [29] A. Alderson and K. E. Evans, "Microstructural modelling of auxetic microporous polymers," *Journal of Materials Science*, vol. 30, no. 13, pp. 3319-3332, 1995.
- [30] K. L. Alderson and V. R. Simkins, "Auxetic materials," U.S. Patent 6,878,3202005.
- [31] K. L. Alderson, A. Alderson, G. Smart, V. R. Simkins, and P. J. Davies, "Auxetic polypropylene fibres: Part 1 - Manufacture and characterisation," *Plastics, Rubber and Composites*, vol. 31, no. 8, pp. 344-349, 2002.
- [32] V. R. Simkins, N. Ravirala, P. J. Davies, A. Alderson, and K. L. Alderson, "An experimental study of thermal post-production processing of auxetic polypropylene fibres," *Physica Status Solidi (B)*, vol. 245, no. 3, pp. 598-605, 2008.
- [33] N. Ravirala, a Alderson, K. L. Alderson, and P. J. Davies, "Expanding the range of auxetic polymeric products using a novel melt-spinning route," *Physica Status Solidi (B)*, vol. 242, no. 3, pp. 653-664, Mar. 2005.
- [34] N. Ravirala, a Alderson, and K. L. Alderson, "Interlocking hexagons model for auxetic behaviour," *Journal of Materials Science*, vol. 42, no. 17, pp. 7433-7445, May. 2007.
- [35] D. R. Poulter, *The Design of Gas-Cooled Graphite-Moderated Reactors*. New York, NY: Oxford University Press, 1963, p. 692.
- [36] K. Muto, R. W. Bailey, and K. J. Mitchell, "Special requirements for the design of nuclear power stations to withstand earthquakes," *Proceedings of the Institution of Mechanical Engineering*, vol. 177, pp. 155-203, 1963.

- [37] G. Chirima, N. Ravirala, a Rawal, V. R. Simkins, a Alderson, and K. L. Alderson, "The effect of processing parameters on the fabrication of auxetic extruded polypropylene films," *Physica Status Solidi (B)*, vol. 245, no. 11, pp. 2383-2390, Nov. 2008.
- [38] B. Chekkal, I. Bianchi, M. Remillat, C. D. L. Bécot, F.-X. Jaouien, and F. Scarpa, "Vibro-acoustic properties of auxetic open cell foam: Model and experimental results," *Acta Acoustica with Acustica*, vol. 96, no. 2, pp. 266-274, 2010.
- [39] R. Lakes and K. Elms, "Indentability of conventional and negative Poisson's ratio foams," *Journal of Composite Materials*, vol. 27, no. 12, pp. 1193-1202, 1993.
- [40] K. L. Alderson, R. S. Webber, U. F. Mohammed, E. Murphy, and K. E. Evans, "An experimental study of ultrasonic attenuation in microporous polyethylene," *Applied Acoustics*, vol. 50, no. 1, pp. 23-33, 1997.
- [41] K. L. Alderson, A. F. Fitzgerald, and K. E. Evans, "The strain dependent indentation resilience of auxetic microporous polyethylene," *Journal of Materials Science*, vol. 35, no. 16, pp. 4039-4047, 2000.
- [42] M.L. Lee, Y. Lia, Y.P. Feng, C.W. Carter, "Study of frequency dependence modulus of bulk amorphous alloys around the glass transition by dynamic mechanical analysis," *Intermetallics*, vol. 10, pp. 1061–1064, 2002.
- [43] W.K. Goertzen, M.R. Kessler, "Dynamic mechanical analysis of carbon/epoxy composites for structural pipeline repair," *Composites: Part B*, vol 38, pp. 1–9, 2007.
- [44] M. Treiber, J.-Y. Kim, L.J. Jacobs, J. Qu, "Correction for partial reflection in ultrasonic attenuation measurements using contact transducers," *The Journal of the Acoustical Society of America*, vol. 125(5), pp. 2946-2953, 2009.
- [45] T. Klatt, M.R. Haberman, D.W. Shahan, C.C. Seepersad, "Hierarchical Modeling and Design of Composite Materials with Negative Stiffness Inclusions," Presented at the 49<sup>th</sup> Annual Technical Meeting of the Society of Engineering Science, Atlanta, GA, (10-12 October 2012).
- [46] D. Shahan and C.C. Seepersad, "Bayesian Network Classifiers for Set-Based Collaborative Design," *Journal of Mechanical Design*, vol. 134(7), pp. 071001-14, 2012.